Fatigue of Sintered Materials

Theory and Application

Srečko Glodež

Fatigue of Sintered Materials

Fatigue of Sintered Materials:

Theory and Application

By

Srečko Glodež

Cambridge Scholars Publishing

Fatigue of Sintered Materials: Theory and Application

By Srečko Glodež

This book first published 2021

Cambridge Scholars Publishing

Lady Stephenson Library, Newcastle upon Tyne, NE6 2PA, UK

British Library Cataloguing in Publication Data
A catalogue record for this book is available from the British Library

ISBN (10): 1-5275-6948-9
ISBN (13): 978-1-5275-6948-5

TABLE OF CONTENTS

ACKNOWLEDGMENTS

The author wishes to acknowledge gratefully all of my colleagues from the Faculty of Mechanical Engineering, University of Maribor, for their contribution and helpful comments in the framework of the following research projects:

- Design of cellular structures (ARRS-P2-0063, Head Prof. Z. Ren);
- Development of multifunctional auxetic cellular structures (ARRS-J2-8186, Head Prof. M. Vesenjak);
- Development of the model of the system for intelligent support of the selection of suitable powder material when developing sintered products (ARRS-L2-4283, Head Prof. J. Flašker)

I am also greatly indebted to all of my students, for their inspiration and assistance, and many thanks to Shelagh Margaret Hedges for her English proofreading of this book. Last but not least, thanks to all my family, who has inspired me, supported me, and given me the opportunity to be who I am.

Author

FOREWORD

The technical systems' development process is defined relatively precisely and reasonably well supported with modern computer tools. Numerous commercial computer aids or specially developed computer tools are relying mostly on graphic presentation, simulations, engineering analysis (i.e. the Finite Element Method) and animations of future technical system performance in the virtual environment. In the embodiment phase, the designer has to take decisions, influenced by various parameters, according to the available data. One of the crucial decisions is material selection, conditioned by several criteria, among which the proposed project will focus on function, technical features and shape of the developing product or technical system. Other criteria, like serviceability, technical feasibility and economic justification, are going to be considered accordingly. Despite the potential of the already mentioned computer tools, a designer has to evaluate the information gathered from these aids, seek interdependences and, finally, choose the optimum from the broad list of materials. Powder materials will be outlined here, as they are used frequently in technical praxis. On the other hand, there is a lack of relevant data and knowledge for successful selection between them. Consequentially, the designer has to master all influential parameters, their overlapping or contradictions, and, above all, he or she has to know the materials available on the market. A designer's right/wrong decision influences a product's applicability severely in praxis, its technical feasibility, life time, economic justification and recycling possibilities, along with its environmental impact. Thus, numerous experts from various fields usually need to contribute their expertise to reach the final decision, which is often quite difficult, as opinions may be contradictive. In addition, sustainability has to be considered as well. Sometimes, an appropriate intelligent system may support the selection of a suitable powder material according to the function, technical features and design criteria. Such a system may be able to support the designer in the decision-making process, whilst selecting the most appropriate powder material for the product or technical system.

Due to low price, low waste, tight tolerances and evermore improving mechanical properties, Powder Metallurgy (PM) is becoming an interesting alternative mass production process for the future. Especially, the automotive industry has been using this technology to produce non-vital

parts. Literature research on this field however concludes that sintered parts will enter the industry as vital automotive parts, such as transmission gears and connecting rods. In-depth chemical analysis, differential scanning calorimetry and thermos-gravimetric analysis have given an important understanding of sintering conditions and the diffusion process between powder particles.

This book by S. Glodež is one of the first Slovenian monographs in international space on the above-discussed subject. It is based mainly on the results obtained by the author and his collaborators during their original research, and concerns the problems of fatigue and fracture mechanics of machine parts and structural components.

Maribor, March 2021
Author

CHAPTER 1

INTRODUCTION

Powder Metallurgy (PM) is a general term which represents all techniques to produce solid-metal-based products from powders [1.1]. This involves powder production and its treatment, one or more consolidation steps involving application of appropriate pressure and temperature, and a multitude of additionally (secondary) treatments, which can be similar to those applied to the wrought metallic components. The world-wide popularity of PM-technologies lies in its ability to manufacture complicated products to exact dimensions, at very high rates and economical prices. However, this technology also has some weaknesses, which are mainly related to the high tooling cost and strength characteristics of PM-products. The main advantages and disadvantages of PM-products are summarised in Table 1.1 [1.2, 1.3]:

Table 1.1: The main advantages and disadvantages of PM-products

Advantages	Disadvantages
• The PM-parts can be produced clean and ready for use. • Close dimensional tolerance can be achieved. • The machining operation can be reduced, or almost eliminated. • The material wastage is small and can be neglected. • Metal powders can be mixed in any proportion. • A high production rate can be achieved. • Composition of structure (porosity, density, etc.) can be controlled easily. • Production of self-lubricated parts is possible.	• The high cost of metal powders if compared to the cost of raw material for casting or forging. • The high cost of tooling and equipment (especially when production volumes are small). • PM-parts generally have lower ductility and strength than those produced by forging, casting or machining. • Uniformly high – density products are difficult to produce. • Large parts are difficult to produce by the PM process due to the large pressure required. • Dimensional changes may appear during sintering.

1.1 The basic process of PM-technology

The two basic elements for manufacturing a sintered component are metallic powder and tooling. Having them, the basic process to follow for producing a sintered component consists of three operations, i.e., powder mixing, compacting, and sintering. The basic principle of manufacturing of sintered components is shown schematically in Figure 1.1.

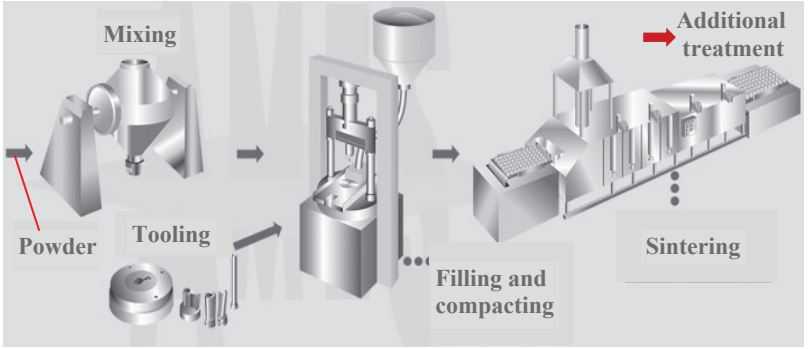

Figure 1.1: Basic principle of manufacturing of sintered components [1.4]

1.1.1 Powder (Raw material)

The raw material of a sintered component is always a metallic powder. Metal powder can be of pure metal (iron, copper, aluminium, etc.), or alloyed powder (bronze, brass, steel, etc.). The material characteristics to be achieved determine the powder's chemical composition.

The production of powders for PM-products can be divided into *mechanical* and *chemical* methods. Here, the final properties and the price of the powder are strongly dependent on the raw-material cost, the production method (large scale vs. small scale), particle shape, size and distribution, impurities, and oxygen sensitivity [1.1, 1.5].

The mechanical methods to produce metal powder are generally divided into (i) Disintegration without phase change and (ii) Disintegration with phase change. The disintegration without phase change is one of the easiest ways to produce powder from solids, where machining techniques such as milling or turning are usually used for that purpose. However, this method is quite expensive, its productivity is relatively low and the danger of

contamination is high. For those reasons, it is applied only for special purposes. On the other hand, the disintegration with phase change is the way to produce powder from liquids (water, oil, gases), usually by using the atomisation process. This method is the most modern and productive way to obtain metal powders for PM-production. Namely, most worldwide shipments of iron and steel powders are produced by the water-atomisation technique.

The chemical methods to produce metal powder are generally divided into the following procedures [1.1]:

- *Reduction with solids*. The classical method of metal powder production using ore reduction. The most pronounced feature of this powder is the internal porosity of the particles (sponge iron powder).
- *Reduction with gases*. For the reduction of ores where the final carbon content should be extremely low. Here, reduction by hydrogen is the standard process for the production of tungsten and molybdenum from WO_3 and MoO_3.
- *Electrochemical reduction*. The production by electrolysis from aqueous solutions is applicable for Copper, Iron, Nickel, and Cobalt, and, due to hydrogen overvoltage, also for Chrome and Manganese. The particle size, size distribution, and shape are determined by the electrical current density, the temperature, concentration, acidity, and the bath movement.
- *Decomposition of gases*. The carbonyl method is used mainly to produce fine Iron and Nickel powders. The powders have very low contents of metallic impurities. Although the process is energy consuming, it is the main production method for Nickel and Iron powder.
- *Reaction with solids (Carbides)*. Carbides, as the major raw material for cemented carbides, are usually produced by reaction with carbon (soot). In this way, WC is produced by intense mixing of tungsten powder with the desired particle size and carbon, and subsequent reactive annealling in hydrogen in graphite tube furnaces. TiC, NbC and TaC are produced by direct reduction and carburisation from their oxides (TiO_2, Ta_2O_5, Nb_2O_3) in a vacuum.

The different applications for metal powders require the appropriate powder characterisation regarding their physical (size, shape and distribution of powder particles), chemical (chemical composition, degree of purity), and technological (flow rate, apparent density, compressibility, green strength) properties.

1.1.2 Mixing and blending

The majority of powders are mixed with other powders or different alloying elements (such as Graphite, Nickel, Copper, etc.), binders and lubricants (the addition of binders and lubricants is necessary to provide the desired compaction properties), to achieve the desired characteristics in the finished product. The result is a powder mixture with a homogeneous additive distribution, which is ensured through the strict dosing and control processes, and it is of critical importance in order to achieve the appropriate physical, chemical and technological characteristics of the material. The time for mixing and blending may vary from a few minutes to several days (depending upon results desired), and can be done in either wet or dry conditions.

1.1.3 Tooling

The powder mixture is compacted inside the tooling, which has the negative shape of the final part. The tool is an element of a very high precision and high durability. Tooling assembly and maintenance is usually carried out by means of SMED (Single Minute Exchange of Dies) techniques.

1.1.4 Filling and compacting

The powder mixture is filled into the tool cavity of a mixer by gravity, and a uniaxial pressure within 40 to 1650 MPa (see Table 1.2) is applied onto it, depending on the final density to be achieved. Here, the mechanical, hydraulic or pneumatic presses are used for that purpose. The compacted part is ejected from the tooling, and the result is a "green part", which has a certain mechanical strength and can be handled. The compacting process is usually assured statistically by SPC (Statistical Process Control) controls of the unique characteristics of a part.

Table 1.2: Typical compacting pressures for various applications [1.2]

Application	Compaction pressure [MPa]
Porous metals and filters	40 – 70
Refractory metals and carbides	70 – 200
Porous bearings	140 – 350
Steel parts (medium density)	270 – 690
Cu- and Al-parts (high density)	250 – 275
Steel parts (high density)	690 – 1650

Figure 1.2 shows the typical compaction sequence for a single-level part during the filling and compacting process. Because powder does not flow like liquid, it is simply compressed until an equal force is reached acting in the opposite direction. This opposing force consists of the resistance by the bottom punch, and friction between the particles and die surface.

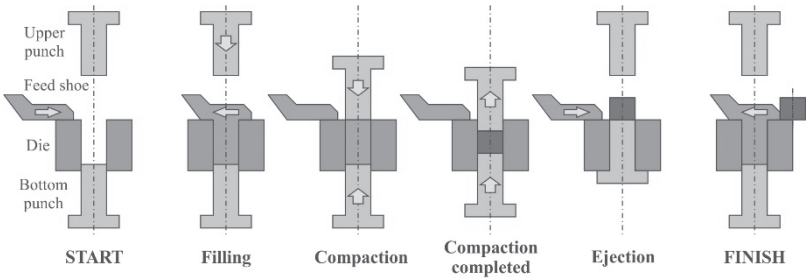

Figure 1.2: Typical compaction sequence for a single-level part [1.2]

When the pressure is applied by only one punch (as already presented in Figure 1.2), the maximum density occurs right below the punch surface and decreases away from the punch. The heterogeneous density actually appears due to friction between the powder particles and friction between the powder and the die walls. This can be avoided if the compacting pressure is applied to the powder evenly from all directions (isostatic pressure [1.6]), which is achieved by placing the powder in a closed flexible mould and introducing the mould in a fluid (liquid or gas) that is pressurised afterwards. In the case of Cold Isostatic Pressing (CIP), the powder is poured into a flexible mould at room temperature and compacting pressure up to 1500 MPa (the pressures used in practice are commonly around 200–600 MPa [1.7]). CIP has become an essential process step for the production of certain PM materials or products: Mo and W (e.g., in arc furnace melting electrodes), hard metal parts (e.g., rollers and dies), high-speed steel products, long thin-walled cylinders, etc. On the other hand, Hot Isostatic Pressing (HIP) is used to densify powders at high pressure and temperatures from 900 °C to 1,250 °C, for example for steels and super-alloys [1.8]. The HIP- process provides improved stability and mechanical properties of solid parts due to the fine and homogeneous isotropic microstructure. Because of its production costs, HIP finds many applications in the production of special PM materials, such as high-speed steels, super-alloys, and titanium alloys. Owing to the properties that can be achieved, many applications can also be found in the automotive and aerospace industries (structure and engine parts), aggressive environments, etc.

1.1.5 Sintering

The green compact produced by compressing (see previous Section), is not very strong and can't be used as a final product. For that reason, sintering is a reasonable production step, which follows after the finishing of compacting stage. According to the ISO definition [1.9], "*Sintering is the thermal treatment of a powder or compact at a temperature below the melting point of the main constituent, for the purpose of increasing its strength by bonding together of the particles*". Following this definition, sintering is a thermal cycle, consisting of heating the compacted part during a given time at lower temperature than the base metal melting point (the sintering temperature is generally about 70 to 90 percent of the melting temperature of the metal powder). The high temperature leads to welding of particles between them, and to the alloying elements by means of a solid-state diffusion mechanism. This process provides strength to the green compact and converts it into a final product.

Sintering can be performed in different variants [1.10–1.12]: Solid phase, activated, liquid phase, reactive, etc. The most straightforward variant of sintering is solid-phase sintering of single component systems, which can be divided into the three main stages (see Figure 1.3). At the beginning, the particles of the pressed (green) part meet at highly deformed pressing contacts (Figure 1.3*a*). In the early stage of sintering, metallic interparticle contacts are formed and grow, but the interparticle porosity is still interconnected and open (Figure 1.3*b*). In the next stage, the pores become closed and isolated from one another (Figure 1.3*c*). Finally, any remaining porosity decreases slowly and grain coarsening occurs [1.13].

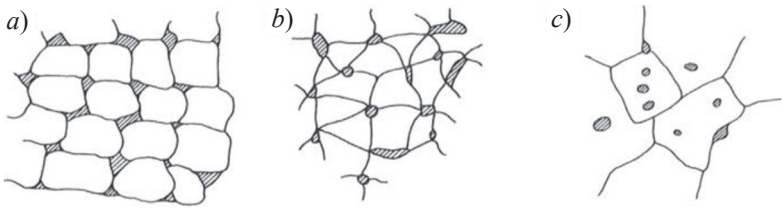

Figure 1.3: Main phases of sintering [1.1]
a) Green state, *b*) Open porosity, *c*) Closed porosity

Sintering is generally carried out in a controlled atmosphere (i.e. a vacuum furnace) to prevent or reduce oxidation of the large number of metal

particles. Liquid Phase Sintering (LPS) is also used in some cases, and is carried out at a temperature at which a liquid phase exists.

1.1.6 Additional treatment

Additional treatments (applications) represent complementary operations on a sintered component which allow improvement of one or more characteristics not directly achievable from the basic PM-process. For instance, these additional operations may be used to reproduce complex shapes, achieve closer tolerances, improve mechanical properties, or protect against corrosion. Although some additional costs appear using these operations, the final products are often still economical compared to those from competing technologies. A number of finishing operations (sizing, coining, porosity impregnation, plating/coating, machining, deburring and cleaning, heat treatment, surface densification, joining, etc.) are known to improve specific properties of sintered products [1.1, 1.4, 1.14].

Sizing is a post sintering operation to correct size, distortion and other geometrical defects of a sintered part, or to improve (reduce) surface roughness. The process consists of compacting the sintered part into a die of smaller dimensions, which has the symmetrically opposite shape of the part. The tolerances and properties achievable after sizing depend on the material (the tolerance class up to IT 5 is reachable [1.15]).

Coining is a repressing operation which produces the same results as the sizing. However, coining additionally improves the density, hardness and strength of the sintered part.

Porosity impregnation consists of filling open porosity (pores) with various substances. If the substance used is oil, it can act as a lubricant of the sintered part (i.e. self-lubricated bearing bushes). Plastic or resin impregnation provides sealing (this operation is quite common as preparation of the sintered parts before plating/coating). Sealing the open porosity also provides some increase in mechanical properties, improves pressure-tightness, and has a positive effect on machinability. Furthermore, copper impregnation (infiltration) consists of sintering the part together with a pressed copper plate on it. Copper is molten during sintering, and becomes infiltrated inside the pores by means of capillarity. This procedure is often used to increase the mechanical strength and toughness of low alloyed sintered steels.

Plating /coating is a material deposition on the component surface, which modifies the surface properties without changing the base metal chemical composition. The final result is improved wear resistance and corrosion protection [1.16]. *Plating* is performed on sintered parts in the same way as in wrought or cast materials, where Cu, Ni, Cd, Zn, Cr and other metals are deposited galvanically on the surface. However, in PM parts, the surface pores must be sealed before plating using an appropriate impregnation process. *Coating* is applied to a large percentage of hard metal inserts. Here, the Chemical Vapour Deposition (CVD) and the Physical Vapour Deposition (PVD) processes are usually used to deposit ceramic layers of TiC, TiN, Al2O3, TiAlN, etc. As presented in [1.17, 1.18], the coating performance can be improved by the combination of several thin coating layers (multilayer coatings).

Machining. Sintered components can sometimes be machined when a shape or tolerance not achievable by compacting is required. Sintered parts support all conventional machining operations (turning, milling, drilling, threading, grinding, lapping, reaming, polishing, etc. [1.19). However, the machining parameters for sintered parts are different from those of cast or wrought components, and are dependent on typical PM-properties (density, chemical composition, additives, etc. [1.20]). In general, machining becomes more difficult with higher porosity levels and with heterogeneous microstructures. The machinability of PM parts can be improved by using some additives prior to compaction (Pb, Cu, S, MgS, graphite, etc.). Furthermore, infiltration with low-melting point metals or polymer (porosity impregnation) is a common practice to improve machinability.

Deburring/cleaning. *Deburring* is applied to remove burrs, sharp edges, or surface irregularities resulting from compaction or machining operations. Burrs are removed either in bulk (tumbling, shot blasting, etc.), or on a unit basis (brushing, polishing, electrolytic deburring, etc.). *Cleaning* operations are used to reduce or eliminate the amount of pollutants, solid or liquid, that a part may contain. There are many techniques (ultrasonic cleaning, electrolytic cleaning, etc.) depending on the material, type of pollutant, and required specifications which may be used for that purpose.

Heat treatment involves heating and cooling of the sintered part to modify (improved) it's material properties (tensile strength, fatigue strength, impact toughness, hardness, wear resistance, etc.). The main heat treatments of sintered parts are:

- *Induction hardening* allows performing a heat treatment only in certain areas of the part surface. The depth and hardness of the hardened layer can be controlled by appropriate heating and quenching parameters.
- *Case hardening* is a process for increasing surface wear resistance and fatigue strength. The chemical composition of the surface is modified by carburising (local diffusion of carbon) or nitriding (local diffusion of nitrogen), and the sintered part is subsequently quenched.

Surface densification is a mechanical process to increase the density of near-surface layers of the sintered part. The process is based on the controlled localised plastic deformations which create compressive residual stresses in the surface layers, and, consequently, improve the fatigue properties of the sintered part significantly [1.21]. The main surface densification procedures of sintered parts are:

- *Shot peening* is a cold working process in which small spherical particles from metal or ceramic are impacting the surface with enough energy to cause plastic deformation, and, consequently, induce compressive residual stresses in the surface layer of the treated component. Shot peening has an additional effect, because plastic deformation closes smaller pores and reduces the size of larger pores on the surface [1.22].
- *Surface cold rolling* is a cold working process in which the worked piece (sintered part) and rolling toll are meshing (rolling between each other) to remove a controlled amount of excess material on the surface of the sintered part. This method is usually used for local densification of sintered bearing races and sintered gears, to improve wear and pitting resistance [1.23, 1.24].

Joining. Sintered parts are susceptible to being joined to other sintered parts or to components made from other technologies [1.4]. Typical joining techniques are welding, brazing, sinter-bonding, fitting, sticking, riveting, over-moulding, etc.

1.2 PM-products

The capital goods industry (the automotive, electrical appliances, hand-tool industries and other high-volume industrial segments) is a major consumer of sintered parts. As a reference, each car uses between 10 and 15 kg of sintered parts (about 600 sintered components with an average weight of 20

grams). A wide range of materials, shapes, finishes, treatments and coatings can be used to produce PM-parts with a high accuracy and performance. Their mechanical properties are, in some cases, comparable to those of wrought or cast products [1.4].

Sintering is used to make a great number of different structural products: High-strength and high-precision components, tribological parts (oil-impregnated bearings), electrical parts (contact elements for Low- and High-Voltage switchers) and magnetic parts (soft-magnetic components). Additional opportunities of PM products are hardphase-based materials, refractory metals, PM-superalloys, etc. [1.25].

Structural parts made of low-alloyed steel represent a large portion of PM-products. Many of these advanced structural parts need the appropriate secondary operation (see Section 1.1.6) to improve their strength characteristics [1.26]. Some typical examples of PM-structural parts are shown in Figure 1.4.

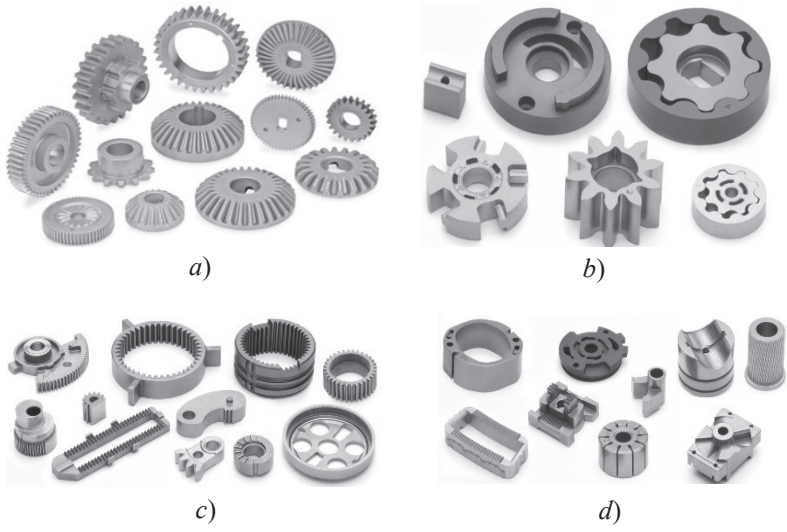

Figure 1.4: Examples of PM-structural parts (Ames [1.4], Capstan [1.27],)
a) Different types of gears, *b*) Components of oil-pumps *c*) Gears and toothed parts of sundry shapes, *d*) Components for steering applications

If corrosion resistance is required, PM-structural parts are usually produced from austenitic, martensitic, or duplex stainless steels [1.1]. Here, the Metal Injection Moulding (MIM) has extended the application of corrosion-resistant steels to small and complex parts for automotive and medical applications. The main difference of these products, apart from their complex shape, is the almost full density and closed porosity, which is reached by the MIM-process using extremely fine powders.

In some special applications, PM-technology can also be used to produce tool steel parts with complex shape in high quantities (cold work tools for pressing dies and punches, hot work tools for injection moulding inserts, high-speed steels for the highest operating temperatures, etc. [1.28]). Here, the conventional pressing is combined with the supersolidus liquid phase sintering in a vacuum [129].

PM-technology is also suitable for producing different tribological parts, where the Copper (Cu) is often used as the main alloying element in the raw material (powder). The major Cu alloys produced by PM are bronze (Cu-Sn), brass (Cu-Zn), and Ni–Ag alloys. A key feature of using PM for the production of tribological parts (i.e. self-lubricated bearings, Figure 1.5*a*) is the ability of this technique to produce porous metallic parts in which the level of porosity is controlled, as well as the shape and size distribution of the pores. A self-lubricating sintered bearing is a metallic component with high porosity (usually between 20-25%), impregnated in a lubricant oil. The oil contained in the porosity provides a constant lubrication between bearing and shaft, so the system does not need any additional external lubricant. A self-lubricating sintered sliding bearing can operate under hydrodynamic lubrication conditions, resulting in a very low friction coefficient. Another example of the use of PM-structural parts with controlled porosity are filters (Figure 1.5*b*). Typical application areas are the chemical industry (water purification, nuclear installations, heat exchangers, general drying, etc.), the food industry (gasification of liquids and spirits, liquefaction, packaging manufacture, etc.), household appliances (boilers, water heaters, gas burners, etc.).

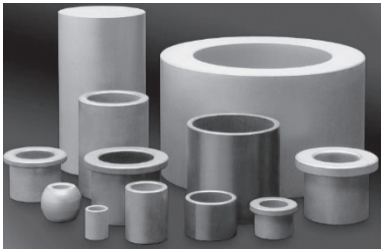

a)

b)

Figure 1.5: Sintered parts with controlled porosity (Ames [1.4])
a) Self-lubricated bearings, *b*) Filters

The use of PM-products in the electro industry is related mostly to the contact parts for Low- and High-Voltage switchers. The base material for Low-Voltage switching is silver, due to its high electrical conductivity and its chemical stability against the surrounding atmosphere (air) [1.30]. Silver-based composite materials produced by PM-technology are used to withstand the mechanical loads during switching to reach sufficient wear resistance and suppress the welding tendency [1.1]. The High-Voltage switches are used in the medium voltage range up to 40 kV. These kinds of switches are usually made of Cu-Cr alloys.

Sintered soft magnetic parts are typical PM-products to guide or amplify a magnetic field. Their function in an electromagnetic circuit is to transform an electrical signal into motion or to transform motion into an electrical signal, based on their ability to be magnetised and demagnetised easily and quickly when a magnetic field is applied or removed. Some typical examples are shown in Figure 1.6.

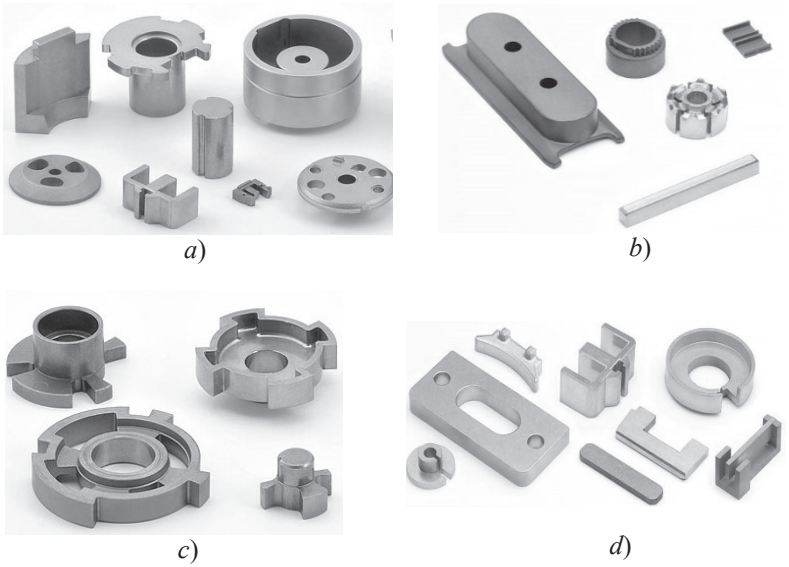

a) *b*)

c) *d*)

Figure 1.6: Typical examples of soft-magnetic sintered parts (Ames [1.4])
a) Actuators (winding cores, armatures, stators, rotors, housings, etc.), *b*) Electrical machine components (pole pieces, winding cores, contactors, switches, etc.), *c*) Pulse sensors (ABS brakes, vehicle engines, camshafts, crankshafts, etc.) *d*) High-sensitivity detectors (when a fast response is required)

References

[1.1] Danninger H., Calderon R. de Oro, Gierl-Mayer C., *Powder Metallurgy and Sintered Materials*, Wiley-VCH Verlag GmbH & Co. KGaA, Weinheim, 2017.

[1.2] Black J.T., Kohser R.A., *DeGarmo's Materials and Processes in Manufacturing*, 13th Edition, Wiley, 2019.

[1.3] Upadhyaya A., Upadhyaya G. S., *Powder Metallurgy, Science, Technology, and Materials*, CRC Press, 2011.

[1.4] AMES, *Sintered Metallic Components* https://www.ames-sintering.com

[1.5] Schatt W., Wieters K.P., Kieback B., *Powder Metallurgy Processing and Materials*, European Powder Metallurgy Association, Shrewsbury, 1997.

[1.6] Eklund A., Ahlfons M., Heat treatment of PM parts by Hot Isostatic Pressing, *Metal Powder Report*, 73, 2018, 163–169.

[1.7] Price P.E., *Powder Metal Technologies and Applications, Cold Isostatic Pressing*, ASM Handbook, Metals Park OH, 1998.
[1.8] HÖGANÄS, *Hot Isostatic Pressing (HIP)* https://www.hoganas.com/en/powder-technologies/hip/
[1.9] ISO 3252:2019, *Powder Metallurgy - Vocabulary*, International Standard Organisation, Geneva, Switzerland, 2019.
[1.10] German R.M., *Sintering Theory and Practice,* John Wiley & Sons, New York-Chichester-Brisbane–Toronto–Singapore, 1996.
[1.11] German R.M., History of sintering–empirical phase, *Powder Metallurgy*, 56, 2013, 117–123.
[1.12] Kang S.J.L., *Sintering–Densification, Grain Growth and Microstructure,* Elsevier-Butterworth-Heineman, Oxford, 2005.
[1.13] Dlapka M., Strobl S., Danninger H., Gierl C., Austenite grain size in sinter hardened powder metallurgy steels, *Practical Metallography*, 47, 2010, 686–699.
[1.14] Shabudeen S., *Engineering Chemistry II,* KCT, Coimbatore, 2010.
[1.15] Danninger H., Gierl-Mayer C., Advanced powder metallurgy steel alloys, in *Advances in Powder Metallurgy* (eds Chang I., Zhao Y.), Woodward Publishing, Cambridge, 2013.
[1.16] MPIF 35, *Materials Standards for PM Structural Parts*, Metal Powder Industries Federation, Princeton, 2016.
[1.17] Garcia J., Pitonak R., Weissenbacher R., Köpf A., SolderaF., Suarez S., Miguel F., Pinto H., Kostka A., Mücklich F., Design and Characterization of Novel Wear Resistant Multilayer CVD Coatings with Improved Adhesion Between Al2O3 and Ti(C,N), *Advanced Engineering Materials*, 12, 2010, 929–934.
[1.18] Haubner R., The history of hard CVD coatings for tool applications at the University of Technology Vienna, *International Journal of Refractory Metals and Hard Materials*, 41, 2013, 22–34.
[1.19] HÖGANÄS, *Handbook for machining guidelines,* Höganäs, Sweden, 2004
[1.20] Šalak A., Selecka M. Danninger H., *Machinability of Powder Metallurgy Steels*, Cambridge International Science Publishing, Cambridge, 2006.
[1.21] Beiss P., Finishing processes in powder metallurgy, *Powder Metallurgy*, 32, 1989, 277–284.
[1.22] Rivolta B., Gerosa R., Silva G., Tavasci A., Engstrom U., Wear performances of surface hardened PM steel from pre-alloyed powder, *Wear*, 289, 2012, 160–167.
[1.23] Dizdar S., High-performance sintered-steel gears for transmissions and machinery: A critical review, *Gear Technology*, 2012, 60–65.

[1.24] Jones K., Buckley-Golder K., Sarafinchan D., Developing PM gear tooth and bearing surfaces for high stress applications, *International Journal of Powder Metallurgy*, 34, 1998, 26–33.
[1.25] Tsutsui T., Recent Technology of Powder Metallurgy and Application, Hitachi Powdered Metals Co. Ltd., 2020. https://www.hitachi-chem.co.jp/english/report/054/54_sou2.pdf
[1.26] Forden L., Bengtsson S., Magnus B.M., Comparison of high performance PM gears manufactured by conventional and warm compaction and surface densification, *Powder Metallurgy*, 48, 2005, 10–12.
[1.27] CAPSTAN Atlantic, PM Products. https://capstanatlantic.com/all-services/
[1.28] Roberts G., Krauss G., Kennedy R., *Tool Steels*, Materials Park, OH, 1998.
[1.29] German R.M., *Sintering Theory and Practice*, John Wiley & Sons, New York-Chichester-Brisbane–Toronto–Singapore, 1996.
[1.30] Schröder K.H., *Werkstoffe fur elektrische Kontakte und ihre Anwendungen*, Expert Verlag, Ehningen, 1992 (in German).

CHAPTER 2

FATIGUE – THEORETICAL BACKGROUND

Fatigue of engineering components and structures is a localised damage process produced by cyclic loading. In general, it has been observed that the fatigue process involves the following stages [2.1–2.8]: (1) Crack nucleation; (2) Short crack growth; (3) Long crack growth; and (4) Final fracture. In engineering applications, the first two stages (crack nucleation and short crack growth) are usually termed as "*crack initiation period* N_i", while the last two stages (long crack growth and final fracture) are characterised as "*crack propagation period* N_p*"*. The complete fatigue life of an analysed engineering component can then be determined from the number of stress cycles N_i required for fatigue crack initiation, and the number of stress cycles N_p required for a crack to propagate from the initial to the critical crack length, when the final failure can be expected to occur:

$$N = N_{\mathrm{i}} + N_{\mathrm{p}} \tag{2.1}$$

An exact definition of the transition period from the initiation of an "engineering" crack to its propagation is usually not possible. However, for engineering components made of steels the size of initial crack a_{i} is of the order of a few crystal grains of the material. This crack size usually ranges from about 0.1 to 1.0 mm. According to Dowling [2.4], the crack initiation size can also be estimated by the following equations:

$$a_i \approx \frac{1}{\pi}\left(\frac{\Delta K_{th}}{\Delta S_e}\right)^2 \qquad \text{smooth specimen} \tag{2.2}$$

$$a_i \approx (0.1 \ldots 0.2) \cdot \rho \qquad \text{notched specimen} \tag{2.3}$$

where ΔS_e is the stress range at the fatigue limit, ΔK_{th} is the threshold intensity factor range, and ρ is the notch-tip radius.

In general, four fatigue design criteria can be used for dimensioning structural elements subjected to cyclic loading [2.2]:

- Infinite-Life Design,
- Safe-Life Design,
- Fail-Safe Design,
- Damage-Tolerant Design.

Infinite-Life Design

Infinite-Life Design is the oldest fatigue design criterion, which is based on the *S–N* curve, with the assumption that the engineering component is going to reach "infinite" life (usually several millions of cycles). According to this criterion, the stresses are in the elastic area, and should not exceed the fatigue limit of the material.

This criterion is combined exclusively with the Stress-life approach, and is suitable for dimensioning dynamically loaded machine parts or structures which are, in the framework of their fatigue life, actually exposed to millions of cycles (engine valve springs, axes and bearings of railway wagons, shafts and gears of high stages in change-speed gear drives, etc.). However, most engineering components undergo significant variable amplitude loading, and the pertinent fatigue limit is difficult to obtain. In addition, this criterion may not be economical in many design situations where the expected fatigue life is shorter (shafts and gears of low stages in change-speed gear drives, certain parts in the aircraft industry, etc.).

Safe-Life Design

Safe-Life Design is a fatigue design criterion where the engineering component is designed for a finite life, which is often known in advance. This criterion should include a margin for the scatter of fatigue results and for other unknown factors (surface roughness, notch effect, residual stresses, temperature, corrosion, etc.). The dimensioning process may be based on the Stress-life approach if stresses are in the elastic area, or on the Strain-life approach if plastic deformation occurs in the critical cross-section of the treated component.

The Safe-Life Design criterion is suitable for dimensioning dynamically loaded machine parts or structures with an expected specific finite life (reverse gears in car drives, pressure vessels design, jet engine design, etc.).

Fail-Safe Design

Fail-Safe Design is a fatigue design criterion which assumes that some initial cracks may appear in individual parts of engineering structures, but

they are not critical and do not lead to a catastrophic failure of the structure. This fatigue design criterion was developed in the aircraft industry. Namely, aircraft engineers could not tolerate the added weight required by large safety factors, or the danger to life created by small safety factors, or the high cost of the safe-life design. In that respect, the fail-safe design is based on the requirement that the system does not fail if one part fails. This principle recognises that fatigue cracks may occur, and structures are arranged so that cracks will not lead to failure of the structure before they are detected and repaired. In that respect, inspection intervals should be defined exactly when using the fail-safe design criterion. Although this approach was originally applied mainly to aircraft structures (fuselages, wings), it is now used in many other applications.

Damage-Tolerant Design

The *Damage-Tolerant Design* criterion is actually a refinement of the Fail-Safe Design criterion. It is based on the assumption that initial defects exist in engineering structures, which were caused either by mechanical and thermal treatment of components during the manufacturing process, or by fatigue. A fracture mechanics analysis can then be performed, in order to determine whether such defects will grow large enough to produce failures before they are detected by periodic inspection.

In recent decades, several nondestructive inspection methods have been developed to detect possible defects (cracks) in a treated engineering component. If a crack is detected, the residual strength of the treated component should be obtained using the fracture mechanics theory. As a crack growth under cyclic loading, the residual strength decreases up to the critical crack length, when final failure (fracture) occurs. If there is no crack, the residual strength is equal to the ultimate tensile strength or yield stress of the material. Apart from those described above, some other influencing parameters, such as environmental conditions, load history, statistical evaluation, etc., should also be incorporated into this methodology.

The damage-tolerant design criterion is often used when evaluating the residual strength of complex and expensive engineering components, which should be retired from service because they have reached their designed safe-life service life, based upon analytical and experimental results. However, it has often been established that such components could have significant additional service life.

In a combination of the four fatigue design criteria as described above, three main fatigue design approaches can be used when dimensioning the cyclic loaded machine parts or structures [2.2]:

- Stress-life approach ($S - N$),
- Strain-life approach ($\varepsilon - N$),
- Fatigue crack growth approach ($\mathrm{d}a/\mathrm{d}N - \Delta K$).

2.1 Stress-life approach

The *Stress–life approach* is the oldest method for dimensioning dynamically loaded structural components. This approach is based on the *S–N* curve that is commonly plotted in terms of stress amplitude σ_a versus number of loading cycles to failure N, usually in log–log scales. The most basic *S–N* curve is considered to be the one for zero mean stress $\sigma_m = 0$, which corresponds to the stress ratio $R = \sigma_{min}/\sigma_{max} = -1$ (see Figure 2.1).

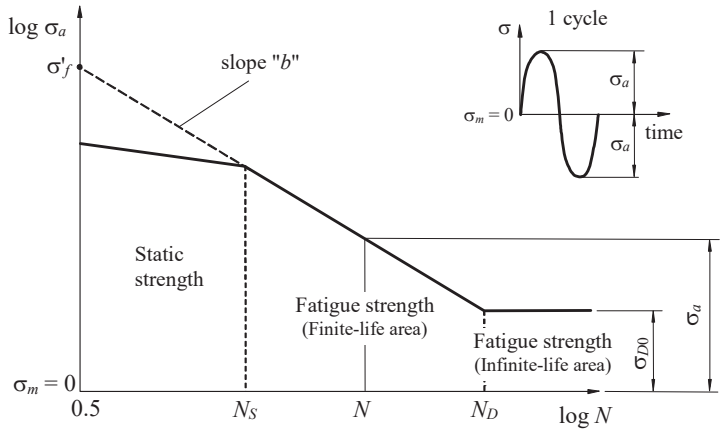

Figure 2.1: *S–N* curve in a log–log scale

For most engineering materials, a distinct dynamic stress level exists below which fatigue failure does not occur under ordinary loading conditions. In this area (i.e. the *Infinite-life area*) the *S–N* curve becomes flat and corresponds to the *fatigue limit* σ_{D0}. The belonging number of loading cycles N_D (knee of the *S–N* curve) is usually between 10^6 and 10^7 for most engineering materials. In the *Finite-life area*, the term *fatigue strength* (or dynamic strength) is used to specify a stress amplitude σ_a from an *S–N* curve

at a particular number of cycles to failure life N, which can be expressed mathematically as follows:

$$\sigma_a = \sigma_f{}'(2 \cdot N)^b \tag{2.4}$$

where σ_f' is the fatigue strength coefficient and b is the fatigue strength exponent (see Figure 2.1). Material parameters σ_f' and b can be determined experimentally, usually by means of the rotating bending test using the appropriate standardised procedures [2.9, 2.10].

A simple S–N curve can be obtained using 10 to 15 specimens loaded with different stress amplitudes σ_a up to the failure of the specimen. First the specimen is usually loaded with $\sigma_a \approx 0.7 \cdot R_m$ (R_m is the ultimate tensile strength) which leads to the relatively short fatigue life. The loading of subsequent specimens is then decreased up to the fatigue limit σ_{D0} (i.e. a limited number of loading cycles N_D) when 2 or 3 specimens do not fail any more. The S–N curve obtained with the procedure described above represents the 50 % probability of failure (P = 0.50, see Figure 2.2). It is clear that some reasonable safety factor should be considered when dimensioning the structural components using this simplified procedure.

Scatter in the fatigue testing is an important consideration when using test data (σ_f', b, σ_{D0}). A variety of factors contribute to the scatter, such as inherent material variability (i.e. variations in chemical composition, impurity levels, etc.), variations in heat treatment and manufacturing (i.e. surface finish, hardness distribution, residual stresses, etc.), variations in specimen geometry (i.e. notch radii, diameter, etc.), and differences in the testing conditions (i.e. environment and test machine alignment variations). In that respect, statistical analysis can be used to describe and analyse the fatigue properties more accurately, as well as to estimate the probability P associated with the fatigue life of the analysed component under given loading conditions. Such analysis allows us to evaluate component reliability quantitatively, and to predict service performance for a given margin of safety [1.2, 1.4].

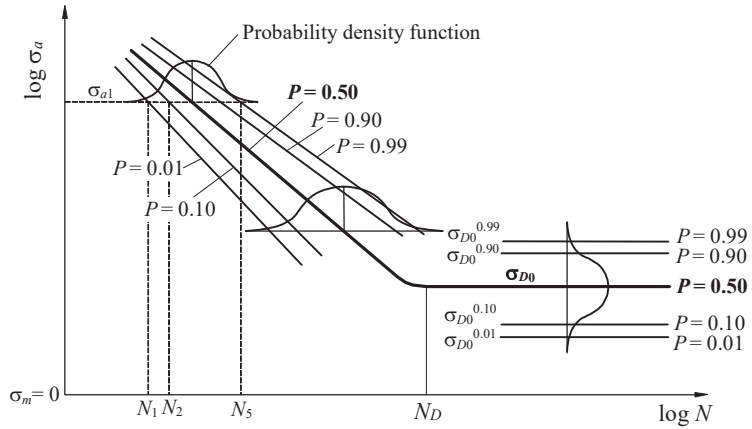

Figure 2.2: Statistical evaluation of dynamic strength in *P*-σ-*N* diagram

In the finite-life area ($N < N_D$), multiple fatigue tests are run at each stress level (σ_a = const), which always lead to the considerable statistical scatter in the fatigue life (Figure 2.3*a*). However, if the fatigue life *N* is treated as the variable, then an appropriate probability distribution (i.e. probability function) can be obtained, as shown in Figure 2.3*b*. The most important probability distributions when evaluating the fatigue behaviour statistically, are normal (Gaussian), log-normal, and Weibull distributions.

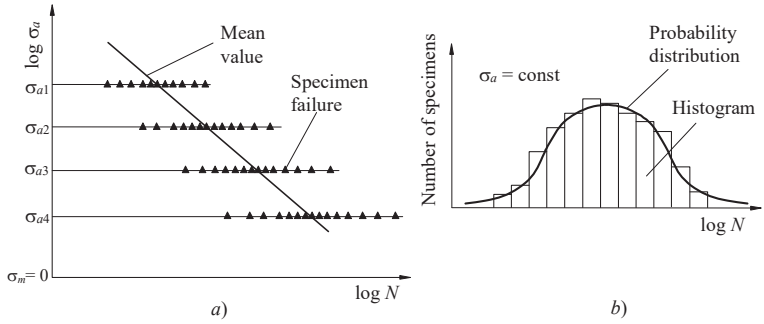

Figure 2.3: Multiple fatigue tests for the statistical evaluation
a) Experimental results, *b*) Histogram for given stress amplitude

In the infinite-life area ($N \geq N_D$), the *staircase method* [2.11] is often used for the statistical evaluation of the fatigue limit σ_{D0} (Figure 2.4). This method is based on the assumption, that the actual specimen is loaded with the stress amplitude σ_a regarding the experimental results already obtained for the previous specimen. If the specimen failed after a limited number of loading cycles N_D, the stress amplitude σ_a in the next specimen decreases, and vice versa. The differences between the statistically evaluated values of the fatigue limit σ_{D0} for a given probability of failure P, and those taken from the professional literature for $P = 0.5$, are mainly dependent on the number of tested specimens, probability function etc. However, the following simplified equation may be used for steel materials [2.11]:

$$\sigma_{D0}^{P} = k_P \cdot \sigma_{D0} \tag{2.5}$$

σ_{D0}^{P} fatigue limit for an arbitrary probability of failure P
σ_{D0} fatigue limit for probability of failure $P = 0.5$
k_P probability coefficient
$k_P = 1.0$ when $P = 0.5$ (50 % probability of failure)
$k_P = 0.897$ when $P = 0.10$ (10 % probability of failure)
$k_P = 0.814$ when $P = 0.01$ (1 % probability of failure)

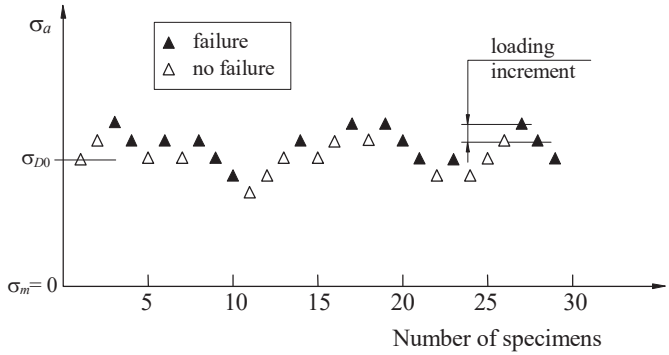

Figure 2.4: The principle of the staircase method for the statistical evaluation of the fatigue limit σ_{D0}

When dimensioning dynamically loaded machine parts or structural components in the infinite-life area, the simplified approach is often used to determine the approximate fatigue strength of the analysed component related only to the ultimate tensile strength R_m of the material. As presented in [2.2, 2.6], the following relation may be considered for steels:

$$\sigma_{D0} \approx (0.4 \ldots 0.6) \cdot R_m \quad \text{when } R_m \leq 1400 \text{ N/mm}^2 \tag{2.6a}$$

$$\sigma_{D0} \approx 700 \text{ N/mm}^2 \quad \text{when } R_m > 1400 \text{ N/mm}^2 \tag{2.6b}$$

It is evident from Eq. (2.6*b*) that for high-strength steels with ultimate tensile strength R_m > 1400 N/mm^2, the fatigue limit σ_{D0} does not increase any more. Thus, there is no reason to use such steels for the dynamic loaded components.

Most *S*–*N* fatigue data available in the literature consist of fully reversed (σ_m = 0 or R = –1) uniaxial fatigue strengths of small, highly polished, unnotched specimens in a laboratory air environment. However, the conditions of real structural components may be very different, and should be considered when determining their fatigue strength. Based on the fatigue strength of standardised specimen σ_{D0}, the fatigue strength of real engineering component σ_D can be determined with consideration of the different influencing factors, as follows:

$$\sigma_D = \sigma_{D0} \cdot C_d \cdot C_{Ra} \cdot C_{others} \tag{2.7}$$

C_d, C_{Ra}, C_{others} … influencing factors

Figure 2.5 shows schematically the influence of some typical parameters on the fatigue strength of real engineering components. The influence of individual parameters is advantageous if the *S*–*N* curve is shifted upwards. However, there are also some other important magnitudes (multiaxial loading, variable amplitude loading) which are discussed in later sections.

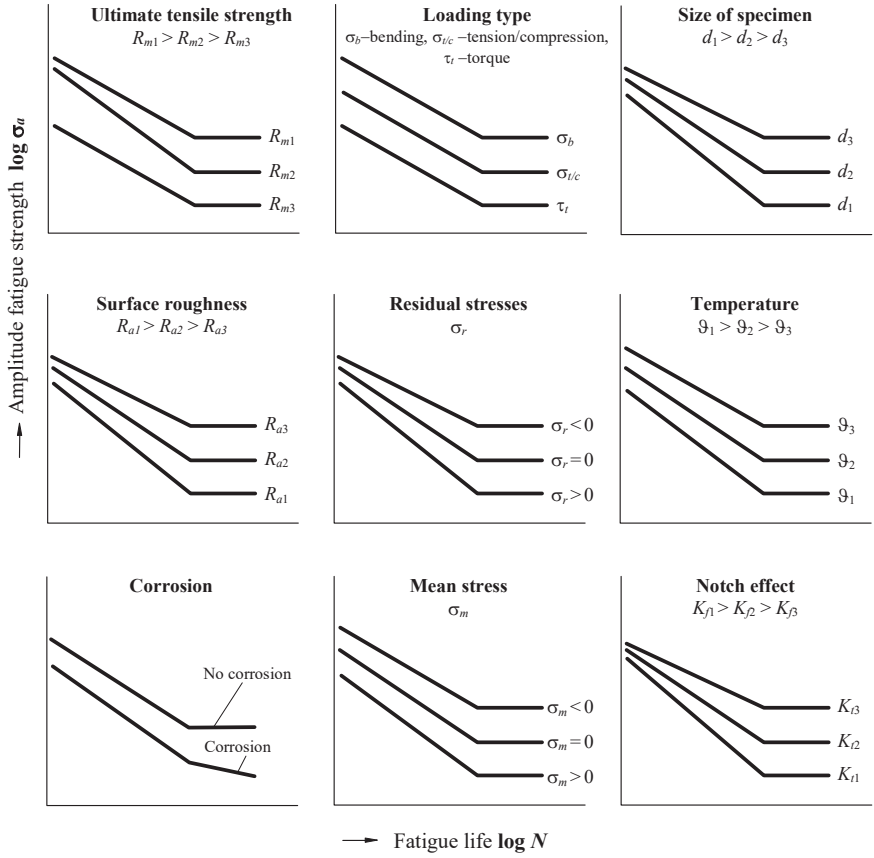

Figure 2.5: Influencing parameters on the fatigue life

2.1.1 Size effect

The standardised experimental testing for determination of the material fatigue parameters (σ_f', b, σ_{D0}) is usually performed on small specimens with the specimen diameter (d) or thickness (t) smaller than 8 mm. For large sizes the fatigue strength decreases, which is primarily the consequence of the higher probability of microstructural discontinuities (non-metallic inclusions, voids, etc.) in the highly stressed surface regions, that contribute to the decrease in fatigue resistance. Furthermore, the *S–N* fatigue resistance under axial (tension/compression) conditions is lower than for bending

conditions. Here, the fatigue limit for axial loading can range from 0.75 to 0.9 of the bending fatigue limit for small specimens ($d \leq 8$ mm). This can be explained with the fact that in axial loading the whole specimen cross-section is subjected to the uniform stress (a stress gradient does not exist). In bending, the stress gradient depends upon the specimen's diameter or thickness (the larger the diameter or thickness, the smaller the bending stress gradient, and, hence, the larger the average stress in a local region of depth h on the surface (see Figure 2.6). In that respect, the following guidelines may be used to consider the size effect on the fatigue limit [2.11]:

Tension/Compression:

$$C_d \leq 1.0 \tag{2.8}$$

Bending:

$$C_d \leq 1.0 \qquad d \leq 8 \text{ mm} \tag{2.9a}$$

$$C_d = \left(\frac{d}{8}\right)^{-0.1133} \qquad 8 \text{ mm} < d \leq 50 \text{ mm} \tag{2.9b}$$

$$C_d = 0.8 \qquad d > 50 \text{ mm} \tag{2.9c}$$

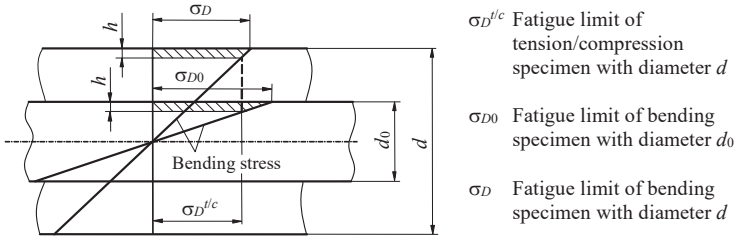

Figure 2.6: Size effect on the bending strength

2.1.2 Effect of surface finish

As presented in the previous section, the fatigue data of engineering materials available in the literature are related mostly to highly polished specimens. If the surface finish of a real component is rougher than the polished surface of a standardised smooth specimen, the fatigue limit, σ_{D0}, is reduced by the *surface finish factor* C_{Ra}. Considering the Eq. (2.7), the fatigue limit of rough engineering component, σ_D, can then be expressed as:

$$\sigma_D = \sigma_{D0} \cdot C_{Ra} \tag{2.10}$$

Figure 2.7 shows the effect of surface finish on the fatigue limit of engineering components made of steels and produced with different production technologies. If a component is not polished, the fatigue limit may be reduced significantly by the appropriate surface finish factor C_{Ra}. Furthermore, a greater degradation of the fatigue limit is obtained for steels with higher ultimate tensile strength R_m. Similar conclusions can also be made from Figure 2.8, where the surface roughness Ra is considered.

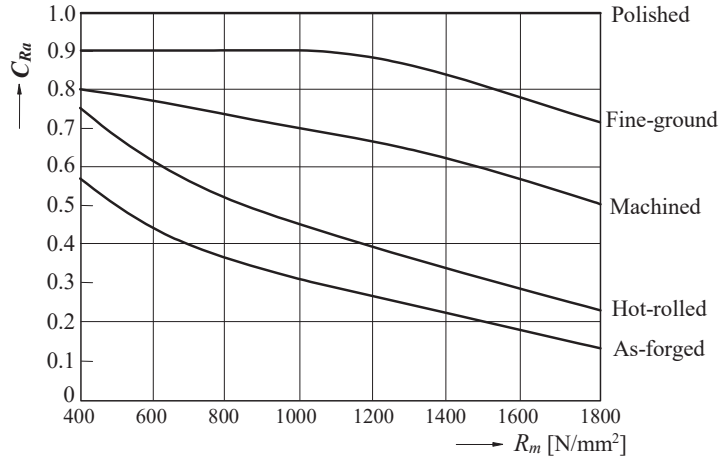

Figure 2.7: Effect of surface finish on the surface finish factor C_{Ra} of steels [2.13, 2.14]

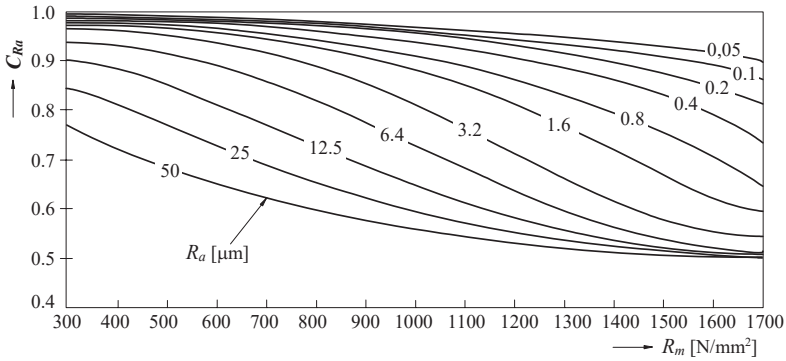

Figure 2.8: Effect of surface roughness R_a on the surface finish factor C_{Ra} of steels [2.15]

2.1.3 Mean stress effect

In general, most *S–N* fatigue data from professional literature are related to the fully reversed rotating bending tests with zero mean stress ($\sigma_m = 0$). However, an arbitrary mean stress (tension or compression) may be applied on the real engineering component. If mean stress ($\sigma_m \neq 0$) is applied, it can have a substantial influence on the fatigue behaviour (Figure 2.9). It is clear that tensile mean stresses are detrimental and compressive mean stresses are beneficial on the fatigue strength. It can be explained by the fact that compressive mean stresses contribute to the crack closure effect, and, consequently, to the higher fatigue strength. The influence of the mean stress on the fatigue strength is often presented by the Haigh diagram as shown principally in Figure 2.10.

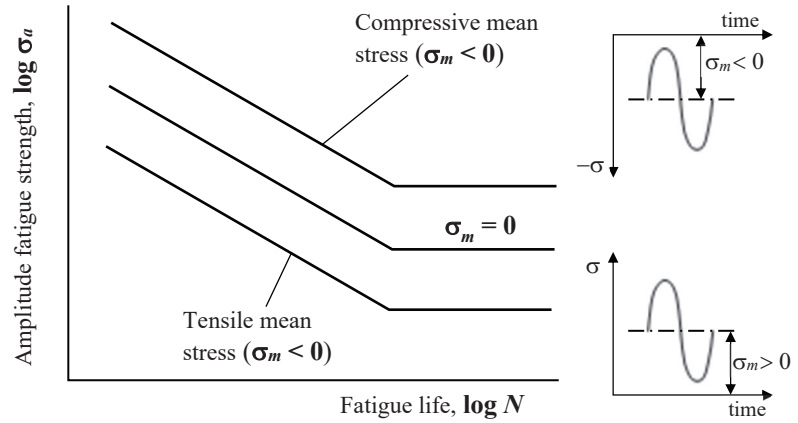

Figure 2.9: Mean stress effect on the *S–N* curve

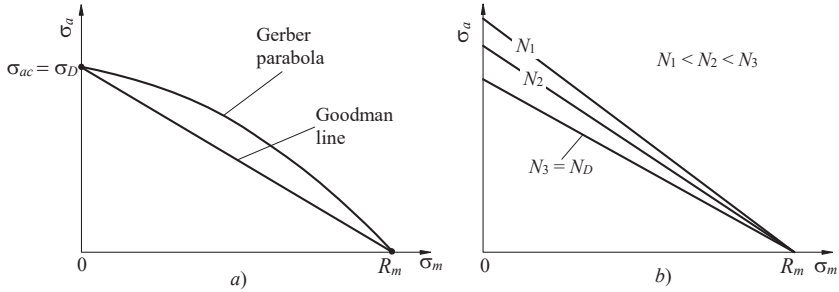

Figure 2.10: Haigh diagram [2.16]
a) Infinite life area ($N \geq N_D$), *b*) Finite-life area ($N < N_D$)

Figure 2.10*a* shows the Haigh diagram for the infinite-life are, where the amplitude strength of the component is presented as a function of the mean stress σ_m. If the structural component is loaded with a mean stress $\sigma_m \neq 0$, the equivalent completely reversed stress amplitude σ_{ac} should be obtained when determining the fatigue life using Eq. (2.4). Here, the following equations describing the Goodman line or Gerber parabola (see Figure 2.10*a*) are often used in engineering praxis:

$$\sigma_{ac} = \frac{\sigma_a}{1 - \frac{\sigma_m}{R_m}} \qquad \text{Goodman line} \qquad (2.11)$$

$$\sigma_{ac} = \frac{\sigma_a}{1 - \left(\frac{\sigma_m}{R_m}\right)^2} \qquad \text{Gerber parabola} \qquad (2.12)$$

where R_m is the ultimate tensile strength of the material. The equivalent completely reversed stress amplitude σ_{ac} actually represents the applied combination of stress amplitude σ_a and mean stress σ_m, which result in the same fatigue life as the stress amplitude σ_{ac} applied at zero mean stress. Besides the equations (2.11) and (2.12), other criteria to determine the value of σ_{ac} may be found in the professional literature [2.17]:

$$\sigma_{ac} = \frac{\sigma_a}{1 - \frac{\sigma_m}{\sigma_f'}} \qquad \text{Modified Goodman (ductile metals)} \qquad (2.13)$$

$$\sigma_{ac} = \sqrt{\sigma_{\max} \cdot \sigma_a} \qquad \text{SWT (Aluminium alloys)} \qquad (2.14)$$

As presented above, the choice of the appropriate criterion for consideration of the mean stress effect is dependent mainly on the material of the analysed structural component. If compression mean stress appears, it may cause a significant increase of the fatigue strength (see Figure 2.11).

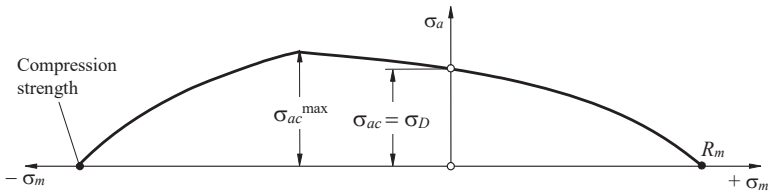

Figure 2.11: Haigh diagram for compression mean stress [2.6]

2.1.4 Notch effect

Machine parts are often comprised of different geometric discontinuities (holes, fillets, keyways, etc.), which are unavoidable in their design. These stress raisers (notches) reduce fatigue strength, and require careful attention in the design process. In the stress-life approach, the notch-effect is taken into account by modifying the unnotched *S–N* curve (see Figure 2.12).

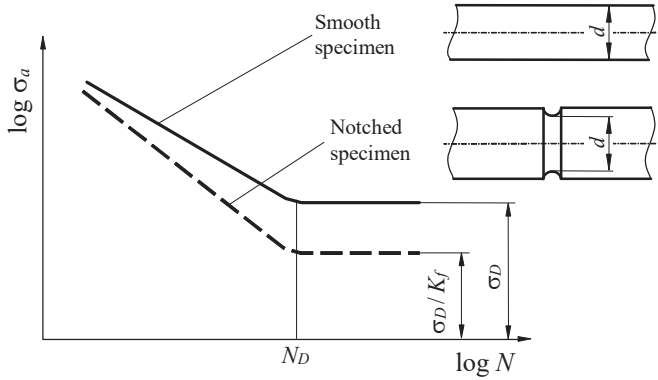

Figure 2.12: *S–N* curve of smooth and notched test specimen

In the infinite-life area ($N \geq N_D$) and zero mean stress ($\sigma_m = 0$), the notch-effect is obtained by the *fatigue notch factor* K_f as follows:

$$K_f = \frac{\text{Fatigue limit of smooth specimen}}{\text{Fatigue limit of notched specimen}} \qquad N \geq N_D;\ \sigma_m = 0 \tag{2.15}$$

In the finite-life area ($N < N_D$) the notch-effect is smaller and is obtained by the *modified fatigue notch factor* K_f' (see Figure 2.13). Here, the fatigue notch factor $K_f{}^*$ should be determined previously (see Figure 2.14).

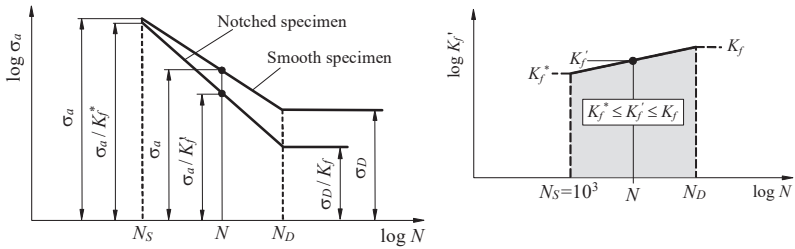

Figure 2.13: Notch-effect in the finite-life area

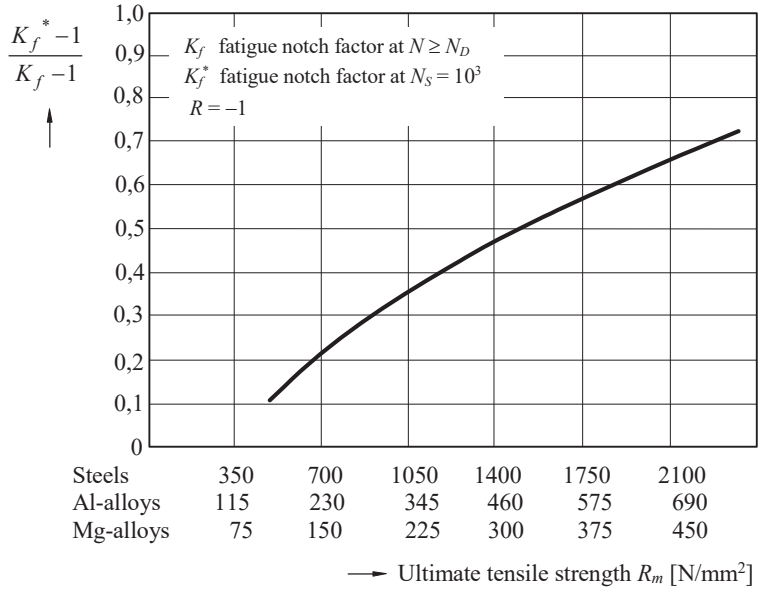

Figure 2.14: Fatigue notch factor K_f^* [2.18]

As shown in Figure 2.12, the appropriate experimental testing on notched specimens should be performed to determine the fatigue notch factor K_f. However, the following empiric equation is often used when dimensioning the dynamic loaded notched components [2.2, 2.4]:

$$K_f = 1 + q \cdot (K_t - 1) \tag{2.16}$$

where K_t is the stress concentration factor and q is the notch sensitivity factor.

Stress concentration factor K_t is defined as the ratio of the maximum stress (stress concentration σ_{conc}) at the notch to the nominal stress σ_{nom} (see Figure 2.15):

$$K_t = \frac{\sigma_{conc}}{\sigma_{nom}} \tag{2.17}$$

where σ_{nom} is always related to the nominal ("net") cross-section of the analysed structural component (i.e. without the hole in Figure 2.15*b*).

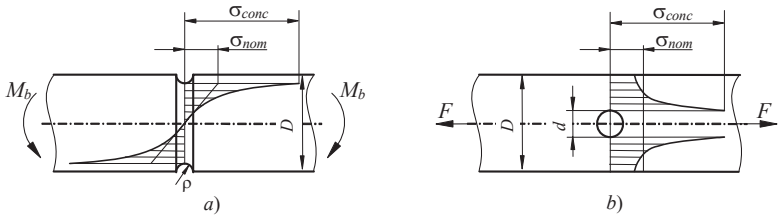

Figure 2.15: Stress concentration around the notch
a) Circular groove in a round bar, *b*) Circular hole in a round bar

Stress concentration factor K_t is the elastic magnitude, and should be determined using the theory of elasticity. The K_t-values for many notch-geometries (see two examples in Figure 2.16) have already been determined in the past and summarised in the professional literature [2.19].

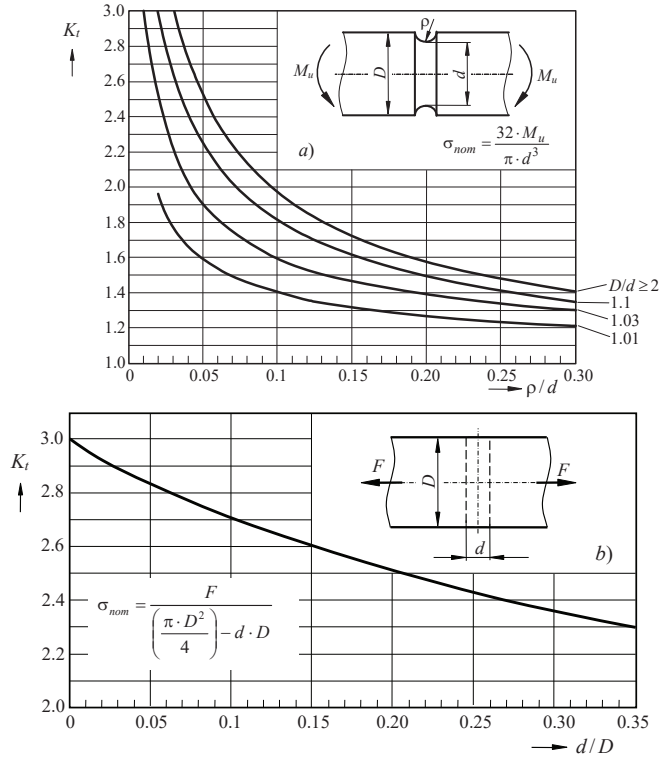

Figure 2.16: Stress concentration factor K_t [2.19]
a) Circular groove in a round bar, *b*) Circular hole in a round bar

Notch sensitivity factor q is the measure of the real notch-effect of the analysed component ($0 \leq q \leq 1$). Namely, the fatigue strength of a notched specimen depends not only on the theoretical stress concentration K_t, but also on other factors, such as the notch radius and the type of material (i.e. hard and brittle material, ductile material, etc.). A value $q = 0$ (or $K_f = 1$) indicates no notch sensitivity, whereas a value $q = 1$ (or $K_f = K_t$) indicates full notch sensitivity.

Values of q may be estimated from the available empirical equations (Neuber, Peterson, etc.) which can be found in the professional literature [2.2, 2.4]. Neuber developed the following approximate formula for the notch sensitivity factor:

$$q = \frac{1}{1 + \sqrt{\frac{C_N}{\rho}}} \qquad N \geq N_D;\ R = -1 \tag{2.18}$$

where ρ in mm is the notch radius and C_N in mm is the Neuber's constant. Values of C_N for steels are shown in Figure 2.17, while for the Al-alloys the following values may be used:

$C_N \approx 2$ mm when $R_m = 150$ N/mm^2
$C_N \approx 0.6$ mm when $R_m = 300$ N/mm^2
$C_N \approx 0.4$ mm when $R_m = 600$ N/mm^2

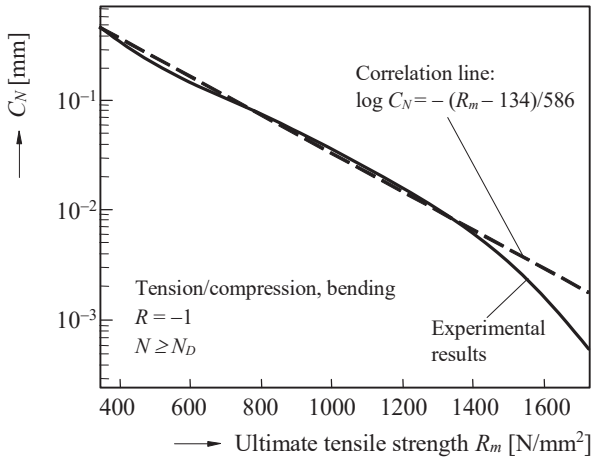

Figure 2.17: Neuber's constant C_N for steels [2.20]

Combined effect of notches and mean stress

The empirical expressions for the fatigue notch factors K_f and K_f' already described in the previous sections are based on the fatigue data observed under completely reversed loading ($\sigma_m = 0$ or $R = -1$). If mean stress is present ($\sigma_m \neq 0$), these expressions cannot be applied directly and some modifications are necessary. The most common approach to consider the combined effect of notches and mean stress (tensile or compressive) is to apply the Goodman diagram (see Section 2.1.3). For a notched component made of ductile material, it follows from the Goodman equation (2.11):

$$\frac{\sigma_D}{K_f} = \frac{\sigma_a}{1 - \frac{\sigma_m}{R_m}} \qquad \text{ductile materials} \tag{2.19}$$

where σ_{ac} is the equivalent completely reversed stress amplitude, σ_a is the stress amplitude, σ_m is the mean stress, R_m is the ultimate tensile strength and K_f is the fatigue notch factor. It is clear from Eq. (2.19) that only long life fatigue strength σ_D is corrected by the fatigue notch factor K_f. It can be explained by the fact that, for ductile materials, the notch-effect on the static strength is small because of the local plastic yielding around the notch. That is not valid for hard and brittle materials where the mean stress correction is also needed (see also Figure 2.18):

$$\frac{\sigma_D}{K_f} = \frac{\sigma_a}{1 - \frac{K_f \cdot \sigma_m}{R_m}} \qquad \text{hard and brittle materials} \tag{2.20}$$

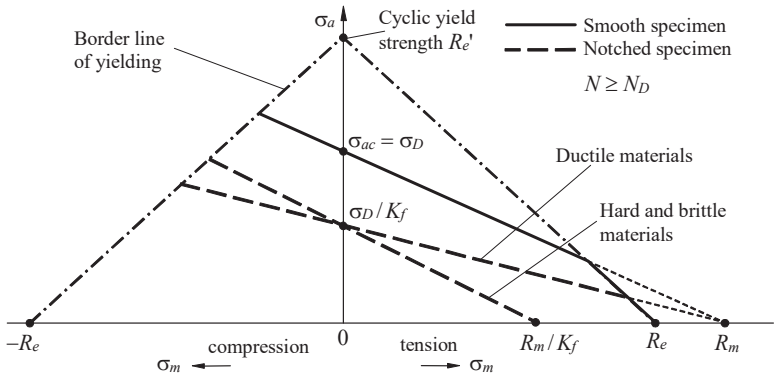

Figure 2.18: Modified Goodman diagram

2.1.5 Multiaxial loading

The basic equation (2.4) and, furthermore, the equations (2.11) to (2.14), represent the common calculation procedure for determination of the fatigue life when uniaxial fatigue loading is applied. However, these equations may also be generalised and used to determine the fatigue life under multiaxial loading. In such cases, the magnitudes σ_a and σ_m in the equations quoted above should be replaced by the equivalent stress amplitude σ_{aE} and the equivalent mean stress σ_{mE}. Once σ_{aE} and σ_{mE} are obtained, the dimensioning procedure is the same as for the uniaxial loading.

Equivalent stress amplitude σ_{aE}

The most commonly used equivalent stress approaches for fatigue are the maximum principal stress theory (Rankine) for hard and brittle materials, and the octahedral shear stress theory (Misses) for ductile materials:

$$\sigma_{aE} = \sigma_{a1} \qquad \text{Rankine} \qquad (2.21)$$

$$\sigma_{aE} = \frac{1}{\sqrt{2}}\sqrt{(\sigma_{a1} - \sigma_{a2})^2 + (\sigma_{a2} - \sigma_{a3})^2 + (\sigma_{a3} - \sigma_{a1})^2} \qquad \text{Misses} \qquad (2.22)$$

where σ_{a1}, σ_{a2} and σ_{a3} are the principal amplitude normal stresses. Once the equivalent stress amplitude, σ_{aE}, is calculated, the multiaxial stress state is reduced to an equivalent uniaxial stress state.

Equivalent mean stress σ_{mE}

If multiaxial mean stresses are present, the equivalent mean stress σ_{mE} is usually obtained as:

$$\sigma_{mE} = \sigma_{m1} + \sigma_{m2} + \sigma_{m3} \qquad (2.23)$$

where σ_{m1}, σ_{m2} and σ_{m3} are principal mean normal stresses which should be considered with the appropriate sign ("+" for tensile mean stress and "–" for compressive mean stress). Therefore, the obtained equivalent mean stress σ_{mE} can be either positive or negative, and, therefore, represents the beneficial effect of compressive mean stress and the detrimental effect of tensile mean stress on the fatigue life correctly.

The equivalent stress approaches described above have commonly been used in the praxis because of their simplicity. However, they should be used only for proportional loading conditions [2.21].

2.1.6 Variable amplitude loading

If more than one amplitude level occurs (variable amplitude loading), the real loading spectrum (Figure 2.19*a*) can be transformed into the loading block (Figure 2.19*b*) with the constant amplitude stress σ_{ai} (i = 1,2, 3 …) inside the loading intervals t_i (i = 1,2, 3 …). Inside the individual loading interval t_i, the amplitude stress σ_{ai} is applied for a number of cycles n_i, while the number of cycles to failure from the *S*–*N* curve (Figure 2.19*c*) is N_i. The

Palmgren-Miner rule simply states that fatigue failure will not appear if the following condition will be satisfied [2.22, 2.23]:

$$\sum_{i=1}^{M} \frac{n_i}{N_i} \leq 1 \tag{2.24}$$

where M is the number of loading intervals inside the analysed loading block (M = 3 for the example in Figure 2.19).

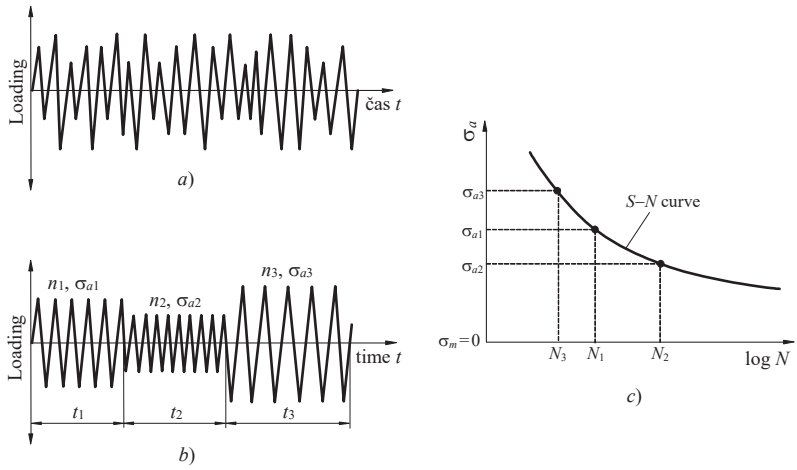

Figure 2.19: The principle of Palmgren-Miner rule for zero mean stress
a) Loading spectrum, *b*) Loading block, *c*) *S* – *N* curve

If the loading block as presented in Figure 2.19b is applied repeatedly for N_B-times, the equation (2.24) may be rewritten as:

$$N_B \cdot \left(\sum_{i=1}^{M} \frac{n_i}{N_i} \right) \leq 1 \tag{2.25}$$

In general, loading intervals t_i inside the loading block may also contain the mean stresses (see Figure 2.20*a*). In such cases, the appropriate mean stress approach (i.e. the Goodman approach in Figure 2.20*b*) should be considered when determining the equivalent completely reversed strain amplitudes σ_{ac}, and, consequently, the number of cycles to failure N_i in each loading interval. In addition, the stress ranges caused by changing the mean stress level also need to be considered in summing the cycle rations n_i/N_i in the Palmgren-Miner equation. For example, one additional cycle ($n_3 = 1$) needs to be considered for amplitude-mean combinations (σ_{a1}, σ_{m1}) and (σ_{a2}, σ_{m2}) in Figure 2.20*a*. It is evident that the cycle (σ_{a3}, σ_{m3}) may cause most of the fatigue damage if σ_{a1} and σ_{a2} are small.

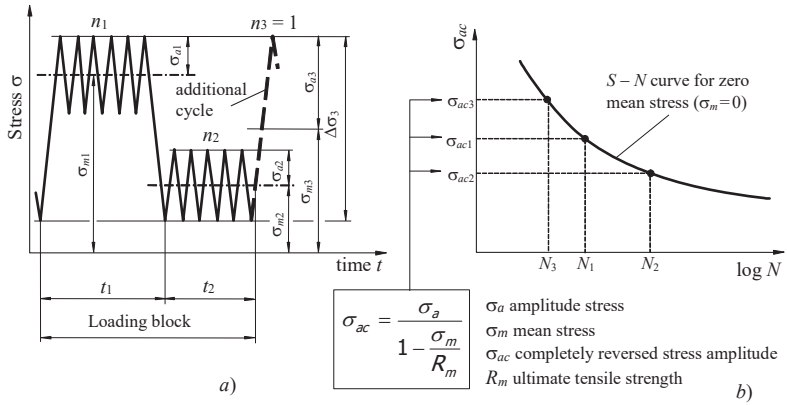

Figure 2.20: The principle of the Palmgren-Miner rule for $\sigma_m \neq 0$
a) Loading block, *b*) *S – N* curve

The important task when dimensioning the structural components under variable amplitude loading is to determine the arranged loading block from the completely stochastic loading spectrum (Figure 2.21). The *cycle counting methods* (Rainflow method [2.24], Level-Crossing method [2.25] etc.) are usually used for that purpose in praxis.

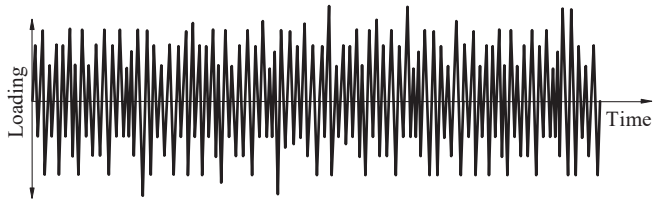

Figure 2.21: Stochastic loading spectrum

2.1.7 Residual stresses

Residual stresses are defined as internal stresses in the component without any external load. The residual stresses may be induced due to machining, thermal treatment, plastic deformation, plating, etc. If residual stresses are induced, they always act as a combination of tensile and compressive residual stresses which are in the reciprocal equilibrium. If compressive residual stresses exist on the surface (Figure 2.22*b*), they can improve the fatigue strength of the analysed component significantly. The most widely used mechanical processes for producing beneficial compressive surface residual stresses are shot-peening and surface rolling [2.2, 2.4].

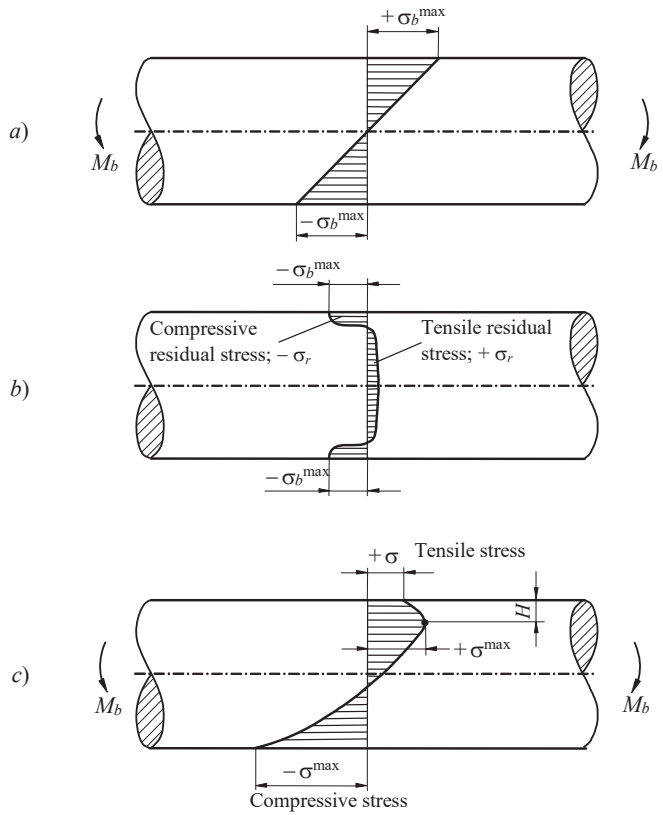

Figure 2.22: The normal stress distribution in a cross-section of a bending specimen
a) Pure bending loading, *b*) Residual stress distribution, *c*) Combined stress

2.1.8 Temperature

The material fatigue parameters (the fatigue limit σ_{D0}, the fatigue strength coefficient σ_f' and the fatigue strength exponent *b*), taken from the professional literature, are generally related to the room temperature (ϑ = 20 °C). If a structural component is subjected to significantly lower or higher temperature, the temperature-effect should be considered when determining its fatigue life.

Low-temperature

The experimental results of many authors [2.6, 2.26, 2.27] have shown that the fatigue limit of polished unnotched specimens increases with the low temperatures (see the example in Figure 2.23). Similar conclusions can also be made for the finite-life area ($N < N_D$). However, the situation may change significantly for notch components and/or components with rough surfaces. Namely, at low-temperatures the material becomes more brittle, and, consequently, more sensitive to the appearance of notches or surface roughness.

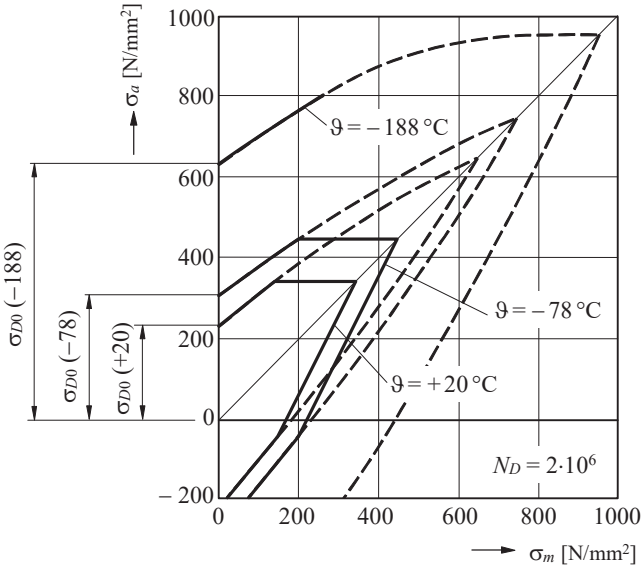

Figure 2.23: Smith diagram for a polished unnotched specimen made of E295 steel [2.6]

High-temperature

Many components in most fields of engineering (automobile and aircraft engines, power, chemical and nuclear plants, etc.) are often subjected to fatigue at elevated temperatures. Figure 2.24 provides a very comprehensive overview of the high-temperatures' effect on the fatigue limit of some common engineering materials. In all cases except for mild steel and cast iron, fatigue limit decreases with increasing temperature. This anomaly for

mild steel and cast iron is probably due to cyclic strain ageing, and is accompanied by a decrease in ductility.

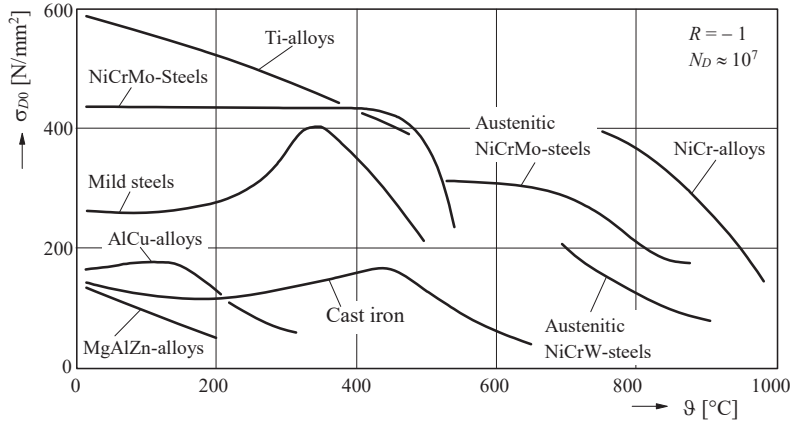

Figure 2.24: Fatigue limit of some metals at high temperatures [2.28]

Creep. If the component is subjected to the extremely high temperature for a long time, a creep deformation should be considered when determining its service life. *Creep* is defined as the thermally assisted, time-dependent deformation under constant external loading. The temperature regime for which creep plays a dominant role in material deformation is typically $\vartheta > 0.5 \cdot \vartheta_m$, where ϑ_m is the melting temperature of the material.

Thermal fatigue. Repeated heating and cooling can cause cyclic stress due to differential thermal expansion and contraction, resulting in *thermal fatigue*. The typical components subjected to thermal fatigue are turbine blades, parts of engines, etc. As presented in [2.16], the resistance against thermal fatigue increases with the quotient $(\sigma_{D0} \cdot \lambda)/(E \cdot \alpha)$, where σ_{D0} is the fatigue limit, E is the Young's modulus, λ is the thermal conductivity, and α is the coefficient of thermal expansion.

2.2 Strain-life approach

The *Strain–life approach* is based on the knowledge of strains (especially plastic strains) that occur at locations where fatigue crack nucleation is likely to start, such as holes (Figure 2.25*a*), fillets, grooves, etc. The effect of local yielding is then investigated on the smooth axial test specimens

(Figure 2.25*b*) under similar conditions as already appear near the notch of the structural component.

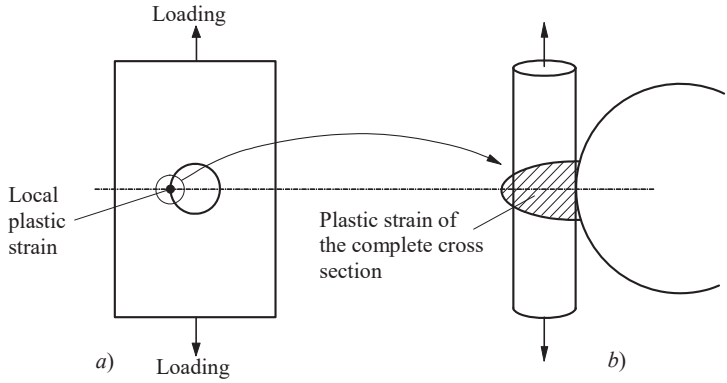

Figure 2.25: The principle of the strain-based approach
a) Local plastic strain around the notch of a real component, *b*) Plastic strain of the complete specimen's cross-section

The strain-life approach is a comprehensive approach, which can be applied for determining the fatigue life of structural components in both Low-Cycle Fatigue (LCF) and High-Cycle Fatigue (HCF) regimes. In the low-cycle region, the component of plastic strain is dominant, while in the high-cycle region the elastic strain component is dominant. From that perspective, ductile materials have better fatigue resistance at large strain, whereas the material strength is the crucial parameter against fatigue failure at smaller strains.

The strain-life approach can also be used in combination with the fatigue crack growth approach (see the introduction of this Chapter) to obtain the number of stress cycles N_i required for the fatigue crack initiation according to equation (2.1). From this point of view, the Safe-Life Design criterion and the Fail-Safe Design criterion are usually used when determining the total fatigue life of cyclic loaded components.

2.2.1 Theoretical background

Engineering and true stress-strain behaviour

Monotonic (static) behaviour of the material is usually obtained from a tension test in which a specimen with a circular cross-section A_0 within the uniform gauge length l_0 (Figure 2.26) is subjected to a monotonically increasing tensile force F until fracture [2.29]. Monotonic uniaxial stress-strain behaviour can be based on *engineering* or *true* stress-strain relationships as follows:

$$\sigma = \frac{F}{A_0} \qquad \text{Engineering stress} \qquad (2.26)$$

$$\sigma = \frac{F}{A} \qquad \text{True stress} \qquad (2.27)$$

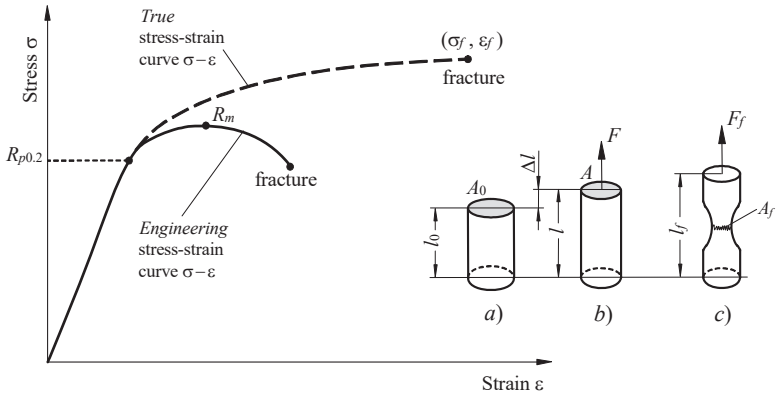

Figure 2.26: Engineering and true stress-strain behaviour
a) Initial gauge section, *b*) Elongated gauge section, c) Gauge section at fracture

It is evident from Figure 2.26 that engineering and true stress-strain curves almost coincide up to the yield stress $R_{p0.2}$, while significant differences appear in the plastic area. Considering this fact, it can be concluded that the true stress-strain relationship should be considered when dimensioning the structural components using a strain-based approach. Here, the true fracture strength, σ_f, can be obtained from F_f / A_f, which is usually corrected for necking. In a similar way, the true fracture strain ε_f is defined as:

$$\varepsilon_f = \ln\frac{l_f}{A_0} = \ln\frac{A_0}{A_f} \tag{2.28}$$

Figure 2.27 shows the true stress-strain behaviour in the elastic and plastic areas. The total strain, ε, is composed from the elastic (ε_e) and plastic (ε_p) part as follows:

$$\varepsilon = \varepsilon_e + \varepsilon_p = \frac{\sigma}{E} + \left(\frac{\sigma}{K}\right)^{\frac{1}{n}} \tag{2.29}$$

where E is the Young's modulus, K is the strength coefficient and n is the strain hardening exponent. The equation (2.29) is often referred to as the "Ramberg-Osgood relationship".

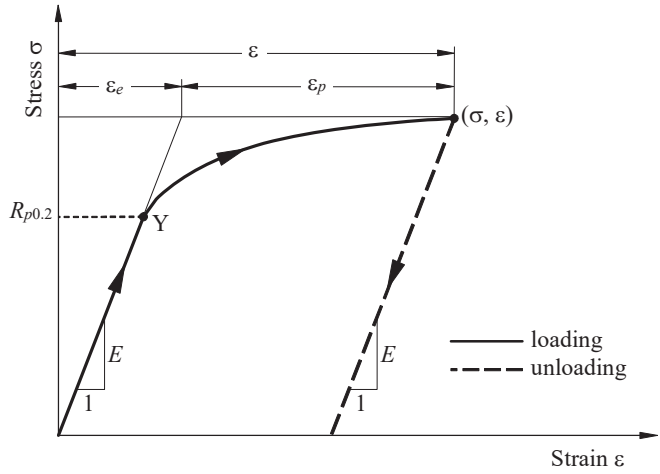

Figure 2.27: True stress-strain behaviour in the elastic and plastic areas

True stress-strain behaviour under cyclic loading

The true stress-strain behaviour under cyclic loading can be quite different from that obtained under monotonic loading, as already described above. The standardised tension/compression cyclic tests [2.30] under strain control (Δε = const) are usually performed to obtain the appropriate stress response, where *cyclic hardening* (Figure 2.28*a*) or *cyclic softening* (Figure 2.28*b*) may appear if stress exceeds the yield stress of the material. Cyclic hardening indicates increased resistance to deformation, whereas cyclic softening indicates the opposite effect. In general, ductile materials (n >

0.15) are usually subjected to the cyclic hardening, while hard and brittle material ($n < 0.15$) are subjected to the cyclic softening [2.16].

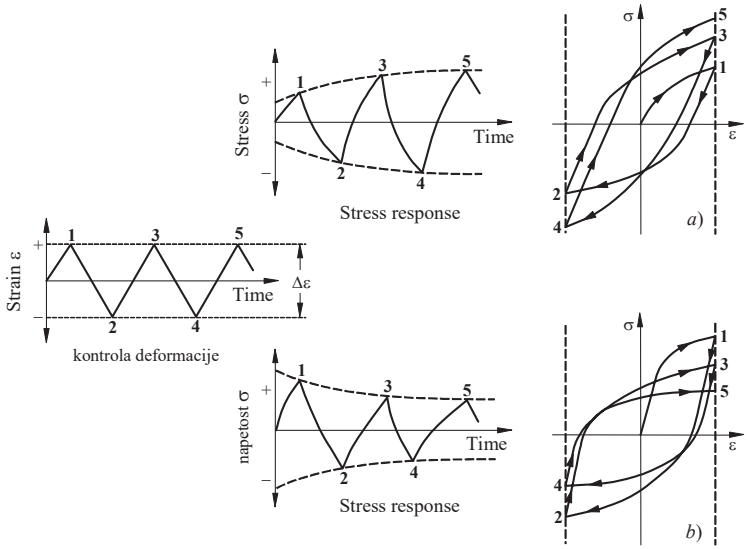

Figure 2.28: Stress response under cyclic loading in the plastic area
a) Cyclic hardening, *b*) Cyclic softening

Changes in cyclic stress responses are more pronounced at the beginning of cyclic loading. As presented in [2.2], most of the materials usually stabilised gradually with continued cyclic loading and a *stable hysteresis loop* forms within 10 to 40 percent of the total fatigue life (see Figure 2.29).

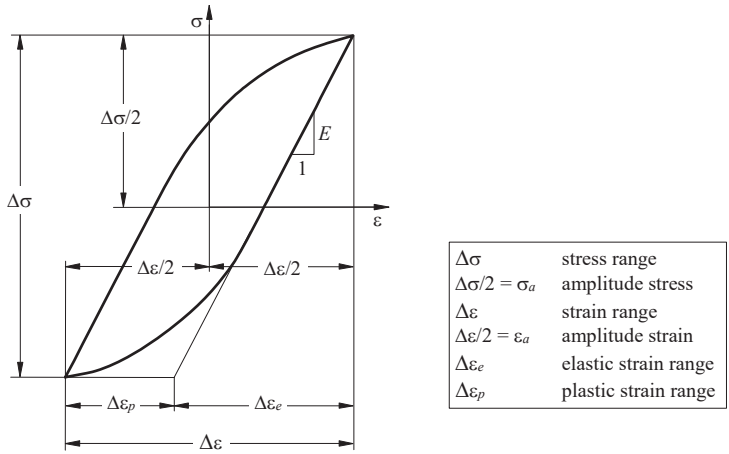

Figure 2.29: Stable cyclic stress-strain hysteresis loop

A family of stabilised hysteresis loops at different strain ranges can be used to obtain the *cyclic stress-strain curve* for a given material. If the *multi-specimen method* is used, each specimen is subjected to a constant strain range ($\Delta\varepsilon_1$, $\Delta\varepsilon_2$, $\Delta\varepsilon_3$, etc.; Figure 2.30*a*) until fracture occurs. Near half-life hysteresis loops from each specimen are then used to obtain the cyclic stress-strain curve (Figure 2.30*b*), which can be divided into the elastic and plastic areas (Figure 2.31)

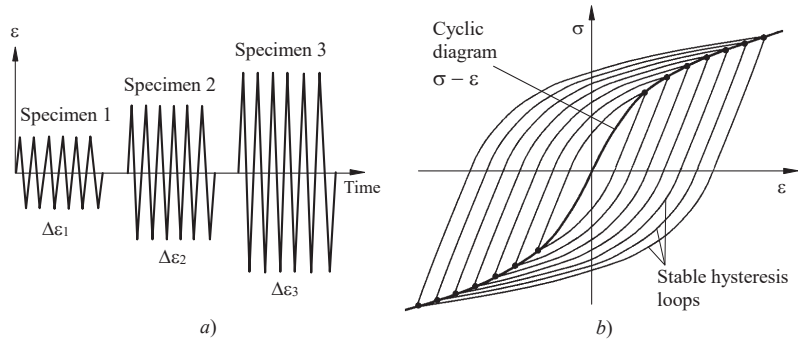

Figure 2.30: Cyclic behaviour under different strain ranges
a) Multi-specimen method, *b*) Cyclic stress-strain curve

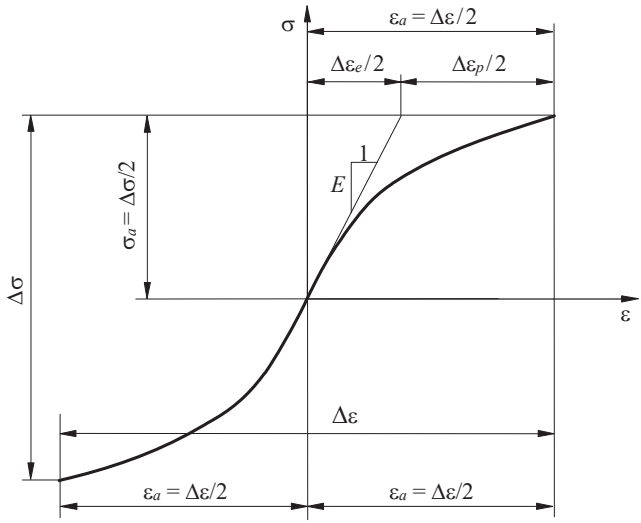

Figure 2.31: Cyclic stress-strain curve in the elastic and plastic areas

Similar to the monotonic loading, the Ramberg-Osgood relationship (equation 2.29) can be modified as follows for the cyclic loading:

$$\varepsilon_a = \frac{\Delta\varepsilon}{2} = \frac{\Delta\varepsilon_e}{2} + \frac{\Delta\varepsilon_p}{2} = \frac{\sigma_a}{E} + \left(\frac{\sigma_a}{K'}\right)^{\frac{1}{n'}} \tag{2.30}$$

where ε_a is the amplitude strain, σ_a is the amplitude stress, E is the Young's modulus, K' is the cyclic strength coefficient and n' is the cyclic strain hardening exponent.

Strain-life curves

Strain-life curves are derived from fatigue tests under completely reversed ($R = -1$) axial cyclic loading according to the ASTM E606 Standard [2.30]. The experimental results are plotted on log-log scales (Figure 2.32), where N_i or $2N_i$ are the number of cycles or reversals to failure, respectively. Failure criteria may be the life to a small detectable crack, life to a certain percentage decrease in tensile load, life to a certain decrease in the ratio of unloading to loading Young's modulus, or life to fracture. The total strain amplitude (ε_a) can be resolved into elastic ($\Delta\varepsilon_e/2$) and plastic ($\Delta\varepsilon_e/2$) strain amplitudes from the stabilised hysteresis loop (see Figure 2.29).

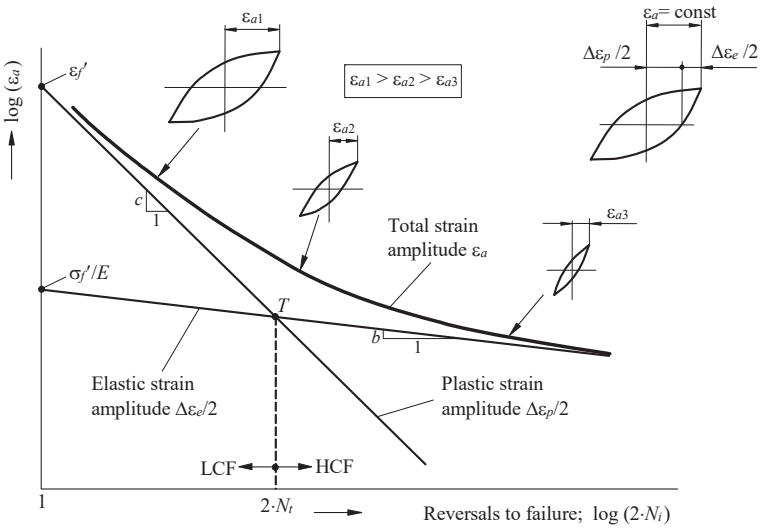

Figure 2.32: Strain-life curves

The strain-life curves presented in Figure 2.32 can be expressed mathematically as the Coffin-Manson relationship [2.31, 2.32]:

$$\varepsilon_a = \frac{\Delta\varepsilon_e}{2} + \frac{\Delta\varepsilon_p}{2} = \frac{\sigma_f{}'}{E}(2N_i)^b + \varepsilon_f{}'(2N_i)^c \tag{2.31}$$

where ε_a is the total amplitude strain, E is the Young's modulus, σ_f' is the fatigue strength coefficient, b is the fatigue strength exponent, ε_f' is the fatigue ductility coefficient and c is the fatigue ductility exponent. To obtain N_i for a given value of ε_a, the mathematical form of this equation requires either a graphical or numerical solution. The low-cycle fatigue parameters σ_f', b, ε_f' and c are considered to be material properties and can be, for many engineering materials, taken from the appropriate professional literature. Otherwise, these parameters should be determined experimentally according to the ASTM E606 Standard [2.30].

The elastic and plastic strain curves in Figure 2.32 can be approximated as straight lines. At large strain or short lives, the plastic strain component is predominant, and at small strain or longer lives the elastic strain component is predominant. The intersect of the two straight lines at $2N_i$ is called the *transition fatigue life*, and represents the transition point between Low

Cycle Fatigue (LCF) and High Cycle Fatigue (HCF). The value $2N_i$ can be obtained from the equation (2.31) considering $\Delta\varepsilon_e/2 = \Delta\varepsilon_p/2$:

$$2N_i = \left(\frac{\varepsilon_f{}' \cdot E}{\sigma_f{}'}\right)^{\frac{1}{b-c}} \tag{2.32}$$

The large amount of strain-life data available in the literature permits some generalisations and trends to be stated concerning strain-life approach when dimensioning the cyclic loaded engineering components. Figure 2.33 shows schematically the fatigue behaviour of different groups of materials (ductile, tough, strong) under a strain-controlled cyclic test. At large strains, increased life is dependent more on ductility, whereas at small strains longer life is obtained for strong (i.e. hard and brittle) materials. It is clear that the optimum overall strain-life behaviour may be established for tough materials, which represent a good combination of strength and ductility. Furthermore, a characteristic strain amplitude $\varepsilon_a \approx 0.01$ may be detected at which all groups of materials demonstrate a similar fatigue life $N_i \approx 10^3$ cycles.

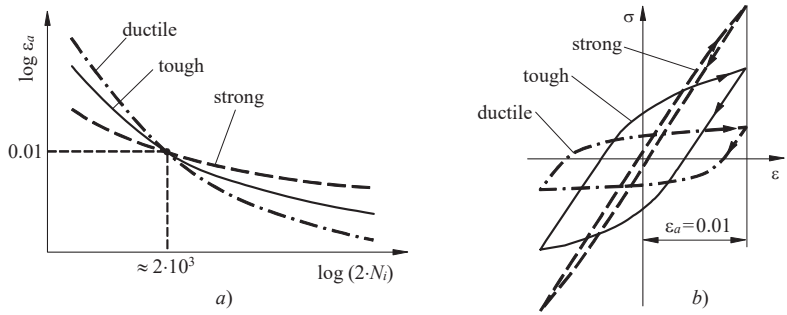

Figure 2.33: Characteristic cyclic behaviour of different materials
a) Diagram log (ε_a) – log ($2N_i$), *b*) Stable hysteresis loops

Most strain-life material data (σ_f', ε_f', b and c) available in the literature are related to the fully reversed ($R = -1$) uniaxial fatigue tests under "ideal" loading conditions (small highly polished unnotched specimens, laboratory air environment, etc.). However, the conditions when operating real structural components may be very different, and should be considered when determining their fatigue life using the strain-based approach. In contrast to the stress-life approach at long lives, strain-life curves at short

lives are not highly sensitive to some influencing factors (surface finish, residual stresses), which is described briefly in the following sections.

2.2.1 Size effect

The standardised experimental testing for determination the material fatigue parameters (σ_f', ε_f', b and c) is usually performed on the small cylindrical specimens. As already presented in Section 2.1.1, the fatigue strength decreases with the size (diameter) of the specimen. However, the investigations related to the size effect in the strain-life approach are very limited. In one study [2.4] related to shafts made of low-carbon and low-alloy steels, the size reduction factor, C_d, was found to vary with shaft diameter, d [mm], as follows:

$$C_d = \left(\frac{d}{25.4}\right)^{-0.093} \tag{2.33}$$

Once the size reduction factor has been obtained, the material parameters σ_f' and ε_f' should be corrected in the following way:

$$\sigma_{fd}' = C_d \cdot \sigma_f' \; ; \qquad \varepsilon_{fd}' = C_d \cdot \varepsilon_f' \tag{2.34}$$

2.2.2 Effect of surface finish

Since fatigue cracks often nucleate relatively early in the LCF-region due to large plastic strains, there is usually little influence of surface finish at short lives ($N_i < N_t$). Conversely, there is more influence in the HCF-regime at long lives ($N_i > N_t$), where the elastic strain is dominant. Therefore, only the elastic strain-life curve should be modified to account for the surface finish effect. This is done by reducing the slope of the elastic strain-life curve from b to b', as shown schematically in Figure 2.34. The new fatigue strength exponent b' can be obtained from the fatigue limits of polished (σ_D) and rough ($C_{Ra} \cdot \sigma_D$) specimens as follows:

$$b' = b + \frac{\log C_{Ra}}{\log(2N_D)} \tag{2.35}$$

where b is the fatigue strength exponent of the polished specimen, C_{Ra} is the surface finish factor (see Section 2.1.2) and N_D is the number of loading cycles at the knee of the S–N curve. This approach for surface finish correction can also be used for nonzero mean stress loadings ($\sigma_m \neq 0$).

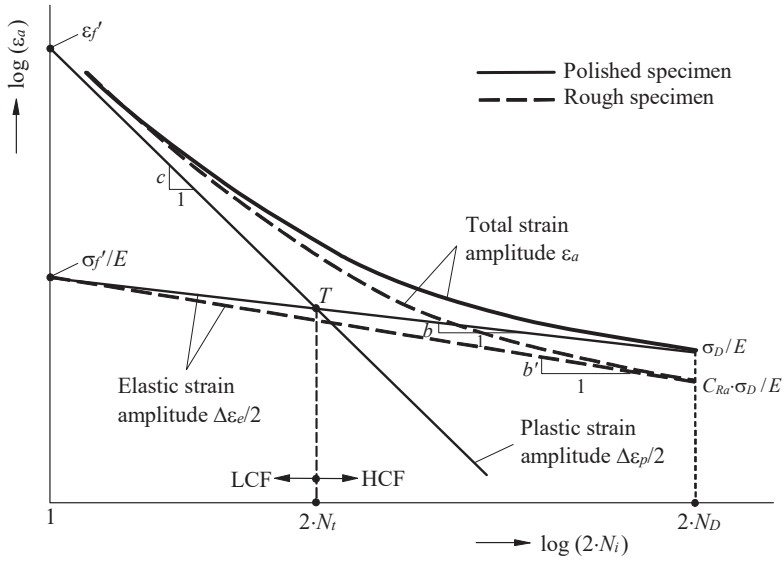

Figure 2.34: Effect of surface finish on the strain-life curves

2.2.3 Mean stress effect

The strain-controlled fatigue behaviour discussed in the previous sections was related to the completely reversed straining (ε_m=0 or $R = \varepsilon_{min}/\varepsilon_{max} = -1$). If a nonzero mean strain ($\varepsilon_m \neq 0$) is present it should be considered when determining the fatigue life using the strain-life approach. However, the stain-controlled cyclic loading with a given mean strain often results in a mean stress relaxation, as shown in Figure 2.35. The amount of mean stress relaxation depends mostly on the plastic strain amplitude involved during the cyclic loading (there is more mean stress relaxation at larger strain amplitudes, and vice versa). Based on this finding it can be concluded that the mean stress effect on the fatigue life is smaller in the LCF-region and larger in the HCF-region.

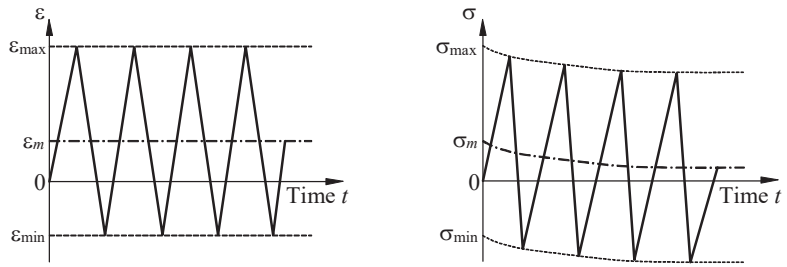

Figure 2.35: Mean stress relaxation under strain-controlled cyclic loading
ε_m- mean strain; σ_m- mean stress

Alternatively, stress-controlled tests can be run where no mean stress relaxation appears. If such tests are run in the plastic region of the material, the *cycle-dependent creep* can occur (Figure 2.36), which may result in a fatigue failure similar to that from a tension test.

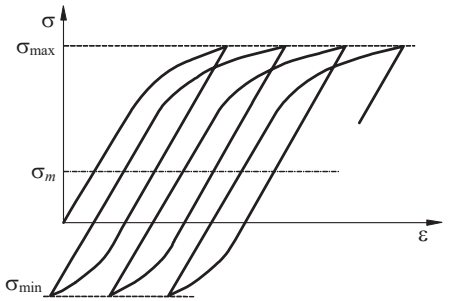

Figure 2.36: Principle of the cycle-dependent creep

The general effect of mean stress on the fatigue life was discussed in Section 2.1.3. However, the consideration of mean stress in the strain-life approach is more complex, and, for that reason, only a few approaches are presented briefly in the continuation of this section.

Morrow's approach

This approach [2.33] simply replaces σ_f' with $(\sigma_f' - \sigma_m)$ in equation (2.31):

$$\varepsilon_a = \frac{\Delta\varepsilon_e}{2} + \frac{\Delta\varepsilon_p}{2} = \frac{\sigma_f{}' - \sigma_m}{E}(2N_i)^b + \varepsilon_f{}'(2N_i)^c \quad (2.36)$$

where σ_m is the mean stress which should be considered with the appropriate sign ("–" for compressive mean stress, "+" for tensile mean stress). Equation (2.36) indicates clearly that compressive mean stress is beneficial and tensile mean stress is detrimental when determining the fatigue life using the strain-based approach. Morrow's approach gives a good result for large plastic strains (short fatigue life) where mean stress effect is small because of its relaxation.

Manson's approach

In this approach [2.34] both the elastic and plastic terms are affected by the mean stress σ_m:

$$\varepsilon_a = \frac{\Delta\varepsilon_e}{2} + \frac{\Delta\varepsilon_p}{2} = \frac{\sigma_f{}' - \sigma_m}{E}(2N_i)^b + \varepsilon_f{}'\left(\frac{\sigma_f{}' - \sigma_m}{\sigma_f{}'}\right)^{\frac{c}{b}}(2N_i)^c \quad (2.37)$$

Manson's approach is, in general, suitable for steels, but it is often inaccurate for aluminium alloys.

SWT approach

The Smith-Watson-Topper (SWT) approach [2.35] is based on the assumption that for different combinations of strain amplitude, ε_a, and means stress, σ_m, the product $\sigma_{max} \cdot \varepsilon_a$ remains constant for a given life:

$$\sigma_{max}\varepsilon_a E = \left(\sigma_f{}'\right)^2(2N_i)^{2b} + \sigma_f{}'\varepsilon_f{}'E(2N_i)^{b+c}\,; \quad \sigma_{\max} > 0 \quad (2.38)$$

where $\sigma_{max} = \sigma_m + \sigma_a$. The SWT approach gives acceptable results for a wide range of materials. It is generally not as accurate for steels as Manson's approach, but it is quite good for aluminium alloys.

2.2.4 Notch effect

As already presented in the introduction of this Chapter, the strain–life approach is a common application in the fatigue analysis of notched members. This is because local yielding is often involved at the notch root and, therefore, fatigue behaviour is best described in terms of strain.

Figure 2.37 shows the tensile loaded plate with a circular hole where the notch root and nominal stresses and strains are represented by (σ, ε) and (σ_{nom}, ε_{nom}), respectively. As long as stresses and strains at the notch root remain elastic, it follows that

$$\sigma = K_t \cdot \sigma_{nom};\ \varepsilon = K_t \cdot \varepsilon_{nom} \tag{2.39}$$

where K_t is the elastic stress concentration factor (see Section 2.1.4). However, when local stress at the notch root exceeds the yield strength of the material, the equation (2.39) should be modified in the following way

$$\sigma = K_\sigma \cdot \sigma_{nom};\ \varepsilon = K_\varepsilon \cdot \varepsilon_{nom} \tag{2.40}$$

where K_σ and K_ε are the stress and strain concentration factors, respectively.

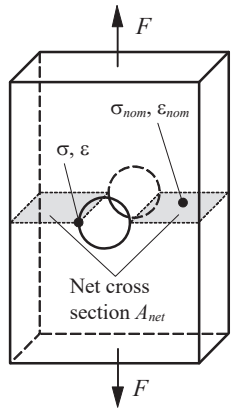

σ_{nom} nominal stress; $\sigma_{nom} = F/A_{net}$
ε_{nom} nominal strain
σ local stress at the notch
ε local strain at the notch

Figure 2.37: Definitions of notch and nominal stresses and strains

A schematic variation of stress and strain concentration factors (K_σ and K_ε) with the notch stress (σ) is shown in Figure 2.38. As long as the notch stress remains elastic ($\sigma < R_e$), we have $K_\sigma = K_\varepsilon = K_t$. When notch stress exceeds the yield strength R_e, K_σ decreases and K_ε increases due to plastic deformation at the notch.

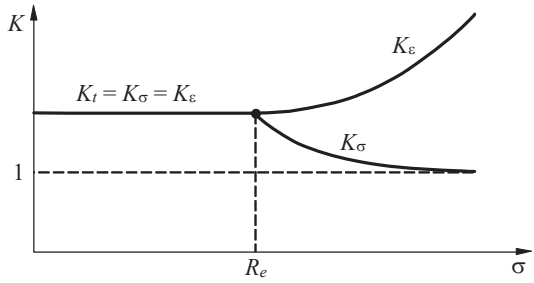

Figure 2.38: Stress and strain concentration factors versus notch stress

The appropriate values of stress and strain concentration factors (K_σ and K_ε) can be obtained experimentally, numerically (usually by means of the Finite Element Method) or analytically by using some empirical equations (i.e. Neuber's rule, Linear rule and Glinka's rule).

Neuber's rule

Neuber's rule is suitable for studying the notch-effect in the case of plane stress conditions (i.e. a notch in a thin plate). Neuber [2.36] derived the following relations between K_σ, K_ε and K_t:

$$\sigma \cdot \varepsilon = {K_t}^2 \cdot \sigma_{nom} \cdot \varepsilon_{nom} \qquad \text{Monotonic loading} \qquad (2.41a)$$

$$\Delta\sigma \cdot \Delta\varepsilon = {K_t}^2 \cdot \Delta\sigma_{nom} \cdot \Delta\varepsilon_{nom} \qquad \text{Cyclic loading; } \sigma_m = 0 \qquad (2.41b)$$

For cyclic loading, Topper et al [2.37] have suggested to replace the elastic stress concentration factor K_t with the fatigue notch factor K_f because of better agreement with the experimental fatigue life results. Therefore, the equation (2.39) can be modified as:

$$\Delta\sigma \cdot \Delta\varepsilon = {K_f}^2 \cdot \Delta\sigma_{nom} \cdot \Delta\varepsilon_{nom} \qquad (2.42)$$

The cyclic behaviour regarding strain and stress amplitude, ε_a and σ_a, respectively, may be defined by the Ramberg-Osgood relationship (Section 2.2.1). Considering $\sigma_a=\Delta\sigma/2$ and $\varepsilon_a=\Delta\varepsilon/2$, it follows from equation (2.30):

$$\Delta\varepsilon = \frac{\Delta\sigma}{E} + 2\left(\frac{\Delta\sigma}{2K'}\right)^{\frac{1}{n'}} \qquad (2.43)$$

where E is the Young's modulus, K' is the cyclic strength coefficient and n' is the cyclic strain hardening exponent.

When nominal stress and strain ranges ($\Delta\sigma_{nom}$ and $\Delta\varepsilon_{nom}$) fall into the elastic area ($\Delta\sigma_{nom} = E \cdot \Delta\varepsilon_{nom}$), it follows from equations (2.42) and (2.43):

$$\frac{\Delta\sigma^2}{E} + 2\Delta\sigma\left(\frac{\Delta\sigma}{2K'}\right)^{\frac{1}{n'}} = \frac{\left(K_f \cdot \Delta\sigma_{nom}\right)^2}{E} \tag{2.44}$$

Equation (2.42) has only one unknown parameter ($\Delta\sigma$), and can be solved iteratively. If nonzero mean stress is present ($\sigma_m \neq 0$), the final solution may be obtained step by step, as illustrated in Figure 2.39 [2.2]. Knowing $\Delta\sigma$, $\Delta\varepsilon$ and σ_{max}, we can obtain $\varepsilon_a = \Delta\varepsilon/2$, and $\sigma_m = \sigma_{max} - \Delta\sigma/2$. Notch strain amplitude, ε_a, and notch mean stress, σ_m, are then used for determination the fatigue life using equations (2.36) to (2.38).

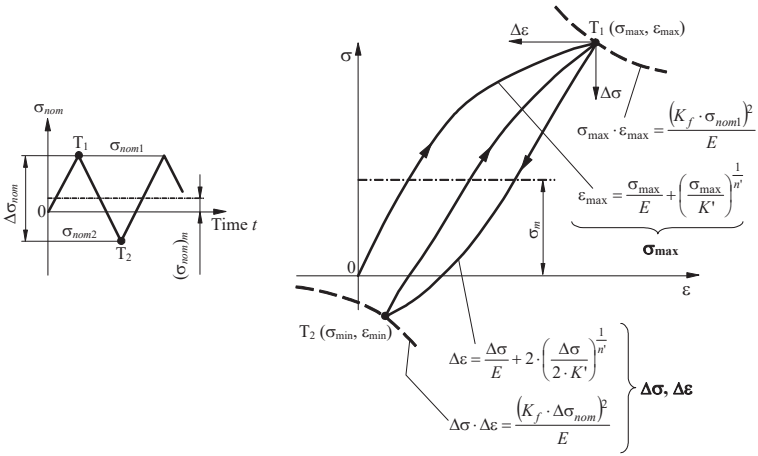

Figure 2.39: Determination of notch stress/strain ranges by Neuber's rule

Linear rule

Linear rule is suitable for studying the notch-effect in the case of plane strain conditions (i.e. a notch in a thick plate), where stresses and strains at the notch root are mostly elastic. This rule is expressed as [2.2]:

$$K_\varepsilon = K_t = \frac{\varepsilon}{\varepsilon_{nom}} \qquad \text{Monotonic loading} \qquad (2.45a)$$

$$\Delta\varepsilon = K_t \cdot \Delta\varepsilon_{nom} \qquad \text{Cyclic loading; } \sigma_m = 0 \qquad (2.45b)$$

Here, the notch strain rate $\Delta\varepsilon$ can be obtained directly if K_t and $\Delta\varepsilon_{nom}$ are known. If nonzero mean stress is present ($\sigma_m \neq 0$), the maximum notch strain ε_{max} should be obtained first from equation (2.43a). Furthermore, the corresponding maximum notch stress σ_{max} follows from the Ramberg-Osgood relationship (see equation 2.26), where the coefficients K' and n' should be considered instead of coefficients K and n. In the next step, the notch strain range, $\Delta\varepsilon$, and corresponding notch stress range, $\Delta\sigma$, are obtained using equations (2.45b) and (2.43), respectively. The subsequent procedure is the same as already presented by Neuber's rule.

Glinka's rule

This rule is based on the assumption that the strain energy density at the notch root is nearly the same for linear elastic (W_e) and elastic-plastic (W_p) notch behaviour, as long as the plastic zone at the notch is surrounded by elastic stresses and strains represented by σ_{nom} and ε_{nom} (see Figure 2.40).

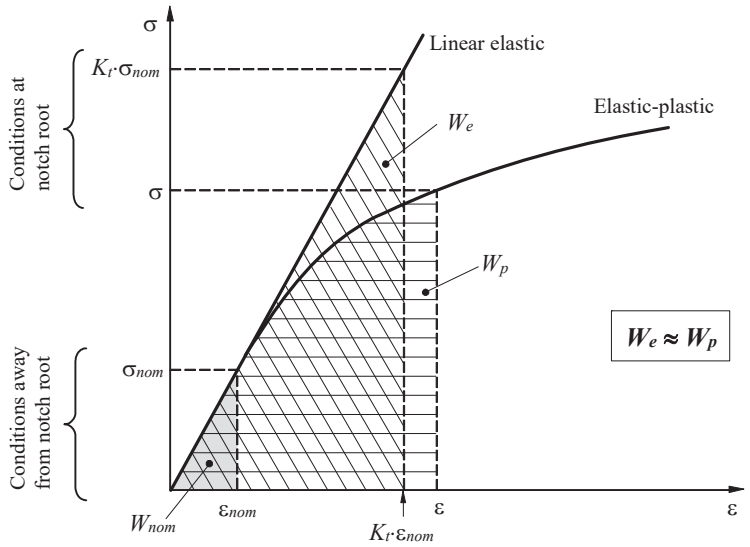

Figure 2.40: Schematic representation of Glinka's rule [2.38]

For nominal elastic stress, σ_{nom}, the nominal strain energy density, W_{nom}, is given by (with $\varepsilon_{nom} = \sigma_{nom}/E$):

$$W_{nom} = \frac{{\sigma_{nom}}^2}{2E} \tag{2.46}$$

As long as the stresses (σ) and strains (ε) at the notch root remain elastic, the linear elastic strain energy density, W_e, can be obtained as (with $\sigma = K_t \cdot \sigma_{nom}$; $\varepsilon = K_t \cdot \varepsilon_{nom}$):

$$W_e = \frac{(K_t \cdot \sigma_{nom})^2}{2E} \tag{2.47}$$

where K_t is the elastic stress concentration factor (see Section 2.1.4). For elastic-plastic behaviour at the notch root, the elastic-plastic strain energy density, W_p, is defined as:

$$W_p = \frac{\sigma^2}{2E} + \frac{\sigma}{n+1}\left(\frac{\sigma}{K}\right)^{\frac{1}{n}} \tag{2.48}$$

where E is the Young's modulus, K is the strength coefficient and n is the strain hardening exponent (see also Section 2.2.1). Considering $W_e = W_p$ it follows from equations (2.47) and (2.48):

$$\frac{\sigma^2}{E} + \frac{2\sigma}{n+1}\left(\frac{\sigma}{K}\right)^{\frac{1}{n}} = \frac{(K_t \cdot \sigma_{nom})^2}{E} \quad \text{Monotonic loading} \tag{2.49a}$$

$$\frac{\Delta\sigma^2}{E} + \frac{4\Delta\sigma}{n'+1}\left(\frac{\Delta\sigma}{2K'}\right)^{\frac{1}{n'}} = \frac{(K_t \cdot \Delta\sigma_{nom})^2}{E} \quad \text{Cyclic loading; } \sigma_m = 0 \tag{2.49b}$$

where K' is the cyclic strength coefficient and n' is the cyclic strain hardening exponent. If nonzero mean stress is present ($\sigma_m \neq 0$), the maximum notch stress, σ_{max}, is determined first from equation (2.47a). In the next step, the notch stress range $\Delta\sigma$ is obtained iteratively from equation (2.49b), and, finally, the notch strain range $\Delta\varepsilon$ is determined from equation (2.43). The subsequent procedure is the same as already presented by Neuber's rule.

2.2.5 Multiaxial loading

Analogous to the equivalent stress approaches presented in Section 2.1.5, equivalent strain approaches can be used to determine the fatigue life under multiaxial loading. Once an equivalent strain amplitude, ε_{aE}, is calculated from the appropriate strength hypothesis, the fatigue-life determination is the same as for the uniaxial loading. Similar to the equivalent stress approaches, equivalent strain approaches are also not suitable for non-proportional multiaxial loadings.

Maximum principal strain hypothesis (Rankine)

This hypothesis assumes that fatigue cracks will initiate in the plane perpendicular to the principal amplitude normal strain ε_{a1} (Figure 2.41*a*). Rankin's hypothesis gives a good result for hard and brittle materials (high strength steels, cast iron, etc.):

$$\varepsilon_{aE} = \varepsilon_{a1} \tag{2.50}$$

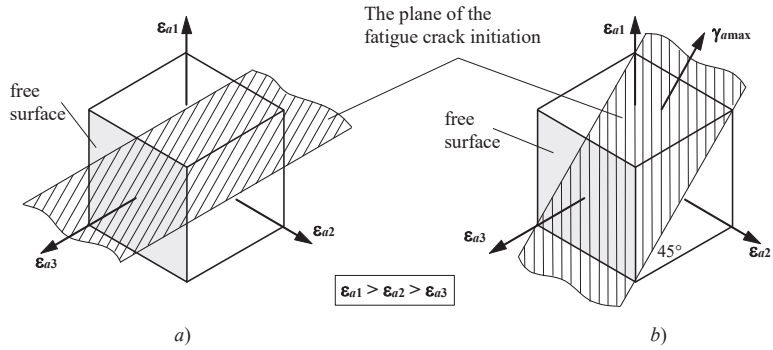

Figure 2.41: The plane of the fatigue crack initiation
a) Rankine's hypothesis, *b*) Tresca's hypothesis

If nonzero multiaxial mean stresses appear, the equivalent mean stress σ_{mE} should also be determined using equation (2.20). Once ε_{aE} and σ_{mE} are known, the fatigue life can be obtained using the appropriate mean stress criterion (Morrow, Manson, SWT) as described in Section 2.2.3.

Maximum shear strain hypothesis (Tresca)

This hypothesis assumes that fatigue cracks will initiate in the plane of maximum shear strain amplitude $\gamma_{a\max}$ (Figure 2.41*b*). Tresca's hypothesis gives a good result for tough and ductile materials (most of the structural steels, Al-alloys, etc.):

$$\varepsilon_{aE} = \frac{\gamma_{a\max}}{1+\nu} = \frac{\varepsilon_{a1} - \varepsilon_{a3}}{1+\nu} \tag{2.51}$$

where ν is the Poison's ratio of the material. If nonzero multiaxial mean stresses appear, the calculating procedure is the same as already described by Rankine's hypothesis.

Critical plane approaches

These approaches are based on the experimental observations which indicate that fatigue cracks nucleate and grow on specific planes, usually called "*critical planes*". Multiaxial fatigue approaches relating to critical planes can predict not only the fatigue life, but also the orientation of the crack or failure plane. Critical plane approaches can also be used for non-proportional loading conditions.

Critical plane approaches attempt to reflect the physical nature of fatigue damage in their formulation [2.39]. In general, fatigue cracks are irregularly shaped at the microscopic level, as the crack grows through the crystal grains. This results in interlocking and friction forces between crack surfaces during cyclic shear loading (i.e. crack closure), as shown in Figure 2.42*a*. Consequently, the crack tip driving force is reduced and the fatigue life is increased. If normal strain appears perpendicular to the crack plane (Figure 2.42*b*), it tends to separate crack surfaces, and, therefore, reduce interlocking and frictional forces. This increases the crack tip driving force, and, consequently, reduces the fatigue life.

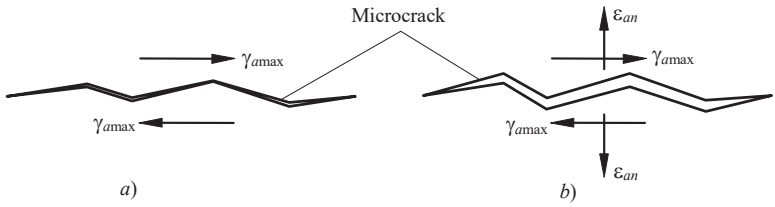

Figure 2.42: Physical modelling of a micro crack along a critical plane
a) Shear loading of crack, *b*) Shear and normal loading of crack

A common approach based on the physical interpretation of the fatigue damage of tough and ductile materials under multiaxial loading is the *Brown-Miller model* [2.40]. In this model it is assumed that fatigue cracks will initiate in the plane of maximum shear strain amplitude $\gamma_{a\max}$ (see Figure 2.41*b*). If additional normal strain amplitude ε_{an} appears perpendicular to the plane of $\gamma_{a\max}$ (see Figure 2.42*b*), the final Brown-Miller equation considering plane-stress conditions can be expressed as:

$$\gamma_{a\max} + \varepsilon_{an} = 1.65\frac{\sigma_f{}'}{E}(2N_i)^b + 1.75\varepsilon_f{}'(2N_i)^c\,; \qquad \sigma_m = 0 \quad (2.52)$$

where normal strain amplitude ε_{an} is obtained as:

$$\varepsilon_{an} = \frac{\varepsilon_{a1} + \varepsilon_{a3}}{2} \quad (2.53)$$

where ε_{a1} and ε_{a3} are principal normal strain amplitudes in planes 1 and 3, respectively. If nonzero mean stress appears ($\sigma_{m1} \neq 0$, $\sigma_{m2} \neq 0$), the normal mean stress σ_{mn} perpendicular to the plane of $\gamma_{a\max}$ should be obtained as:

$$\sigma_{mn} = \frac{\sigma_{m1} + \sigma_{m2}}{2} \quad (2.54)$$

where σ_{m1} and σ_{m2} are principal mean stresses in planes 1 and 2, respectively. The equation (2.52) is then modified as follows:

$$\gamma_{a\max} + \varepsilon_{an} = 1.65\frac{\left(\sigma_f{}' - \sigma_{mn}\right)}{E}(2N_i)^b + 1.75\varepsilon_f{}'(2N_i)^c \quad (2.55)$$

Another critical plane approach is the model presented by *Bannantine and Socie* [2.41]. The model assumes the fatigue crack initiation in the plane perpendicular to the maximum principal normal strain amplitude ε_{a1} (Figure 2.41*a*) and gives a good result for hard and brittle materials. Considering the maximum principal stress $\sigma_{\max 1} = \sigma_{m1} + \sigma_{a1}$, where σ_{m1} is the principal mean stress and σ_{a1} is the principal amplitude stress, the strain-life relationship is derived from the SWT equation (see Section 2.2.3):

$$\varepsilon_{a1} \cdot \sigma_{\max 1} = \frac{\left(\sigma_f{}'\right)^2}{E}(2N_i)^{2b} + \sigma_f{}'\varepsilon_f{}'(2N_i)^{b+c}\,; \quad \sigma_{\max 1} > 0 \quad (2.56)$$

2.2.6 Variable amplitude loading

The application of the strain-life approach under variable amplitude loading is similar to those in the stress-life approach (see Section 2.1.6). The principle of the complete procedure is shown schematically in Figure 2.43. The notched member (Figure 2.43*a*) is loaded with the loading spectrum as shown in Figure 2.43*b*. Using the appropriate cycle counting method (i.e. the "Rainflow" method), the loading spectrum can be replaced with four arranged loading cycles (A-D-A', B-C-B', E-H-E' and F-G-F'; Figure 2.43*c*). The belonging hysteresis loops in Figure 2.43*d* present the actual notch stresses and strains which can be obtained considering the notch-effect as described in Section 2.2.4. For each hysteresis loop, the appropriate values of σ_a, σ_m and ε_a should be obtained as shown in Figure 2.43*e*.

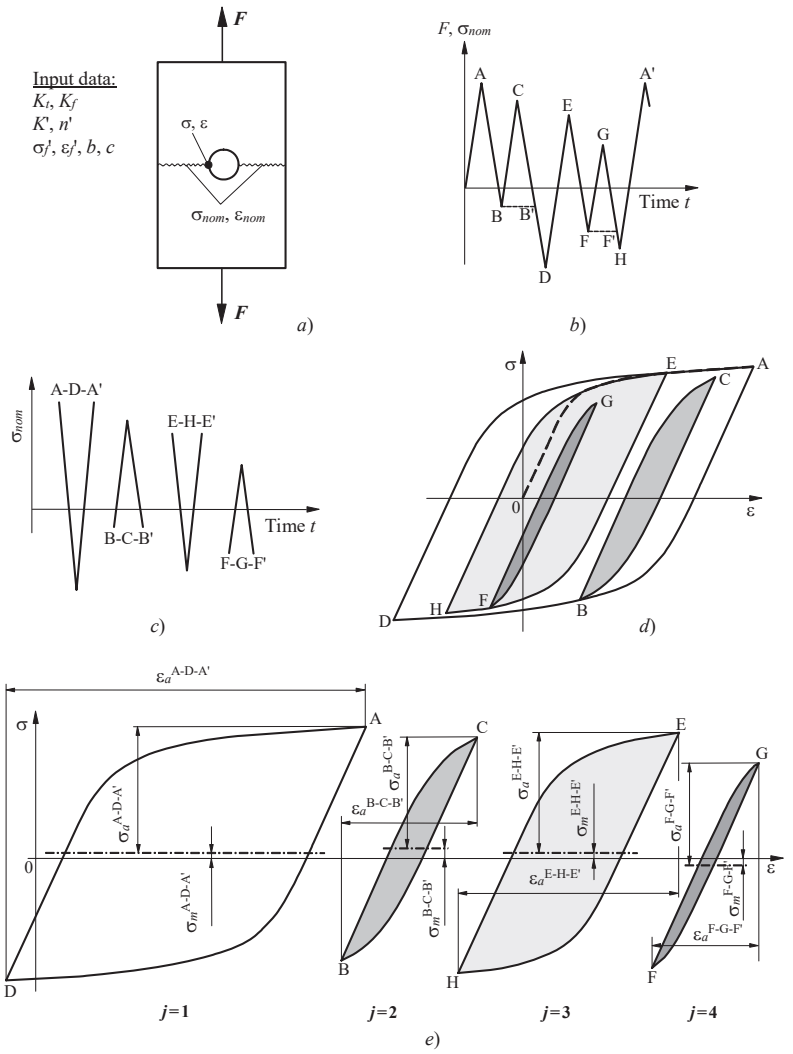

Figure 2.43: The principle of dimensioning under variable loading
a) Notched member, *b*) Loading spectrum, *c*) "Rainflow" method, *d*) Hysteresis loops in diagram σ – ε, *e*) The appropriate values of σ_a, σ_m and ε_a

If particular cycles are marked with j (j = 1 to 4 for the example in Figure 2.43), the number of loading cycles $(N_i)_j$ for crack initiation in a j-th cycle for given data pairs $(\varepsilon_a, \sigma_m)_j$ can then be obtained using the strain-life approach as described in Section 2.2.3. Following these procedures, the values $(N_i)_1$, $(N_i)_2$, $(N_i)_3$ and $(N_i)_4$ can be obtained for the example in Figure 2.43. Thereafter, it follows from the Palmgren-Miner rule that

$$\frac{n_1}{(N_i)_1} + \frac{n_2}{(N_i)_2} + \frac{n_3}{(N_i)_3} + \frac{n_4}{(N_i)_4} = \sum_{j=1}^{4} \frac{n_j}{(N_i)_j} \leq 1 \tag{2.57}$$

where n_j (j = 1 to 4) is the number of repetitions of the j-th cycle.

The procedure described above can also be used when dimensioning the multiaxial cyclic loaded components using the strain-life approach. In this case, the hypothesis presented in Section 2.5.5 should be considered.

2.2.7 Residual stresses

As presented in Section 2.1.7, the residual stresses may govern the fatigue behaviour significantly, especially in the HCF-area, where the stress-life approach is, in general, used to obtain the fatigue life of a cyclic loaded component. It was also pointed out that compressive residual stresses are beneficial (longer fatigue life) and tensile residual stresses are detrimental (shorter fatigue life). However, in the LCF-area, the influence of residual stresses is small because of their relaxation due to plastic deformation. For that reason, the residual stresses are usually neglected when dimensioning the cyclic loaded components using the strain-based approach.

2.2.8 Temperature

The low-cycle fatigue parameters (σ_f', b, ε_f', c) taken from the professional literature are generally related to the room temperature (ϑ = 20 °C). If another temperature appears (lower or higher), it should be considered when dimensioning using the strain-life approach.

Low-temperature

The low-temperature strain-life fatigue behaviour indicates that the fatigue resistance is unchanged in the HCF-area, while in the LCF-area the fatigue resistance may be decreased as a result of the lower ductility of the material.

High-temperature

Similar to the stress-life approach (see Section 2.1.8), some shortcomings exist when using the strain-life approach at high temperatures. This is a result of creep/fatigue/environment interaction.

2.3 Fatigue crack growth approach

The *Fatigue crack growth approach* requires the use of fracture mechanics and its integration into the fatigue crack growth theory to obtain the number of loading cycles required for crack propagation from the initial to the critical crack length, when final fracture of the treated component can be expected to occur. This approach can be applied to determine total fatigue life when it is used in conjunction with information on the existing initial crack, which has been, for example, detected by previous examination. The "two-stage approach" means that the fatigue crack growth approach is combined with the strain-life approach. In this case, total fatigue life can be determined from the number of stress cycles, N_i, required for fatigue crack initiation (previously determined using the strain-life approach), and the number of stress cycles, N_p, required for a crack to propagate from the initial to the critical crack length (subsequently determined using the fatigue crack growth approach); see also equation (2.1). In engineering design, the fatigue crack growth approach is usually used by dimensioning the machine parts and structures considering the *Fail-Safe Design* criterion.

The presence of a crack in an engineering component can reduce its fatigue life significantly. When a crack is detected in an analysed engineering component, the following questions are usually topical for designers:

- What is the residual strength of the analysed engineering component?
- What is the critical crack length that still assures the safe operation of the component?
- What is the operation time (number of loading cycles) needed for crack extension from the initial to the critical length?
- What is the fatigue life of a component with a detected micro-crack (i.e., as a consequence of mechanical or thermal treatment)?
- How frequent are periodic inspections of components with detected cracks?

As implied above, the effective use of fracture mechanics requires periodic inspections of cracked components in order to determine what sizes and

geometries of cracks are present or might be present. Such periodic inspections are often performed on aircraft, bridges, nuclear constructions, pressure vessels and many other engineering applications. According to this philosophy, a crack cannot grow to a dangerous length, and the critical part of the structure will be repaired before a critical situation could happen. Methods of inspection to detect the presence of possible cracks can be simple visual examinations, or more comprehensive examinations, such as X-ray photography or ultrasonics. Repairs necessitated by cracks may consider replacing a part or repairing it, for example, by machining away a small crack to leave a smooth surface [2.1–2.4].

This chapter provides the theoretical background for fracture mechanics and its use when solving engineering problems related to the fatigue of cyclically loaded machine parts and structural components. The topic is focused predominantly on the *K*-concept and its application to fatigue problems, although other concepts may be found in the literature (*G*-concept, *COD*-concept, *J*-concept, etc.)

2.3.1 Linear Elastic Fracture Mechanics

Linear Elastic Fracture Mechanics (*LEFM*) is used to determine crack growth in components under the basic assumption that material conditions are predominantly linear elastic during the fatigue process. This is usually the case in the High Cycle Fatigue (HCF) regime, or when using hard and brittle materials (i.e., high strength steels), where the actual stresses are lower if compared to the yield stress of the material.

The theoretical background of LEFM is based on three loading modes of cracked components as shown in Figure 2.44. *Mode I* (the opening mode) is the most common when solving uniaxial fatigue problems, and has received the greatest amount of investigation in the past. In this mode, tensile loading acts perpendicular to the crack front, and causes a crack opening in the plane of the maximum tensile stress. In *Mode II* (shearing mode), shear loading acts on the plane x-y along the crack front, and causes the sliding of crack faces relative to one another along the plane of the maximum shear stress. *Mode III* (tearing mode) also involves relative sliding of the crack faces, but now in plane y-z (perpendicular to the crack front).

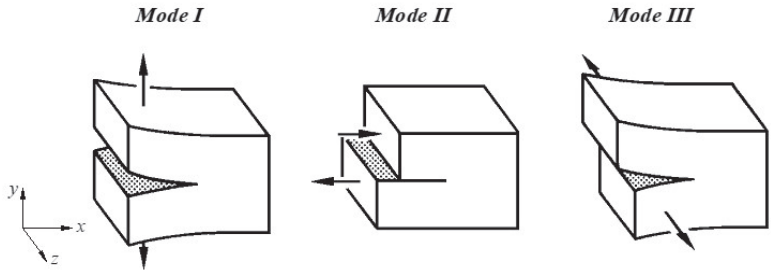

Figure 2.44: The basic loading modes of cracked components

Stress intensity factor

In general, the stress intensity factor K characterises the intensity of the stresses in the vicinity of an ideally sharp crack tip in a linear-elastic and isotropic material [2.4]. Figure 2.45 shows the elastic stress σ_y near the crack tip ($r/a << 1$) in an elastic isotropic body subjected to the pure Mode I loading [2.42]. It is evident that the magnitude of this stress at a given point is dependent entirely on K_I.

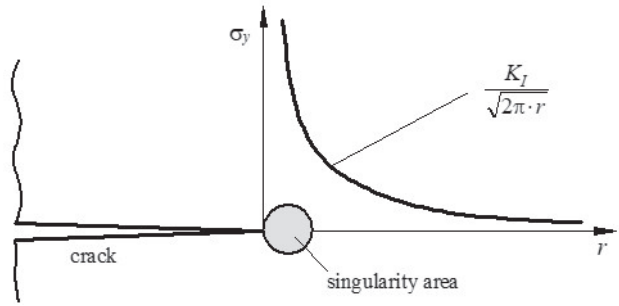

Figure 2.45: Elastic stresses near the crack tip for pure Mode I loading

It can be seen from Figure 2.45, that the elastic stress distribution σ_y approaches infinity ($\sigma_y \rightarrow \infty$) as r approaches zero ($r \rightarrow 0$). Following this finding, the stress intensity factor for mode I loading can be defined mathematically as:

$$K_I = \lim_{r \to 0} \sigma_y \cdot \sqrt{2\pi r} \tag{2.58}$$

Similar equations can also be expressed for Mode II and Mode III loading. Values of K are generally dependent on the external loading, crack length and geometry of the cracked member. Explicit equations for the determination of K can be found in the professional literature [2.43]. On the other hand, K can also be determined numerically using the available numerical approach (i.e., FEM). For mostly applied Mode I loading, the stress intensity factor is, in general, defined as:

$$K_I = \sigma_{nom} \sqrt{\pi \cdot a} \cdot \mathrm{f}\left(\frac{a}{W}\right) \tag{2.59}$$

where σ_{nom} is the nominal stress and acts at a large distance from the crack, a is the crack length and f(a/W) is the dimensionless function dependent on the crack length and geometry of the specimen [2.44, 2.45].

Critical stress intensity factor

It follows from equation (2.59) that the stress intensity factor increases with the increase of crack length and loading. The critical stress intensity factor K_c refers to the condition when a crack propagates in an unstable manner. According to the equation (2.59), K_c can be expressed mathematically as:

$$K_c = \sigma_c \sqrt{\pi \cdot a_c} \cdot f\left(\frac{a_c}{W}\right) \tag{2.60}$$

where σ_c is the applied nominal stress at crack instability and a_c is the crack length at instability. The critical stress intensity factor K_c is the main designing parameter when dimensioning cyclically loaded components using the fail-safe design criterion. Namely, it represents the critical value of the stress intensity factor K for a given load, as well as the crack length and geometry required to cause the fracture. In general, K_c depends mainly on the material and geometry (thickness) of the cracked member (see Figure 2.46). It is evident that the highest K_c corresponds to the thinnest specimen where the plane stress appears in the critical cross-section. As the thickness of the specimen increases the value of K_c decreases up to the thickness B_I when plane strain conditions appear. The minimum value of K_c is called *fracture toughness* K_{Ic} and refers strictly to the plane strain conditions. The type of fracture (brittle or ductile) is also dependent on the loading conditions (plane stress or plane strain) as can be seen in Figure 2.46.

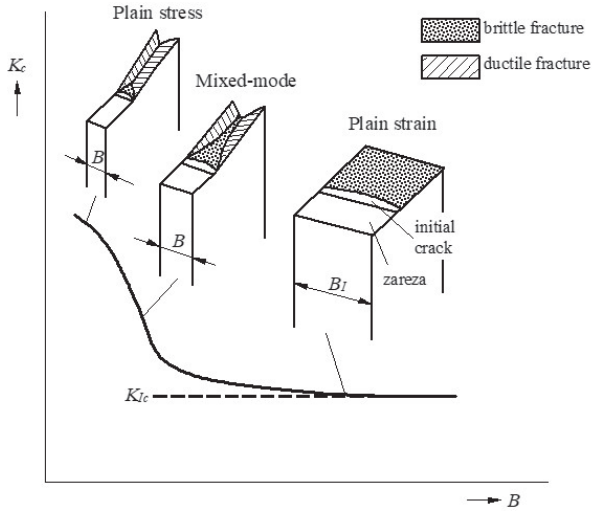

Figure 2.46: Critical stress intensity factor K_c

Fracture toughness K_{Ic} is a material parameter and is independent of the geometry of the cracked member. The values of K_{Ic} for different engineering materials can be found in the professional literature [2.46, 2.47]. It is clear from Figure 2.47 that K_{Ic}-values decrease with the increase of the yield stress of the material. Therefore, it can be concluded that high strength materials (i.e., high strength steels) are more sensitive to the occurrence of cracks if compared to low strength materials.

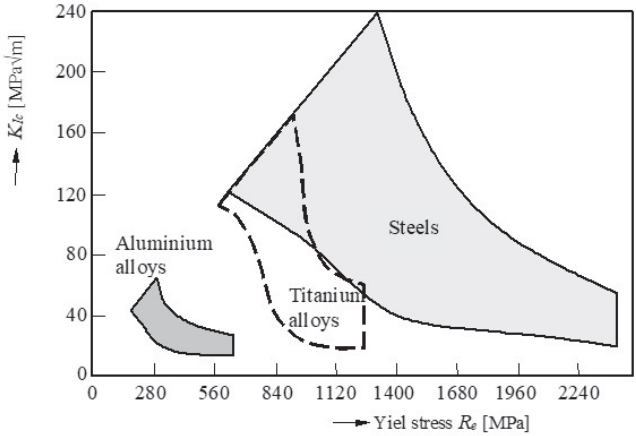

Figure 2.47: K_{Ic} -values of some typical engineering materials [2.2]

Plastic zone and its limitation on LEFM

As it is pointed out at the beginning of this Section, the use of LEFM is limited to the elastic behaviour of the material. However, the LEFM can also be used if the plastic zone size ahead of the crack is small in comparison to the other dimensions of the component. Figure 2.48 shows schematically the plastic zone in a tensile loaded cracked plate, where Irwin's formulation [2.48] is used to obtain the plastic zone size r_d ahead of the crack:

$$r_d = \frac{1}{\pi} \cdot \left(\frac{K_I}{R_e}\right)^2 \qquad \text{plane stress} \tag{2.61a}$$

$$r_d = \frac{1}{3\pi} \cdot \left(\frac{K_I}{R_e}\right)^2 \qquad \text{plane strain} \tag{2.61b}$$

where K_I is the stress intensity factor for Mode-I loading and R_e is the yield stress of the material.

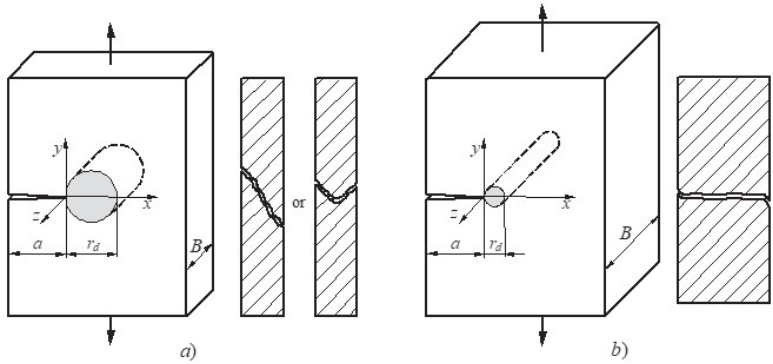

Figure 2.48: Irwin's formulation of the plastic zone and fracture mode *a*) Thin plate (plane stress), *b*) Thick plate (plane strain)

Irwin's plastic zone formulation as described above provides only a rough estimation of the plastic zone ahead of the crack, and actually represents the plastic zone in the plane of the crack. Plastic zone configuration in real engineering components is usually a combination of plane stress and plane strain conditions. In the case of a through-thickness crack (see Figure 2.49), the plane stress condition is dominant at the surface, while the plane strain occurs in the middle of the component.

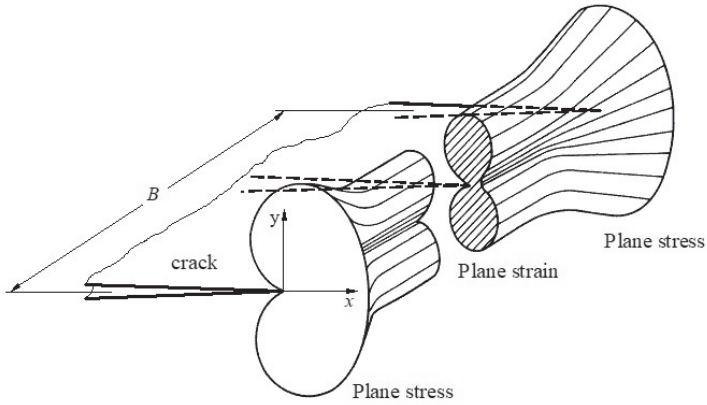

Figure 2.49: Plastic zone size at the tip of a through-thickness crack

If the plastic zone is sufficiently small, there will be an elastic region outside it where an elastic stress field occurs. The existence of such a region is necessary for the application of the LEFM theory. In that respect, it is necessary that the plastic zone is smaller in comparison to the distance from the crack tip to any boundary of the cracked member (see Figure 2.50):

- crack length a,
- uncracked ligament $(W - a)$,
- height of cracked member H.

Considering the explanation above, an overall limitation of LEFM may be expressed as:

$$a, (W - a), H \geq \frac{4}{\pi}\left(\frac{K_I}{R_e}\right)^2 \tag{2.62}$$

where K_I is the Mode-I stress intensity factor and R_e is the yield stress of the material.

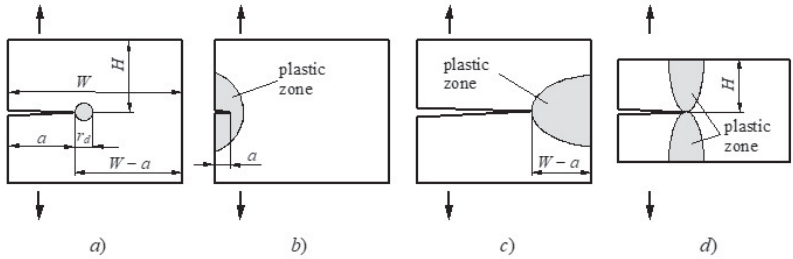

Figure 2.50: Different configurations of plastic zone in cracked members
a) Small plastic zone (the use of LEFM is valid), *b*) Crack length is too small, *c*) Ligament is too small, *d*) Height of member is too small

2.3.2 Fatigue crack growth

In Section 2.3.1, the theoretical background of LEFM is related to the monotonic loading. The following questions can be answered with the use of this knowledge: (i) What is the highest permissible loading of a cracked component and, (ii) What is the critical crack length that still assures the safe operation of the component? However, machine elements and structural components are often exposed to cyclic loading, which varies between a maximum (F_{max}) and a minimum (F_{min}) value. In such cases, the designer should first provide the answer to the following question: What is the operation time (number of loading cycles) needed for crack extension from the initial to the critical length, when final fracture can be expected to occur?

Figure 2.51 shows the curves *a*–*N* (crack length versus number of loading cycles) for three different nominal stress ranges, $\Delta\sigma_{nom}$. The fatigue crack growth rate, d*a*/d*N*, is defined as a slope of the *a* versus *N* curve at a given crack length or given number of cycles. Guidelines for the experimental determination of the crack growth rate, d*a*/d*N*, based on the data pairs (*a*, *N*), are described in the Standard procedure ASTM E647 [2.49].

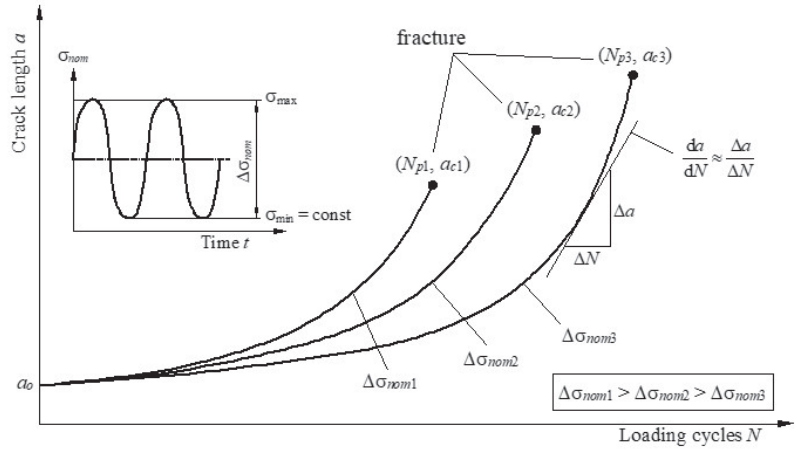

Figure 2.51: Fatigue crack length *a* versus the number of loading cycles *N*

When analysing cracked components using the fatigue crack growth approach, it is reasonable to combine the crack growth rate, d*a*/d*N*, with the *stress intensity factor range* ΔK. For Mode-I loading, it follows that:

$$\Delta K = \Delta K_I = K_{\max} - K_{\min} \tag{2.63}$$

where $K_{\max}$ and $K_{\min}$ are the maximum and minimum stress intensity factors, respectively. Considering the equation (2.59), it follows that:

$$K_{\max} = \sigma_{\max} \sqrt{\pi \cdot a} \cdot f\left(\frac{a}{W}\right) \tag{2.64a}$$

$$K_{\min} = \sigma_{\min} \sqrt{\pi \cdot a} \cdot f\left(\frac{a}{W}\right) \tag{2.64b}$$

where $\sigma_{\max}$ and $\sigma_{\min}$ are the maximum and minimum nominal stresses, respectively, and $f(a/W)$ is the dimensionless function dependent on the crack length and geometry of the specimen.

Similar to the stress-life approach and strain-life approach, the stress ratio *R* may be defined as:

$$R = \frac{K_{\min}}{K_{\max}} \tag{2.65}$$

For a given material and testing conditions, the crack growth behaviour is often described as the relationship between cyclic crack growth rate, da/dN, and the stress intensity factor range, ΔK. The crack growth tests are usually performed by pulsating loading (R = 0 or approximately zero) due to the fact that during compression loading the crack is closed, and, hence, no stress intensity factor, K, can exist. Figure 2.52 shows schematically the typical log(da/dN) – log(ΔK) plot with three major regions:

- region 1 (crack growth threshold),
- region 2 (stable crack growth),
- region 3 (instable crack growth).

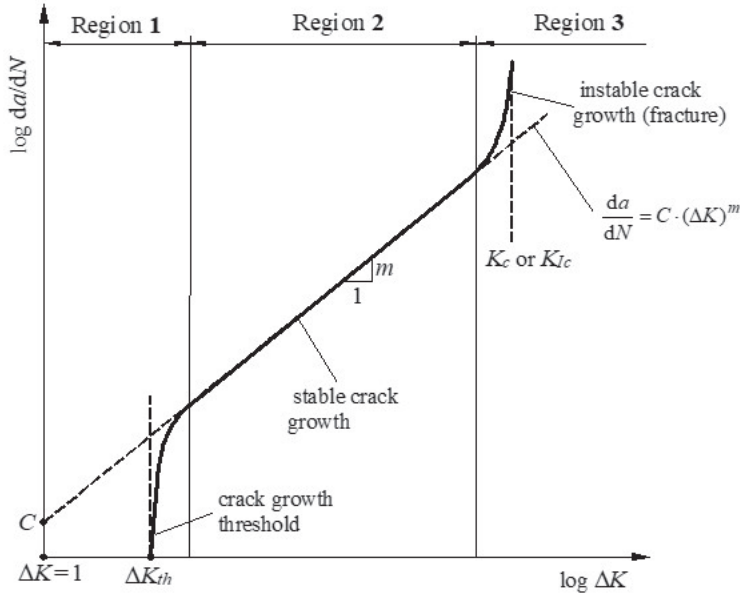

Figure 2.52: Schematic presentation of diagram log (da/dN) – log (ΔK)

Region 1

Region 1 indicates the threshold value, ΔK_{th}. Below ΔK_{th}-values (10^{-10} m/cycle according to the ASTM E647), fatigue cracks are characterised as non-propagating cracks. The main parameters influencing the value of ΔK_{th} are the microstructure of the material, mean stress (or R-value), loading frequency, environment, etc. For many engineering materials, the appropriate

values for ΔK_{th} can be found in the professional literature [2.2, 2.11]. For steels with an ultimate tensile strength $R_m \leq 1400$ MPa and stress ratio $R = 0$, the ΔK_{th} value can be determined approximately as [2.6]:

$$\Delta K_{th} \approx \frac{3.48 \cdot 10^3}{\sqrt{\sigma_D}} \tag{2.66}$$

where σ_D is the fatigue limit of the material obtained by $R = 0$.

Region 2

Region 2 shows a linear relationship between $\log(\mathrm{d}a/\mathrm{d}N)$ and $\log(\Delta K)$, which can be expressed mathematically with the *Paris equation* [2.50]:

$$\frac{\mathrm{d}a}{\mathrm{d}N} = C \cdot (\Delta K)^m \tag{2.67}$$

where C and m are material parameters which can be determined experimentally. Graphically (see Figure 2.52), m is the slope of the line and C is the coefficient found by extending the straight line to the value $\Delta K = 1$ MPa $\sqrt{\text{m}}$. Microstructure and mean stress have less influence on fatigue crack growth behaviour in Region 2 in comparison to Region 1. Once C and m are known and ΔK is obtained using an appropriate analytical procedure or numerical approach (FEM), the number of loading cycles N required for a crack to propagate from initial (a_0) to the critical (a_c) length can be determined with the integration of eq. (2.67):

$$N = \frac{1}{C} \int_{a_0}^{a_c} \frac{\mathrm{d}a}{(\Delta K)^m} \tag{2.68}$$

Region 3

In Region 3, the fatigue crack growth rates are very high as they approach instability (final fracture of the component). This region is controlled by the critical stress intensity factor K_c or fracture toughness K_{Ic}, which, in turn, depends on the microstructure, mean stress, and environment.

For a given material and environment, the fatigue crack growth behaviour as presented in Figure 2.52 is essentially very similar for different engineering components, because the stress intensity factor range, ΔK, is the principal controlling factor in the fatigue crack growth process. This

allows the fatigue crack growth rate da/dN versus ΔK data, obtained under constant amplitude conditions with simple specimen configurations, to be used in real design problems.

Effect of the stress ratio R

Material parameters to describe the fatigue crack growth (ΔK_{th}, C, m) taken from the literature are generally related to the stress ratio $R = 0$. If other values of R appear, they should be considered as shown in Figure 2.53. The presented curves indicate that increasing the R-value, which means increasing the mean stress, has a tendency to increase the crack growth rates. It is also clear that this influence is more significant in Regions 1 and 3.

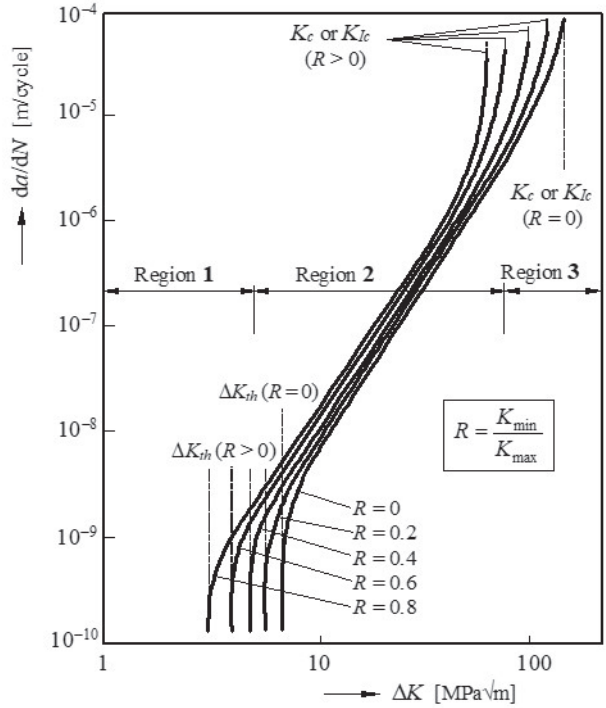

Figure 2.53: Diagram log (da/dN) – log (ΔK) for different R-values [2.2]

2.3.2 Fatigue crack growth by multiaxial fatigue

The fatigue crack growth theory presented in the previous sections is related to uniaxial fatigue considering the Mode-I crack propagation. However, engineering components are often subjected to multiaxial fatigue, where some combinations of loading modes I, II and III may appear at the same time. Such multiaxial loading results in *mixed-mode crack extension*, where both, crack growth direction and crack growth rate are important.

Maximum Tangential Stress criterion

The *Maximum Tangential Stress* (MTS) criterion was first proposed by Erdogan and Sih [2.51] and is generally suitable for mixed-mode I and II crack growth. This criterion is based on the elastic stress field around the crack tip, as shown in Figure 2.54. Assuming that the material is isotropic and homogeneous, the elastic stress field in polar coordinates can be described as follows:

$$\sigma_r = \frac{K_I}{\sqrt{2\pi r}}\left(\frac{5}{4}\cos\frac{\theta}{2} - \frac{1}{4}\cos\frac{3\theta}{2}\right) + \frac{K_{II}}{\sqrt{2\pi r}}\left(-\frac{5}{4}\sin\frac{\theta}{2} + \frac{1}{4}\sin\frac{3\theta}{2}\right) \qquad (2.69a)$$

$$\sigma_\theta = \frac{K_I}{\sqrt{2\pi r}}\left(\frac{3}{4}\cos\frac{\theta}{2} + \frac{1}{4}\cos\frac{3\theta}{2}\right) + \frac{K_{II}}{\sqrt{2\pi r}}\left(-\frac{3}{4}\sin\frac{\theta}{2} - \frac{3}{4}\sin\frac{3\theta}{2}\right) \qquad (2.69b)$$

$$\tau_{r\theta} = \frac{K_I}{\sqrt{2\pi r}}\left(\frac{1}{4}\sin\frac{\theta}{2} + \frac{1}{4}\sin\frac{3\theta}{2}\right) + \frac{K_{II}}{\sqrt{2\pi r}}\left(\frac{1}{4}\cos\frac{\theta}{2} + \frac{3}{4}\cos\frac{3\theta}{2}\right) \qquad (2.69c)$$

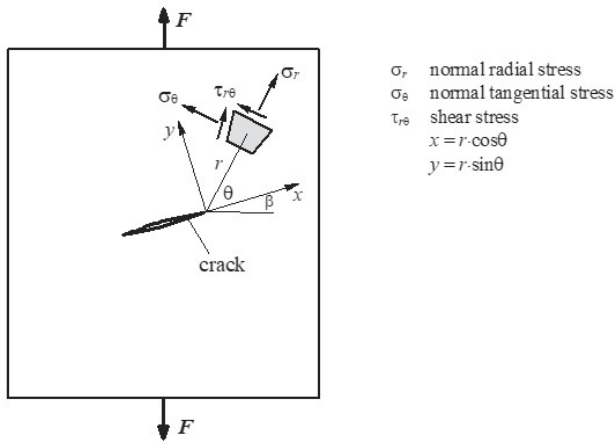

Figure 2.54: The elastic stress field around the crack tip for mixed-mode I and II

The MTS-criterion considers the following assumptions:

- The crack propagates under the angle $\theta = \theta_0$ where the normal tangential stress is maximum ($\sigma_\theta = \sigma_{\theta max}$); it means that the direction of the crack extension is perpendicular to the direction of $\sigma_{\theta max}$.
- Unstable crack growth (fracture) occurs at the moment when the maximum normal tangential stress $\sigma_{\theta max}$ reaches its critical value $\sigma_{\theta c}$, or when the equivalent stress intensity factor K_{EQ} reaches its critical value K_{EQc}.

As presented in [2.51], the values of θ_0 and K_{EQ} can be obtained as:

$$\theta_0 = \pm \arccos\left[\frac{3K_{II}^{\,2} + \sqrt{K_I^{\,4} + 8K_I^{\,2}K_{II}^{\,2}}}{K_I^{\,2} + 9K_{II}^{\,2}}\right] \tag{2.70}$$

$$K_{EQ} = \left[K_I \cos^2\frac{\theta_0}{2} - \frac{3}{2}K_{II}\sin\theta_0\right]\cos\frac{\theta_0}{2} \tag{2.71}$$

The crack propagation angle θ_0 can be positive or negative, which is dependent on the stress intensity factor K_{II}. Here, the following rule can be applied: $\theta_0 < 0$ if $K_{II} > 0$ and $\theta_0 > 0$ if $K_{II} < 0$, respectively. The value $\theta_0 = 0°$ corresponds to pure Mode I loading ($K_I \neq 0$, $K_{II} = 0$) while the values $\theta_0 = \pm 70.5°$ correspond to pure Mode II loading ($K_I = 0$, $K_{II} \neq 0$).

The equations (2.670) and (2.71) are actually related to the stress intensity factors K_I and K_{II} by monotonic loading. When studying multiaxial fatigue crack growth under cyclic loading, the stress intensity factor ranges $\Delta K_I = K_{I\max} - K_{I\min}$ and $\Delta K_{II} = K_{II\max} - K_{II\min}$ should be obtained first. The subsequent procedure is the same as that described above.

Energy release rate criterion

This criterion is based on the energy release rate G during crack extension. For pure Mode I loading, the following relation between G and K_I is known:

$$G = \frac{1}{E}K_I^{\,2} \qquad \text{plane stress} \tag{2.72a}$$

$$G = \frac{1-\nu^2}{E}K_I^{\,2} \qquad \text{plane strain} \tag{2.72b}$$

where E is the modulus of elasticity and ν is Poisson's ratio.

For mixed-mode I and II loading (see Figure 2.54), the relationship between the energy release rate G and the stress intensity factors K_I and K_{II} can be expressed with the following equations:

$$G = \frac{1}{E}\left({K_I}^2 + {K_{II}}^2\right) \qquad \text{plane stress} \qquad (2.73a)$$

$$G = \frac{1-\nu^2}{E}\left({K_I}^2 + {K_{II}}^2\right) \qquad \text{plane strain} \qquad (2.73b)$$

The equivalent stress intensity factor K_{EQ} is obtained on the assumption that the energy release rate for Mode I loading, G=f(K_{EQ}), has a similar effect on the crack growth as the energy release rate G=f(K_I, K_{II}) for combined Mode I and Mode II loading. Thus, with combining equations (2.72) and (2.73), it follows:

$$K_{EQ} = \frac{1}{E}\sqrt{{K_I}^2 + {K_{II}}^2} \qquad \text{plane stress} \qquad (2.74a)$$

$$K_{EQ} = \frac{1}{E}\sqrt{\left({K_I}^2 + {K_{II}}^2\right)(1-\nu^2)} \qquad \text{plane strain} \qquad (2.74b)$$

In the energy release rate criterion, the crack extension direction is obtained according to the *Virtual Crack Extension (VCE)* method, which was developed by Hellen [2.52]. As shown in Figure 2.55, different virtual crack extensions of length δr are assumed around the crack tip. For each virtual crack extension with the belonging angle θ, the equivalent stress intensity factor K_{EQ} = f(K_I, K_{II}) is calculated using equation (2.74). In the next step, the crack is actually extended under the angle θ_0, which corresponds to the maximum value of K_{EQ}. Similar to the MTS criterion, the ranges ΔK_I, ΔK_{II} and ΔK_{EQ} should be considered when analysing fatigue crack growth.

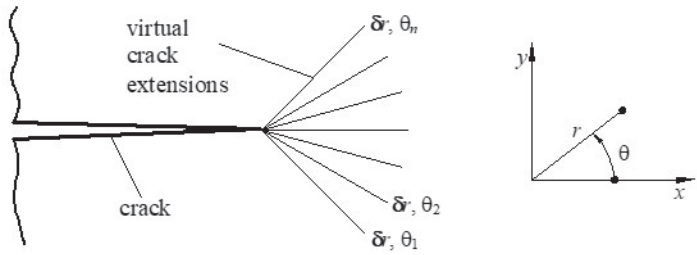

Figure 2.55: Virtual crack extensions in Polar coordinates

Minimum Strain Energy Density criterion

The minimum *Strain Energy Density* (SED) criterion was first proposed by Sih [2.53], and may be used for mixed-mode I and II crack growth (see Figure 2.54). Here, the strain energy density w is defined as:

$$w = \frac{1}{r}\left(a_{11}{K_I}^2 + 2a_{12}K_I K_{II} + a_{22}{K_{II}}^2\right) \tag{2.75}$$

where a_{ij} are the auxiliary coefficients

$$a_{11} = \frac{1+\nu}{8E}[(1+\cos\theta)(\kappa-\cos\theta)] \tag{2.76a}$$

$$a_{12} = \frac{1+\nu}{8E}\sin\theta\,[(2\cos\theta-\kappa+1)] \tag{2.76b}$$

$$a_{22} = \frac{1+\nu}{8E}[(\kappa+1)(1-\cos\theta)+(1+\cos\theta)(3\cos\theta-1)] \tag{2.76c}$$

where E is the modulus of elasticity and ν is the Poisson's ratio. The auxiliary parameter κ is defined as:

$$\kappa = \frac{3-\nu}{1+\nu} \qquad \text{plane stress} \tag{2.77a}$$

$$\kappa = 3-4\nu \qquad \text{plane strain} \tag{2.77b}$$

Considering the parameter $S = w{\cdot}r$, the crack will propagate under the angle $\theta = \theta_0$ which corresponds to the minimum Strain Energy Density ($w = w_{min}$; $S = S_{min}$). Furthermore, the unstable crack growth (fracture) occurs at the moment when the minimum coefficient of Strain Energy Density, S_{min}, reaches its critical value, S_c [2.53].

References

[2.1] Glodež S., Aberšek B., *The life of cracks: Theory and application*, Cambridge Scholars Publishing, 2020.
[2.2] Stephens R.I., Fatemi A., Stephens R.R., Fuchs H.O., *Metal Fatigue in Engineering*, John Wiley & Sons Inc, New York, 2001.
[2.3] Glodež S., Flašker J., *Dimensioning on the service life*, University of Maribor, Maribor, 2005.

[2.4] Dowling N.E., *Mechanical Behaviour of Materials*, Prentice Hall, New Jersey, 1999.
[2.5] Draper J., *Modern Metal Fatigue Analysis*, Emas Publishing, Warrington, 2007.
[2.6] Radaj D., Ermüdungsfestigkeit, Springer Verlag, Heidelberg, 2003. (in German)
[2.7] Suresh S., Fatigue of Materials, Cambridge University Press, Massachusetts Institute of Technology, 1998.
[2.8] Schijve J., Fatigue of Structures and Materials, Cambridge University Press, Springer Netherlands, 2009.
[2.9] ISO 1143:2010, Metallic materials–Rotating bar bending fatigue testing, ISO Standard, 2010.
[2.10] ASTM E2948, Standard Test Method for Conducting Rotating Bending Fatigue Tests of Solid Round Fine Wire, ASTM Standard,
[2.11] Zahavi E., *Fatigue Design*, CRC Press, Boca Raton, FL, 1996.
[2.12] Buch A., *Fatigue Strength Calculation*, Trans Tech Publications, 1988.
[2.13] Juvinall R.C., Marshek K.M., *Fundamentals of Machine Component Design*, John Wiley & Sons,New York, 2000.
[2.14] Shigley J.E., Mischke C.R., *Mechanical Engineering Design*, McGraw-Hill Book Co., New York, 1989.
[2.15] Glodež S., Šraml M., Kramberger J., A Computational Model for Determination of Service Life of Gears, *International Journal of Fatigue*, Vol. 24, 2002, 1013–1020.
[2.16] Ellwood D.G., *Mechanical Metallurgy*, McGraw-Hill, New York 1988.
[2.17] Rice RC., *SAE Fatigue Design Handbook*, 3rd ed., AE-22, SAE, Warrendale, PA, 1997.
[2.18] Heywood R.B., *Designing Against Fatigue*, Chapman & Hall, London, 1962.
[2.19] Pilkey W.D., Peterson's Stress Concentration Factors, John Wiley, New York, 1997.
[2.20] Kuhn P., Hardrath H.F., *An Engineering Model for Estimating Notch Size Effect in Fatigue*, NACA TN 2805, 1952.
[2.21] Socie D.F., Marquis G.B., *Multiaxial fatigue*, Society of Automotive Engineers, Warrendale, PA, 1999.
[2.22] Palgren A., *Durability of Ball Bearings*, ZDVDI, Vol. 68, 1924, p. 339.
[2.23] Miner M.A., Comulative Damage in Fatigue, *Trans. ASME, J. Appl. Mech.*, Vol. 67, 1945, p. 159.

[2.24] Matsuishi M, Endo T., Fatigue of Metals Subjected to Varying Stress, *Paper presented to the Japan Society of Mechanical Engineers, Fukuoka*, Japan, 1968.
[2.25] ASTM E-1049, *Cycle Counting for Fatigue Analysis*, Annual Book of ASTM Standards, Vol. 03.01., ASTM, West Conshohocken, PA, 1998.
[2.26] Stephens R.I, Chung J.H., Glinka G., Low Temperature Fatigue Behaviour of Steels - A Review, *SAE Technical Paper 790517*, 1979.
[2.27] Verkin B.I., Grinberg N.M., Seryuk V.A., Yakovenko L.F., Low temperature fatigue fracture of metals and alloys, *Materials Science and Engineering*, 58, 1983, 145–168.
[2.28] Forrest P.G., *Fatigue of metals*, Pergamon Press, London, 1962.
[2.29] ISO 6892-1:2019, Metallic materials, Tensile testing -Part 1: Method of test at room temperature, 2019.
[2.30] ASTM E606, Standard Practice for Strain-Controlled Fatigue Testing, ASTM International, West Conshohocken, PA, 2004.
[2.31] Tavernelli J.K., Coffin L.F., Experimental Support for Generalized Equation Predicting Low Cycle Fatigue, *Trans. ASME- J. Basic Eng.*, Vol. 84, 1962, p. 533.
[2.32] Manson S.S., Discussion of Reference [2.31], *Trans. ASME- J. Basic Eng.*, Vol. 84, 1962, p. 537.
[2.33] Morrow J.D., *Fatigue Properties of Metals*, Section 3.2 in Fatigue Design Handbook, Warrendale, SAE, 1968.
[2.34] Manson S.S., Effect of Mean Stress and Strain on Cyclic Life, *Machine Design*, 1960, pp. 129-135.
[2.35] Smith K.N., Watson P., Topper T.H., A Stress-Strain Function for the Fatigue of Metals, *J. Mater.*, Vol. 5, 1970, p. 767.
[2.36] Neuber H., Theory of Stress Concentrations for Shear-Strained Prismatical Bodies with Arbitrary Nonlinear Stress Strain Laws, *Trans. ASME, J. Appl. Mech*, Vol. 28, 1961, p. 544.
[2.37] Topper T.H., Wetzel R.M., Morrow J.D., Neuber's rule applied to fatigue of notched specimens, *J. Materials*, *JMSLA*, Vol. 4, 1969, p. 200.
[2.38] Molski K., Glinka G., A Method of Elastic-Plastic Stress and Strain Calculation at a Notch Root, *Mat. Sci. Eng.*, Vol. 50, 1981, p. 93.
[2.39] Fatemi A., Socie D.F., A critical plane approach to multiaxial fatigue damage including out-of-phase loading, *Fatigue Fract. Eng. Mater. Struct.*, Vol. 11, 1988, p. 149.

[2.40] Brown M.W, Miller K.J., A Theory of Fatigue under Multiaxial Strain Conditions, *Proc. Inst. Mech. Eng.*, Vol. 187, 1973, pp. 745-755.
[2.41] Bannantine J.A., Socie D.F., A Variable Amplitude Multiaxial Fatigue Life Prediction Method, *Proceedings of Third International Conference on Biaxial/Multiaxial Fatigue*, Stuttgart, 1989.
[2.42] Anderson T.L., *Fracture Mechanics*, CRC Press, Boca Raton, FL, 1995.
[2.43] Murakami Y., *Stress Intensity Factors Handbook*, Vol. 2, Perg. Press, Oxford, 1987.
[2.44] ASTM E399, Standard Test Method for Plane-Strain Fracture Toughness of Metallic Materials, Vol. 03.01, West Conshohocken, PA, 2000, p. 431.
[2.45] BS 7448, Fracture Mechanics Toughness Tests; Part 1: Method for Determination of K_{Ic}, critical *CTOD* and critical *J* values of metallic materials, British Standard, 1991.
[2.46] Damage Tolerant Design Handbook, *A Compilation of Fracture and Crack Growth Data for High Strength Alloys*, CINDAS/Purdue University, Lafeyette, 1994.
[2.47] Schwalbe K.H., Bruchmechanik metallischer Werkstoffe, Carl Hanser Verlag, 1980. (in German)
[2.48] Irwin G.R., Plastic zone near a crack and fracture toughness, *Proceedings of the Seventh Sagamore Ordnance Materials Conference*, Vol. 4, 1960, pp. 63-78.
[2.49] ASTM E647, Standard Test Method for Measurement of Fatigue Crack Growth Rates, Vol. 03.01, West Conshohocken, PA, 2000, pp. 591.
[2.50] Paris P.C., Gomez M.P., Anderson W.E., A Rational Analytical Theory of Fatigue, *Trend Eng.*, Vol. 13, 1961, pp. 9-14.
[2.51] Erdogan F., Sih G.C., On the Crack Extension in Plates under Plane Loading and Transverse Shear, *Int. Journal of Basic Engineering*, 1963, pp. 519-525.
[2.52] Hellen T.K., On the Method of Virtual Crack Extensions, *International Journal for Numerical Methods in Engineering*, Vol. 9, 1975, pp. 187-297.
[2.53] Sih G.C., Strain Energy density factor applied to mixed mode crack problems, *Int. Journal of Fracture*, Vol. 10, 1974, pp. 305-321.

CHAPTER 3

SOME ASPECTS OF THE IRON AND ALUMINIUM POWDER MORPHOLOGY AND ITS INFLUENCE ON THE P/M PRODUCTS

As already presented in Section 1.1, there are two basic magnitudes when manufacturing sintered parts: Metallic powder and tooling. Metallic powder can be of pure metal (iron, aluminium, etc.), or alloyed powder (steel, bronze, etc.). Here, the powder chemical composition and its morphology play an important role on the die-compacting process, which results in a "green part" of a further sintered product. On the other hand, sintered parts should be designed with consideration of some shape recommendations, aimed at making compacting feasible, as well as to minimise manufacturing costs. Some aspects on these features are explained in the continuation of this Chapter.

3.1 The influence of iron powder morphology on the compaction process in an automatic die

Iron- and steel-based Powder Metallurgy (P/M) products, such as steel gears, locking mechanisms, porous filters, bushes, as well as other machine parts and structural elements, are produced mainly with the so-called conventional sintering technology. A fine, iron-based powder mixture is first uniaxially-die compacted into the final shape of the product with a mechanical or hydraulic press, and then sintered in a protective atmosphere at approximately 1100 °C. However, some geometrical limitations exist during the product design, and later in the phase of tool manufacture when considering uniaxial die compaction. Namely, the compacting forces are not transferred uniformly over the height and cross-section of the green compact because of the internal friction among the powder particles and the friction on the die walls [3.1, 3.2]. Furthermore, the final result of the compacting process is also dependent on the ratio between the height (h) and the characteristic length L (i.e. diameter D for cylindrical parts), h/L, of the green compact. For these reasons, it is not possible to ensure a completely

uniform green density over the whole volume of the green compact. The non-uniform density distribution also appears in products with sharp crossings and chamfers due to non-uniform powder filling of the die. In such cases, cracking of the green compact may happen during ejection.

An example of a sintered product with unsuitable geometry regarding uniaxial-die compacting is the two-height small gear (Figure 3.1) produced with the compacting toll as shown in Figure 3.2. An additional difficulty in this case is a very small gear module (m = 0.5 mm), as well as large height and diameter differences.

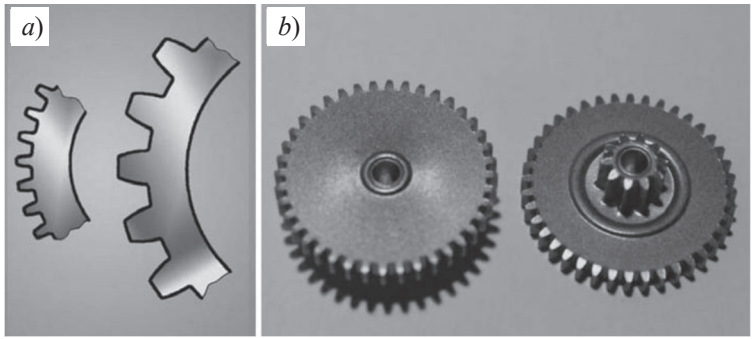

Figure 3.1: Sintered gear produced by the Unior factory [3.3]
a) Schematic presentation of small and large gear modules, *b*) Double spur gear

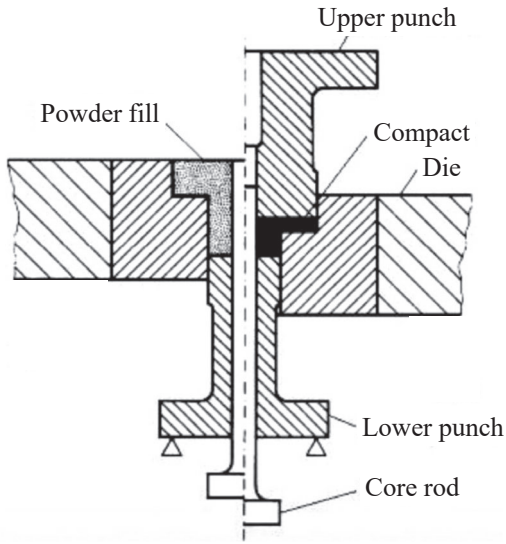

Figure 3.2: Schematic presentation of the tool to produce a double spur gear

A double spur gear with the number of teeth 40 and 10 is compacted with very high compacting pressure (over 700 MPa) in order to decrease the differences in the green density in the gear teeth because of poor filling of the engraving, as well as to decrease the differences in the green density between the gear parts with a large height difference to avoid cracking at the height crossing. The final result is a relatively short tool-life due to fatigue fracture of the most loaded tool parts (punches and core rod, Figure 3.2). Different solutions (better tool material, more precise tooling, optimisation of the die and press set up) have been researched to solve this problem. However, no one has been satisfied in regard to the appropriate strength characteristics of toll parts. Another possibility was a change of the existing powder granulometry. The hypothesis was that the selection of a finer powder could offer better compressibility and filling of the die. Unfortunately, as it follows, the change of the granulometry to a finer powder also did not give an improvement of the uniaxial-die compacting process but gave us a lot of useful and interesting information.

3.1.1 Experimental analysis

For the production of the investigated two-height gear a standard commercial Fe-based powder Distaloy AB, Höganäs (Sweden) was used (see Table 3.1). 5 kg of the original Distaloy AB powder was sieved on a set of vibrating sieves. The finest powder fraction (< 45 μm) was selected for the subsequent experiments and investigations [3.5].

Table 3.1: Nominal chemical composition of Distaloy AB [3.4]

Ni	Cu	Mo	Fe
1.75 %	1.50 %	0.50 %	The rest

The compressibility of the selected fine (< 45 μm) and rough (> 45 μm) mixtures was determined by instrumented apparatus [3.2] in standardised die dimensions of ϕ24 mm × 16 mm. The experiment for the compressibility determination was performed at a ram speed of 10 mm/min. It is a much slower speed than the actual speed in the industrial uniaxial-die compacting process. Therefore, the densification and deformation rate of the green compact in industrial conditions are different and higher (a larger number of structural defects affecting the sintering), respectively. The flowability and tap density of the selected powder mixtures were determined with a Hall flowmeter [3.1]. The prescribed amount of carbon (w = 0.5 %) and Kenolube lubricant (w = 0.9 %) were added to the original Distaloy AB fine sieved powder. Both fine and rough mixtures were then homogenised in a double-cone mixer. The experimental compaction of the analysed gears was performed on an industrial 60 kN mechanical press (Dorst, Germany). Approximately 100 gear pieces were compacted from both powder mixtures, followed by the sintering of green compacts in an industrial continuous-belt Mahler furnace under standard sintering conditions (1120 °C/30 min) in a protective atmosphere (N_2 + 5/10 % H_2). The sintered gears were additionally heat treated after sintering (oil quenching from 890 °C and tempering at 200 °C/30 min). The Vickers hardness HV5 of the sintered and heat-treated gears and the mechanical moment (teeth strength) were determined. The local bulk and micro-chemical compositions of the powders, green compacts and sintered gears were determined with an SEM/EDS (Jeol–JSM6500F/Oxford Inca Energy 450, Inca X-Sight LN2) and an XRF analyser (Thermo Scientific, Niton XL3t Goldd+).

3.1.2 Results and discussion

Figure 3.3 shows scanning electron micrographs of the fine and rough fractions of the investigated powders. The powders do not have large differences in morphology (shape and surface state), with the exception of the particle size. However, micro-chemical SEM/EDS analyses have shown that the local chemical composition of the fine fraction is significantly different compared to the original mixture. The most probable reason is the method of powder alloying as shown in Figure 3.4. The used Fe-based powder Distaloy AB is diffusion prealloyed (marked in Figure 3.4). In this case, the segregation of the alloying elements occurred during sieving, and, therefore, finer powder particles have a different chemical composition than the larger ones.

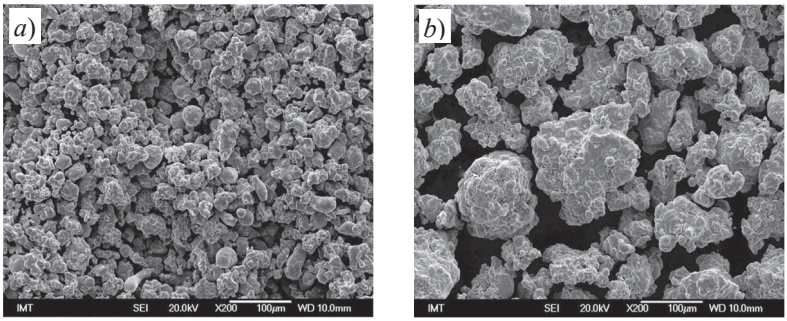

Figure 3.3: SEM micrograph [3.5]
a) Fine powder mixture (< 45 µm), *b*) Rough powder mixture (> 45 µm)

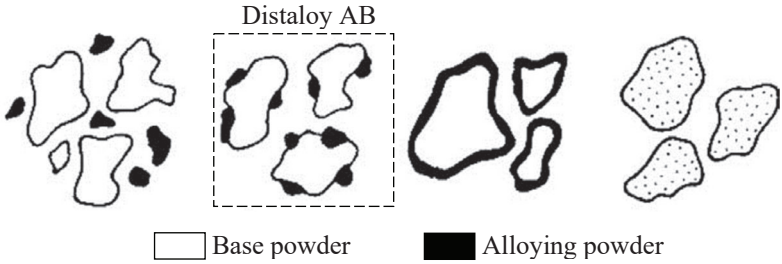

Figure 3.4: Standard ways of alloying techniques in PM [3.1]

Figure 3.5 shows EDS micro-chemical mapping analyses of the fine and rough powder particles. It is clear that their local compositions are quite different. This was also confirmed by the XRF analyses, which included a much larger volume of analysed samples. In spite of this, the local chemical compositions of all the samples differed significantly from the nominal chemical composition of the Distaloy AB powder (see Table 3.1). Table 3.2 shows the average chemical compositions of all the analysed samples. It is clear that the fine powder mixtures have a much higher content of alloying elements than the original (rough) powder mixture. As will be shown later, this over-alloying also has a significant influence on the mechanical properties of the sintered and heat-treated gears.

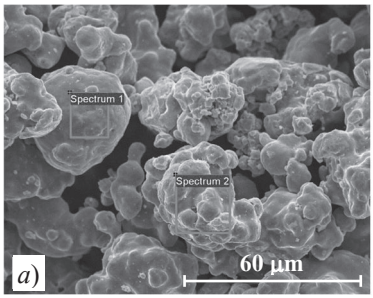

Mass fractions w [%]

	Ni	Cu	Mo	Fe
Spect. 1	4.01	1.71	1.74	92.54
Spect. 2	0.41	0.63	0.00	98.96

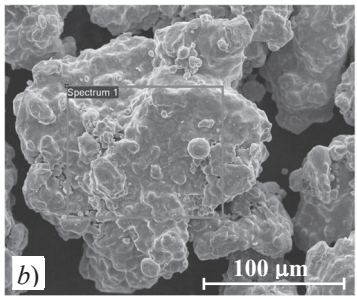

Mass fractions w [%]

	Ni	Cu	Mo	Fe
Spect. 1	0.81	0.71	0.97	97.51
Spect. 2	0.76	9.94	2.03	87.27

Remark: Spectrum 2 is not marked in the micrograph!

Figure 3.5: Mapping SEM/EDS microanalyses [3.5]
a) Fine powder mixture (< 45 µm), *b*) Rough powder mixture (> 45 µm)

Table 3.2: Average XRF bulk chemical compositions of the analysed samples [3.5]

Sample	Mass fractions w [%]						
	Fe	Ni	Cu	Mo	Mn	Cr	Si
Green compact, fine powder	83.03	9.73	5.91	0.78	0.09	0.04	0.12
Sintered gear, fine powder	88.92	5.47	4.42	0.80	0.20	0.05	0.08
Green compact, rough powder	90.57	4.72	3.53	0.60	0.10	0.06	0.17
Sintered gear, rough powder	93.65	3.10	2.11	0.65	0.13	0.06	0.12

Table 3.3 shows the obtained technological properties of the fine and rough powders. These values are also compared to the manufacturer's data proposed by Höganäs [3.4]. It can be seen that the fine powder has a poorer flowability, a lower tap density (ρ_n) and a negligibly better compressibility (ρ_z at p_m). It is the opposite to our hypothesis that the finer powder mixture has a better ability to fill the die cavity during the automatic compacting process. This was also confirmed by industrial experiments of the real gear compaction [3.5]. Besides this, the gears made of the fine powder mixture had poorer surface hardness after sintering and additional heat-treatment if compared to the gears made from rough powder (see Table 3.4).

Table 3.3: Technological properties of the analysed powder mixtures [3.5]

Powder type	Flowability [s/50 g]	Tap density ρ_n [g/cm^3]	Pressure		Green density ρ_z [g/cm^3]
			p_{max} [MPa]	p_m [MPa]	
Fine powder	30	2.75	722.6	595.4	7.15
Rough powder	26	2.99	738.5	512.4	6.94
Manufacturer's data (Höganäs)	26	3.06	7.10 g/cm^3 at 600 MPa		

Table 3.4: Vickers hardness HV5 of the analysed gears [3.5]

	Fine powder	Rough powder
Sintered gears	298	212
Tempered gears	293	318

Figure 3.6 shows a typical microstructure of a polished sample in the region of the tooth-root of the sintered gear visible under a Light Microscope (LM). It is clear that the sintered gear made of the finer powder mixture (Figure 3.6*a*) has well-distributed, fine pores, but it is much less densified if compared to the gear made of the original (rough) powder mixture (Figure 3.6*b*).

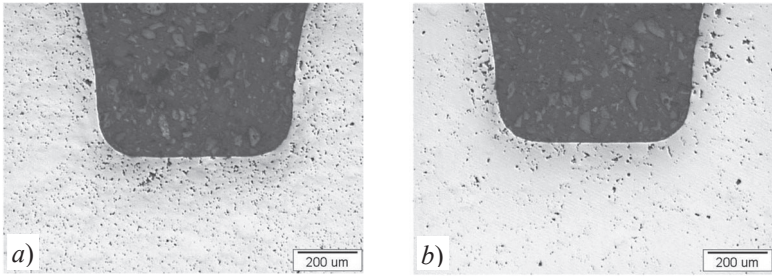

Figure 3.6: Microstructure of sintered gears [3.5]
a) Fine powder mixture, *b*) Rough powder mixture

Figure 3.7 shows the typical microstructures of polished and etched samples of the gears after sintering and additional heat treatment (tempering), visible under an LM. The gear made of the fine powder mixture (Figure 3.7*a*) has a microstructure in accordance with the inappropriate (over-alloyed) chemical composition. On the other hand, the gear made of the rough powder mixture (Figure 3.7*b*) has a typical and correct, but heterogeneous, martensitic/bainitic microstructure.

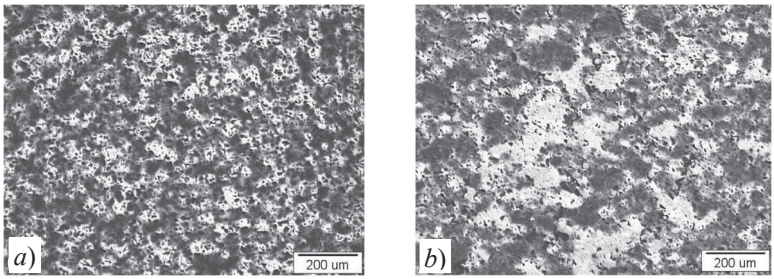

Figure 3.7: Microstructure of tempered sintered gears [3.5]
a) Fine powder mixture, *b*) Rough powder mixture

3.1.3 Conclusions

The metal powder mixture must have the appropriate engineering properties given by the chemistry and particle morphology, enabling a fast and reliable die-compaction process. The most important are a high tap density, a good powder flowability and a low compressibility. All this gives the green compacts an appropriate final shape with a smooth surface, a relatively high and uniform green density, as well as a green strength without internal flaws

and cracks. In the case of very small two-or-more-heights products, for example, spur gears with a low module, it is very difficult to obtain a uniform green density at acceptable compaction pressures. Often small cracks are formed at height crossings, and big differences in the green density appear in smaller or thinner regions.

The main objective of this study was to establish the possible influence of the selected prealloyed commercial iron powder's morphology and its technological properties on the automatic die compaction, as well as the sintering process in the case of a small two-level sintered gear with module m = 0.5 mm. The original (rough) iron powder was sieved, and the finest powder particle fraction (< 45 μm) was compared with the original powder mixture considering the automatic uniaxial-die compacting and sintering process. It was found that the selection of the finer powder mixture could not contribute to the improvement in the overall compacting process, as well as a better green compact. Namely, the fine powder fraction has a lower tap density, worse flowability and a negligibly better compressibility. It was expected that the selection of the fine powder fraction could contribute to an improvement in the automatic uniaxial-die compacting process of a small, two-height gear, especially to better filling of the teeth engraving, as well as a more uniform green-density distribution at a lower compaction pressure. This hypothesis has been disapproved, based on the experimental and semi-industrial work. It has been found that the selection of the finer powder mixture also has other traps. The sieved finer fraction has a different chemical composition than the original powder mixture. This has an important influence on the sintering and heat-treatment (tempering) response of the material. Therefore, the poorer mechanical properties were obtained of the gears made of the fine fraction. The open question is also the price of manufacture of the fine powder mixture with the correct chemical composition. For now, the existent automatic uniaxial-die compacting procedure for the selected small gears is indicated as optimal. In the future, it will be necessary to find other ways to improve the automatic uniaxial-die compacting procedure of small spur gears.

3.2 Morphological and microstructural features of Al-based alloyed powders for P/M applications

As presented in the previous Chapter, iron- and steel-based P/M products (gears, spurs, locking mechanisms, bearing bushes, etc.) are produced mainly with the automatic uniaxial-die compacting procedure. However, small complex sintered parts can also be used frequently in the furniture and

household industry, precision mechanics, articles for leisure, recreation and sports, etc. Besides advanced nano steels, polymers and ceramics, recently also light metals, i.e., Al, Mg and Ti based materials, have been recognised as future materials for different kinds of advanced applications [3.6, 3.7]. Here, Al and Al-alloys have an acceptable price, excellent corrosive resistance, and good mechanical and other physical properties (non-magnetic, excellent thermal and electrical conductivity, etc.). Therefore, they have the potential to produce Al-based sintered parts [3.8].

However, the P/M technology of Al and Al-alloys is very demanding, and has its own specifics compared to the sintering technology of iron and steel [3.9]. The Al-based powders for the P/M technology contain the alloying elements (Cu, Zn, Mg, etc.) with a high solid solubility in Al, enabling reaction and liquid-phase sintering, respectively. The high solid solubility of these elements is also important for the additional improvement of mechanical properties, enabling precipitation hardening during a heat treatment. Generally, Al-powders are surface oxidised because of the high affinity of Al to oxygen. Besides, these types of powders also contain approximately the mass fraction 1.5 % of polymeric lubricant (wax) that reduces the friction at die walls, while the powders are being automatically die compacted into the final compact shapes of the products. This lubricant has to be removed slowly during the first stage of sintering, in order to prevent deformations and cracking of the product. Therefore, its sintering is very complex. The optimum sintering conditions are commonly determined on the basis of Light Microscopy (LM) and Scanning Electron Microscopy (SEM), combined with a micro-chemical analysis based on the measurement of the dispersed kinetic energy of X-rays (Energy Dispersive X-ray Spectrometer, EDS). The investigation can also be completed very successfully with hot microscopy, as well as with Differential Scanning Calorimetry and Thermo Gravimetry (DSC/TG) [3.8].

A relatively large quantity of Al-based alloy powder is formed as a bypass product during the sand blasting of slugs and discs in the Talum factory [3.10]. Slugs (see Figure 3.8) are used as semi-products in the production of tubes and containers in the pharmaceutical, food and cosmetic industries. In this regard, there was a research interest to analyse and investigate its practical usability for the production of the advanced products made with the P/M technology [3.11]. The formed Al-based powder was compared with the commercially available Al-based powders that are generally used for conventional sintering technology.

Figure 3.8: Slugs produced in the Talum factory [3.10]

In the first part of this study we explain which types of Al-based powders are generally used for the production of sintered parts, what the required parameters are and why we considered them. Then, the results of the theoretical thermodynamic analyses and investigations of the morphological and microstructural characteristics of the selected commercial Al-based powders are presented, and their comparison with the Al-powder formed during the sand blasting are given, together with its potential for P/M applications. Henceforth, this Al-powder will be designated as the SB powder.

3.2.1 Chemical and thermodynamic characteristics of the Al-powders

In the frame of this study, three commercial Al-based powders (Alumix 123, 231 and 432), appropriate for the sintering technology, were purchased at Ecka Granules, Germany [3.12]. The powder producer has already provided some recommendations for the sintering of these alloy powders. However, in some cases these data are not enough to get all the necessary information for their comparison with the SB powder. Therefore, a complete theoretical thermodynamic analysis, as well as morphological and microstructural characterisations of the selected commercial powders, were performed first.

Table 3.5 shows the nominal and actual chemical compositions of the investigated powders. One can notice that the chemical compositions of these alloys are very simple. Wrought Al-alloys (extruded, forged) of similar types usually have more complex compositions with additional amounts of alloying elements (Cr, Ti, Zr, V, etc.) and, generally, lower amounts of impurities and oxygen. The chemical composition of the SB powder differs significantly from the commercial powders. It has much

higher amounts of Cu, Fe and Mn, but lower amounts of Mg and Zn. Only its Si content is comparable with the amount in the powder mixture Alumix 123, but it does not contain Zn. In view of the above, it is practically impossible to dilute the SB powder with additional corrections (by adding appropriate amounts of Al and other elements) in order to prepare a powder mixture similar to the one of the commercial powders given in Table 3.5.

Table 3.5: Nominal and actual average bulk chemical compositions of the investigated powders [3.13]

Powder mixture		Chemical composition; mass fraction *w* [%]					
		Cu	Si	Mg	Zn	Al	Other elements
Alumix 123	nominal	4.2 – 4.8	0.5 – 0.7	0.4 – 0.6	–	Bal.	–
	actual	4.5	0.62	0.48	–	n.d.*	0.08 Fe
Alumix 231	nominal	2.4 – 2.8	14 – 16	0.5 – 0.8	–	Bal.	–
	actual	2.7	15.0	0.58	–	n.d.*	–
Alumix 432	nominal	1.4 – 1.8	–	2.2 – 2.8	5.0 – 5.8	Bal.	–
	actual	1.6	–	2.4	5.8	n.d.*	0.29 Sn
SB powder	actual	7.74	0.83	0.1	1.57	87.0	0.08 Fe 0.48 Mn

n.d.* … not determined

In the first phase of the investigation, it is necessary to be acquainted at least with the experimentally determined binary-phase diagrams of Al with the basic alloying elements (Al-Cu, Al-Si, Al-Mg, Al-Zn), and with their mutual congruency (Si-Cu, Si-Mg, Mg-Cu, Mg-Zn). Such information gives us the appropriate data about the temperature solid-state solubility of an individual alloying element in Al, the basic temperature stability of the formed binary phases and the melting points. Certain ternary-phase diagrams with known multi-component intermetallic phases are also available in the professional databases [3.14, 3.15].

The thermodynamic behaviour of selected commercial powder mixtures (Alumix 123, 231 and 432) has been obtained using the *Thermo-Calc* software [3.16]. From the detailed thermodynamic analyses of the selected alloys (see ref. [3.13]) it was observed that, after the sintering (designated as T1a), all three alloys could be additionally heat treated with the conventional standardised precipitation strengthening (also age-hardening) procedure, i.e., solid-solution annealing combined with fast cooling (quenching) and natural (T4) or artificial ageing (T6, T76, etc.). In this case the temperature of solid-solution annealing must be below the formation temperature of the first liquid in the region of the maximum solid solubility

of the alloying elements in Al, typically 500 °C for 20 min. After homogenisation fast cooling must be performed, enabling the formation of a supersaturated solid solution of the αAl phase with the alloying elements. The final step of the heat treatment is natural (ambient conditions) or artificial (at an elevated temperature) ageing, typically 150 °C for 15 min.

Similar thermodynamic analysis as described above has also been done for the industrial SB powder (see Figure 3.9). For the optimum liquid-phase sintering conditions it would be recommendable that Al_6Mn and Alfa (Al-Fe-Mn-Si-Cu) are dissolved in the αAl solid solution. Unfortunately, in this alloying system a two-phase region (αAl + Liquid) does not exist, and the optimum sintering conditions cannot be assured.

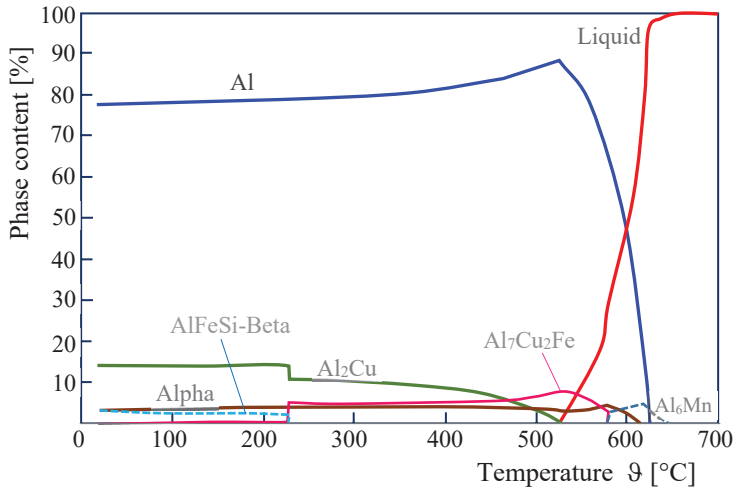

Figure 3.9: The thermodynamic behaviour of the SB-powder [3.13]

The theoretical thermodynamic analysis has shown that commercial Al powders have designed chemical compositions that enable reactive liquid-phase sintering. However, the industrial SB powder has a more complex chemical composition that is not accommodated for the optimum sintering process. By analogy with the determination of the sintering temperatures of the commercial Al powders (approximately 10 % to 20 % of the liquid phase present), the optimum sintering temperature of the SB powder is somewhere between 550 °C and 590 °C. But, in this temperature region, besides the liquid and αAl, there is still a relatively large amount of the intermetallic

phases of AlFeSi-Beta, Al_6Mn and Alpha. All these intermetallic phases are only dissolved in the liquid phase above 645 °C, but then the αAl phase also disappears completely, i.e, only the liquid phase is present and complete melting of the material occurs. On the other hand, it is necessary to know that the sinterability of a metal powder does not depend only on the chemical composition and thermodynamic conditions, but also on the other parameters (particle-surface oxidation, particle shape and size, homogeneity of the powder mixture, sintering atmosphere, etc.) which are out of the scope of this study.

3.2.2 Morphological characteristics of the Al-powders

For a successful industrial mass production of small complex parts, besides a good final densification of a powder compact with sintering, the preceding processing step, i.e., the automatic uniaxial cold or warm die compaction of the metal mould with automatic mechanical or hydraulic presses, is also important. The selected metal powder must flow fast and continuously from the powder container through the filling tube and the shoe into the die cavity, where it is fast compacted with as low as possible a pressure into a green compact with a high green density and strength, as well as without any internal or surface defects (cracks, flaws). The powder must fill all the parts of the die cavity completely. For this reason, besides a suitable chemistry, the metal powder must also have an appropriate particle morphology (the size distribution and shape). This is controlled mainly with the powder production process (atomisation, milling, powder heat treatment, etc.). Several standardised tests and investigations make it possible to evaluate the usability of the powder mixture for an automatic die compacting process and its technological properties [3.17]. The most important are the apparent and tap densities, the flowability and compressibility that are controlled with the particle morphology, as well as the chemical and metallurgical conditions of the powder's production. The apparent density and flowability of a powder are determined with a Hall flowmeter. Through a funnel of a standardised size 50 g or 100 g of powder flows for a defined period. The flow time is measured (for example, 30 s/50 g), and the value is designated as the powder flowability. At the same time, this powder is collected in a small copper pot with a known volume (25 cm^3), and the weight and apparent density of the loose powder is calculated in g/cm^3 (typically approximately 3 g/cm^3 for the Fe- and 1.2 g/cm^3 for the Al-based powders). The loose powder is generally densified, to some extent, with mechanical vibration. The tap density is a result of 100 mechanical vibrations of the loose powder. The compressibility of a powder is determined with a

standardised tool measuring the mechanical pressure needed for a certain green density of a compact (typically approximately 600 MPa for the green density of 7.0 g/cm^3 of a steel-powder compact, and 400 MPa for the green density of 2.6 g/cm^3 of an Al-powder compact, respectively [3.18]. It can be noticed clearly from Table 3.6 that the commercial powders have smaller parts of the fine fraction of powder particles, and better flowability and compressibility than the SB powder.

Table 3.6: The technological properties of the investigated powders [3.13]

Technological property		Powder mixture			
		Alumix 123[1)]	Alumix 231[1)]	Alumix 432[1)]	SB powder
Apparent density (g/cm^3)	nominal	1.05 – 1.15	1.05 – 1.25	1.10 – 1.25	n.d.[2)]
	actual	1.08	1.12	1.14	1.20
Tap density (g/cm^3)	nominal	1.20 – 1.50	1.20 – 1.50	1.20 – 1.50	n.d.[2)]
	actual	1.32	n.d.[2)]	n.d.[2)]	1.25
Flowability (seconds/50 g)	nominal	< 30	n.d.[2)]	< 30	n.d.[2)]
	actual	24	n.d.[2)]	n.d.[2)]	Not flowable
Green density (g/cm^3)	nominal	2.65 (400 MPa)	2.56 (620 MPa)	2.65 (400 MPa)	Not defined
	actual	2.68 (440 MPa)	2.52 (600 MPa)	2.61 (430 MPa)	2.37 (516 MPa)
Fine fraction < 45 μm, *w* [%]		max. 20	25 – 40	max. 35	45

[1)] Commercial Al-based powders [3.12].
[2)] Not determined.

Figure 3.10 shows the results of the complete sieving analyses of the investigated powders. The SB powder consists mainly of two fractions. The fine fraction (< 45 μm) is a result of the sand blasting of discs and slugs, i.e., small-scale particles (worn parts), while the coarse-particle fraction (160–200 μm) is a result of the incompletely worn sand-blasting media. On the other hand, the commercial Al-powders have a relatively uniform natural-particle-size distribution.

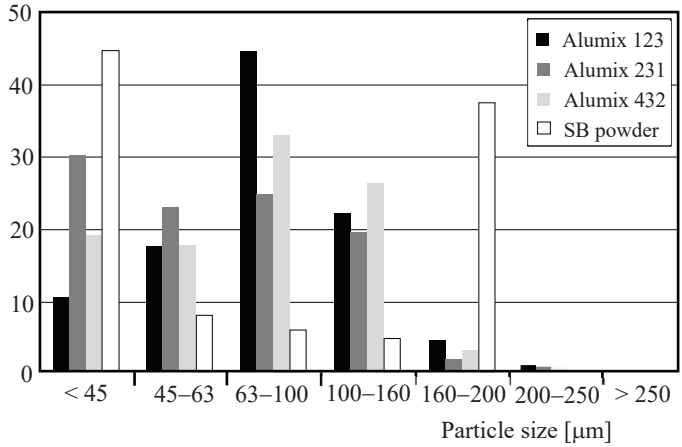

Figure 3.10: Particle size distribution histogram of the investigated powders [3.13]

3.2.3 Microstructural characteristics of the Al-powders

The revealed technological properties of the investigated powders are the results of their micromorphological and microchemical characteristics. The observations were performed in a loose condition (powder particles stacked on a special tape), as well as in cross-section (polished and etched metallographic samples). Figure 3.11 shows the SEM micrographs of loose powders Alumix 123 and Alumix 231 (Powder Alumix 432 has demonstrated a similar particle morphology).

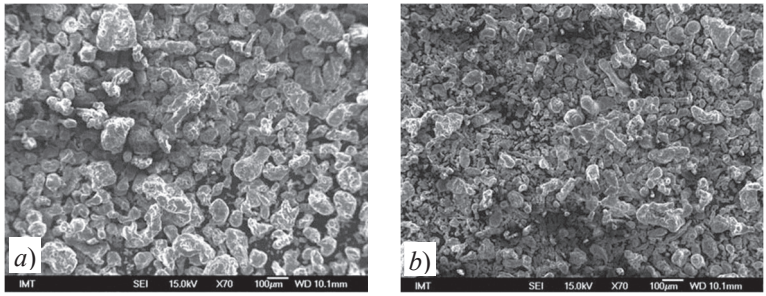

Figure 3.11: SEM micrograph of loose powder [3.13]
a) Alumix 123, *b*) Alumix 231

It can be seen from Figure 3.11 that the commercial powders have irregular particle shapes (rounded droplets) with smooth vitreous surfaces and different sizes from approximately 1 μm to 200 μm. This particle morphology is typical for gas (air) atomised Al powders.

Figure 3.12 shows the SEM/BEI (Backscatter Electron Image) cross-section micrographs of the commercial powders Alumix 231 and Alumix 432. In both powders it can clearly be seen that the particles are of different colours (shades of grey). This means that they have different chemical compositions. It was also noticed that small white irregular shapes (SiO_2, Al_2O_3 and CaO) were present in the powder Alumix 123, which was checked with the SEM/EDS microanalyses (Figure 3.13). The powder mixture contains the particles of pure Al, the Al-Si alloy and the Cu-Al alloy. Similar SEM/EDS results have been obtained for Alumix 231 and Alumix 432.

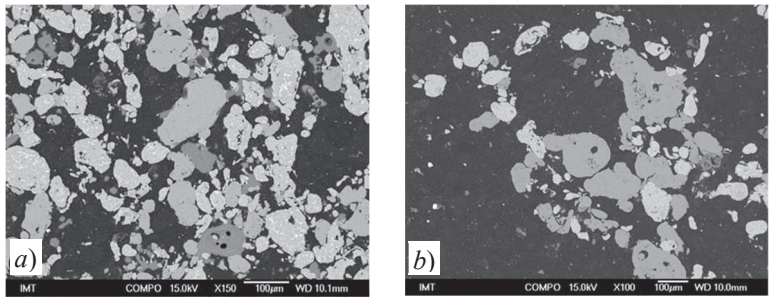

Figure 3.12: SEM/BEI cross-section micrographs of commercial powders Alumix 231 (*a*) and Alumix 432 (*b*) [3.13]

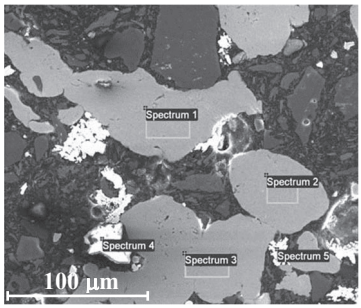

Mass fractions *w* [%]

	O	Al	Si	Ca	Cu
Spectrum 1		100			
Spectrum 2		89.3	10.7		
Spectrum 3		100			
Spectrum 4	55.7	2.3	41.0	1.0	
Spectrum 5		5.5			94.5

Figure 3.13: Mapping SEM/EDS microanalysis of Alumix 123 commercial powder [3.13]

Similar microstructural analyses, as presented in Figures 3.11 to 3.13 for commercial powders, have also been done for the industrial SB powder (see Figure 3.14). Here, the large round particles of the sand-blasting media and small irregular particles (scales or shells) formed due to the sand blasting of discs and slugs, are clearly visible (Figure 3.14*a*). Figure 3.14*b* shows the SEM/EDS analysis of a larger spherical particle (Spectrum 1) in the region where small-scale particles were also present (Spectrum 3). The large spherical particle is surface oxidised, and, besides Al, it also contains Si, Mn, Fe, Cu and Zn, which is in accordance with the chemical analysis of the sand-blasting media. However, the larger flat particle is practically pure Al (Spectrum 2) but also surface oxidised. The obtained particle morphology is probably the main reason for the low flowability and compressibility of the analysed industrial SB powder.

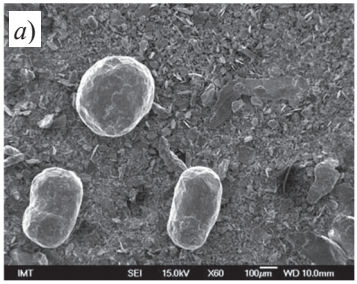

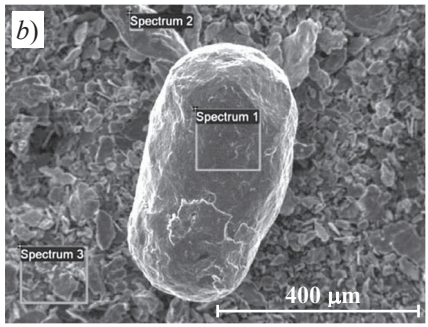

Mass fractions *w* [%]

	O	Al	Si	Mn	Fe	Cu	Zn
Spectrum 1	17.1	74.4	0.8	0.3	0.9	5.0	1.1
Spectrum 2	4.1	95.9					
Spectrum 3	15.2	76.3	0.7		1.0	5.6	1.2

Figure 3.14: SEM micrograph (*a*) and SEM/EDS analysis (*b*) of loose SB powder [3.13]

3.2.4 Compaction and sintering of the Al-powders

The investigated commercial powders were compacted into standard tensile-test specimens (35 pieces of each powder, Figure 3.15*a*) with a 60 MN Dorst mechanical press in the Unior factory [3.3]. The powders were dosed (poured) into the die cavity manually (Figure 3.15*b*). The Alumix 231 and Alumix 432 powders were compacted at approximately 440 MPa, while the Alumix 123 powder has a lower compressibility and was, therefore,

compacted at approximately 600 MPa. The corresponding average green densities are given in Table 3.6. The samples were then sintered in a batch lab furnace under the prescribed sintering conditions. The obtained average mechanical properties of sintered tensile specimens are given in Table 3.7.

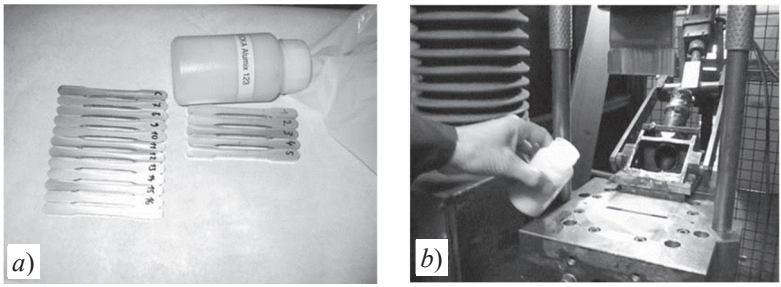

Figure 3.15: Standardised tensile test specimens (*a*) and manual pouring of the powder into a die cavity (*b*)

Table 3.7: Mechanical properties of sintered tensile-test specimens made of commercial Al-based powders [3.13]

	Sintered density ρ_s [g/cm^3]	Hardness HB	Young's modulus E [MPa]	Tensile strength R_m [MPa]	Yield stress R_e [MPa]	Elongation at fracture EL [%]
Alumix 123	2.60	65	3834	202	156	2.23
Alumix 231	2.62	104	4399	239	219	0.70
Alumix 432	2.73	102	4102	325	250	3.90

As a case study, the LM micrographs of the green and sintered compacts of Alumix 231 powder are given in Figure 3.16. It is clearly visible that the remaining porosity of the green compact after cold compaction is still relatively large. However, after the sintering, a good densification was obtained and only a small amount of residual porosity remained. One can also notice that the compacted powder mixture consists mainly of two types of particles (pure Al and alloyed particles of Al-Si-Mg-Cu), which was also confirmed with SEM/EDS analyses. This chemical inhomogeneity with the traces of a different initial-particle composition also remained after the sintering. The SB powder was also compressed and sintered experimentally. However, many flaws were formed at high compaction pressures because of its low compressibility, and, consequently, low green density (only 2.37 g/cm^3 at 516 MPa; see Table 3.6). The sinterability of the SB powder was

also low; therefore, a low sintering density was obtained, together with a high porosity and a significant amount of different defects (Figure 3.17).

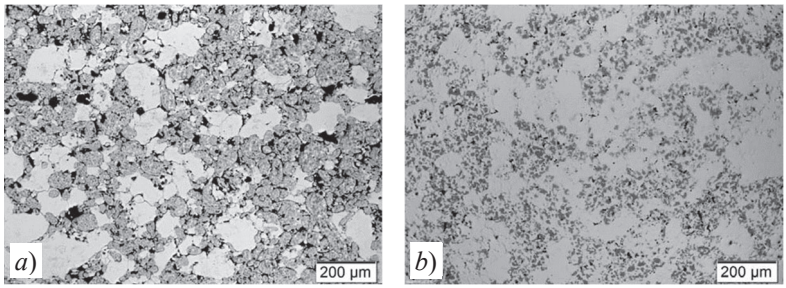

Figure 3.16: Microstructure of the commercial powder Alumix 231 [3.13]
a) After cold compaction, *b*) After sintering

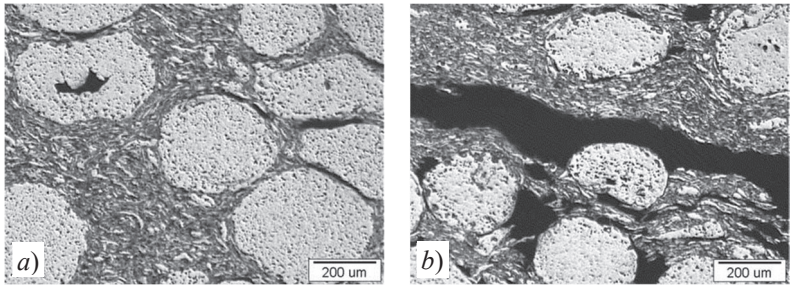

Figure 3.17: Microstructure of the SB powder after sintering with a clearly visible, irregular particle morphology and local defects [3.13]
a) Pores, lunkers, *b*) Flaws

Based on the obtained experimental results it may be concluded that SB powder is a relatively good raw material with approximately 86 % to 87 % of Al. However, it also contains a significant amount of oxides. Therefore, it seems that SB powder is more usable for the production of Al/Al_2O_3 composites using the modified Oxygen Dispersion Strengthening (ODS) technology than for conventional sintering technology. This technology was originally developed for the use of the Al scrap containing a lot of metallic oxides [3.13]. The appropriate powder mixture for the initial sintering (sintered aluminium powder, SAP) was obtained by grinding and milling the scrap, and the end result was a semi-final or final extruded or forged composite with the oxide-particle size of 10 μm to 100 μm. However, later, a lot of modifications and improvements of the technology were introduced,

using atomised powders and high-energy reaction ball milling (Figure 3.18). In this way various Al-based composites with a fine micro/nano dispersion of complex oxides, nitrides and borides can be formed, such as Al/Me_xO_y (for example Al_2O_3), Al/ M_xC_y (for example Al_4C_3, SiC), Al/M_xN_y (for example BN, TiN, ZrN, TiB_2, etc.) or their combinations. Nowadays, high-quality Fe- and Ni-based ODS superalloys with a fine dispersion of thermally stable oxides or intermetallics can also be produced.

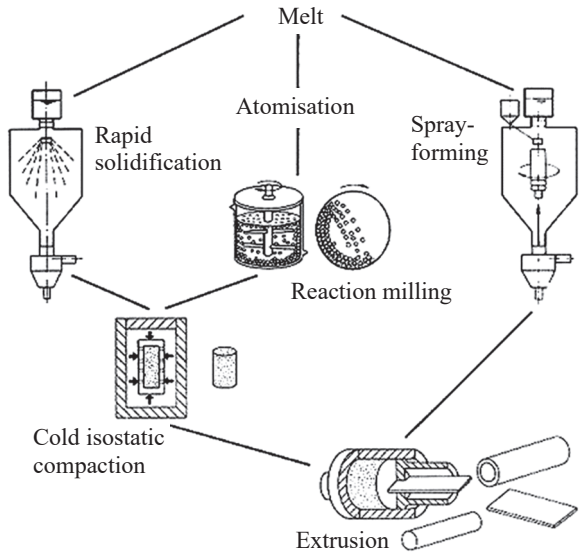

Figure 3.18: P/M technologies for the production of high-strength ODS Al-based alloys

3.2.5 Conclusions

In the frame of this study, the practical usability was analysed of the Al powder formed as a bypass product of the sand blasting of slugs and discs. The so-called SB powder was compared with commercially available Al-based powders used for conventional sintering technology. The theoretical thermodynamic analyses, as well as morphological and microstructural investigations, have shown that the SB powder has an inappropriate chemical and particle morphologies for conventional sintering technology. It would have to have more suitable morphological properties in order to be appropriate for use in conventional automatic die compacting and the

subsequent sintering process. Firstly, the flowability and compressibility of the powder have to be improved significantly. This could be achieved by adding an appropriate amount (approximately 50 % to 60 %) of soft, commercially available, pure Al powder (> 99.8 % of Al) with a suitable particle shape and size distribution. An additional procedure should be removal of the remaining coarse particles of the sand-blasting media with 180 μm or 250 μm sieves. The sand-blasting media contain relatively large amounts of Fe, Mn and Zn, and sieving would probably decrease the amounts of these elements significantly in the SB powder. However, the correct chemical composition similar to that of the standardised Al-Cu-Si-Mg alloy (for example, type 2xxx) would still not be attained, and additional corrections of the chemical composition would be necessary. In spite of this, the final target composition will be very difficult to obtain completely. Therefore, it seems that SB powder can be more suitable for the production of Al/Al_2O_3 composites using the modified Oxygen Dispersion Strengthening (ODS) technology than for conventional sintering technology. However, this still has to be confirmed in the frame of a new, additional experimental research.

References

[3.1] German R.M., *Powder Metallurgy Science*, Metal Powder Industries Federation (MPIF), Princeton, New Jersey, 1994.

[3.2] Šuštaršič B., Kosec L., Span T., Jelenko M., Torkar M., An instrumented cell to analyse the behaviour of metal powders during cold uniaxial die compaction, *Materials and Technologies*, Vol. 35, 2001, 351–360.

[3.3] Unior (Forge) https://www.unior-forge.com/en/forge/forge/products

[3.4] Höganäs, Distaloy AB, https://www.hoganas.com/en/powder-technologies/products/distaloy/distaloy-ab/

[3.5] Šuštaršič B., Godec M., Donik Č., Paulin I., Glodež S., Šori M., Ratej M., Javornik N., The influence of the morphology of iron powder particles on their compaction in an automatic die, *Materials and Technologies*, Vol. 49, 2015, 303–309.

[3.6] Gandara M.J.F., Aluminium, the metal of choice, *Materials and Technologies*, Vol. 47, 2013, 261–265.

[3.7] Lichy P., Cagala M., Beno J., Investigation of the thermomechanical properties and microstructure of special magnesium alloys, *Materials and Technologies*, Vol. 47, 2013, 503–506.

[3.8] Šuštaršič B., Medved J., Glodež S., Šori M., Korošec A., DSC/TG of Al-based Alloyed Powders for P/M Applications, Presentation at

21st International conference on Materials and Technology, Portorož, Slovenia, 13–15-th November, 2013.
[3.9] Powder Metallurgy of Al and Al alloys, P/M technologies and applications, Vol. 7, ASM Handbooks.
[3.10] Talum, Factory of Aluminium, Kidričevo, Slovenia, http://www.talum.si
[3.11] L2-4283 (B), Development of the model of the system for intelligent support of the selection of suitable powder material when developing sintered products, ARRS research project, 2011-2014.
[3.12] ECKA Granules, http://www.ecka-granules.com
[3.13] Šuštaršič B., Paulin I., Godec M., Glodež S., Šori M., Flašker J., Korošec A., Kores S., Abramovič G., Morphological and microstructural features of Al-based alloyed powders for powder-metallurgy applications, *Materials and Technologies*, Vol. 48, 2014, 125–136.
[3.14] Brandes E.A., Brook G.B., *Smithells Metals Reference Book,* Butterworth Heinemann, Oxford, UK, 1992.
[3.15] Villars P. et al, *ASM Alloy Phase Diagram Database*, ASM International, Materials Park, OH, USA, 2006–2013.
[3.16] *Thermo-Calc*, Software package for thermodynamic calculations, http://www.thermocalc.com
[3.17] *Metal Powder Industries Federation (MPIF)*, http://www.mpif.org/
[3.18] Powder Metallurgy, Materials Processes and Applications, EPMA Education Working Group, 2001.

CHAPTER 4

FATIGUE AND FRACTURE BEHAVIOUR OF DIFFUSION ALLOYED CU-NI-MO SINTERED STEEL

4.1 Introduction

Diffusion-alloyed powder Cu-Ni-Mo steels have been used widely in the PM industry for many decades. The contained elements Cu, Ni and Mo provide high mechanical strength without detrimental effects on compressibility and processability, since they have a low affinity with oxygen [4.1]. Mo is normally pre-alloyed, while Ni and Cu are added as elemental particulates to the steel and often diffusion bonded, providing unique heterogeneous microstructures mainly through the presence of Ni-rich areas.

As presented by Bergmark et al [4.2], copper is the most common alloying element in PM-steel. Copper is added as a powder and mixed with the base powder, lubricant and graphite. The influence of copper on the mechanical performance of PM-structural parts is strong. Namely, it increases strength through liquid phase formation during sintering. During the production of PM steels in industrial conditions (sintering temperature 1,120 °C), copper is in a liquid phase, and it accelerates and makes more uniform alloying of sintered Mn steels [4.3, 4.4]. Nickel has been shown to increase the ductility of PM steels. At the sintering temperature (1,120 °C), a heterogeneous microstructure is formed around the Nickel particles with austenite in the core. The austenitic islands are surrounded by martensite when graphite in the range 0.5 to 0.8% is also added to the premix. The combination of Mo pre-alloyed base powder mixed with Ni and Cu has been shown to create a material with high fatigue performance. A martensitic network around the base powder cores characterises the microstructure.

New applications of PM steel are found mostly in competition with wrought steels. Here, Nickel is one way to combine improvement of ductility and fatigue performance, taking into account an appropriate combination with Copper and Molybdenum [4.5, 4.6].

The powder mixture used in this study was Höganäs Distaloy AB (SINT – D30 according to the German Standard DIN 30910-4 [4.7]) with the addition of 0,58 wt% of lubricant Kenolube P11 and 0,3 wt% of Carbon in the form of Graphite UF4. Classical PM technology was used to prepare the test specimens. The metal powder (iron) was mixed with the alloying elements and lubricant. Besides improving the material properties, the alloying elements also control the dimensional changes during sintering and final density of the sintered component [4.8, 4.9]. Flat specimens (Fig. 4.1) were cold compacted with a pressure of 485 MPa, and then sintered for 30 minutes in a 10/90 hydrogen and nitrogen atmosphere at 1,120 °C. After sintering, half of the specimens were subjected to additional hardening (austenitisation at 915 °C, oil-quenched and tempered for 1 h at 175 °C). Both sets of specimens had a final density of 7,07 g/cm3.

Additional grinding of the specimens was done before experimental testing to remove the sharp edges. However, the surface of the specimens was not polished additionally (the average surface roughness of multiple measurements was $Ra = 0.76$ µm). The surface hardness was measured on three randomly chosen specimens from both as-sintered and as-hardened sets. The results of these measurements were in the range 160 to 180 HV1 for the as-sintered specimens and 310 to 340 HV1 for the as-hardened specimens. The term “as-hardened” denotes samples which were sintered, austenitised, oil-quenched and tempered.

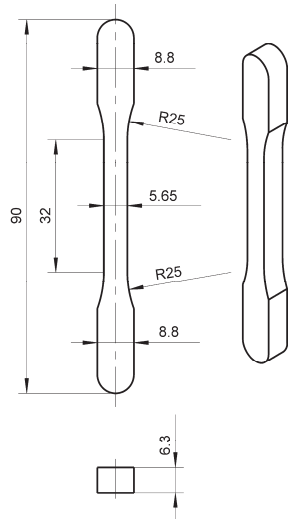

Figure 4.1: Flat specimen

Specimens for metallography were prepared using conventional grinding and polishing and etched in a natal solution (2 % nitric acid in alcohol). They were examined by the light microscope (Nikon 300) and two scanning electron microscopes (Quanta 200 and Sirion 400 NC, FEI). Figure 4.2 shows the initial microstructures of the as-sintered and as-hardened samples. In both conditions, the microstructure was not uniform, which originated mainly from the inhomogeneous distribution of the alloying elements. Nabeel et al. [4.10] already studied the effects of alloying elements on Ni-distribution in Fe-Ni alloys, which was relatively uneven. Combined additions of C, Cu and Mo, which were present in this PM steel, improved the post-sintering homogeneity of the Ni. Nevertheless, the as-sintered samples contained large Ferrite (F) and Austenite (A) regions, with in-between regions of Pearlite/Bainite (P/B). The Ferrite regions consisted of several, relatively equiaxed ferrite grains. A rather thin carbide layer decorated their grain boundaries. Very fine carbide particles of submicrometric sizes were distributed uniformly within the grain interior. The Ferrite regions contained only small amounts of Si and Mn and around 0.15 % of Mo, while the contents of Ni and Cu were under the detection limit of Energy-Dispersive X-ray Spectroscopy (EDS). Conversely, the austenite contained around 10 % Ni, 3 % Cu and 1 % Mo. The Pearlite/Bainite regions consisted partly of pearlite (lamellar carbides) and upper bainite (elongated carbide particles between ferritic laths). In these

regions, moderate contents of nickel, copper and molybdenum were determined using EDS (around 0.5 % Ni, 0.5 % Cu and 0.25 % Mo).

Further exposure to higher temperatures during austenitisation resulted in a somewhat more homogeneous distribution of the alloying elements and the microstructural constituents, while the volume fraction of ferrite islands decreased considerably. The contents of Ni and Cu increased to 0.03 to 0.05 %, and Mo to around 0.3 %. Carbides at the grain boundaries dissolved during austenitisation, while smaller submicrometric sized carbide particles were distributed uniformly within the ferrite grains, which were presumably formed during tempering. The fraction of austenite decreased, while the contents of Ni and Cu increased compared to the as-sintered condition (≈14 % Ni, 4 % Cu). The content of Mo remained at the same level as prior to the heat treatment (≈1 % Mo). The main volume fraction of the as-hardened specimens represented Martensite (M), which formed during quenching from the austenitisation temperature. It contained ≈0.6 % Ni, 1.1 % Cu and 0.6 % Mo. Their contents were higher than in the Pearlite/Bainite regions of the sintered samples.

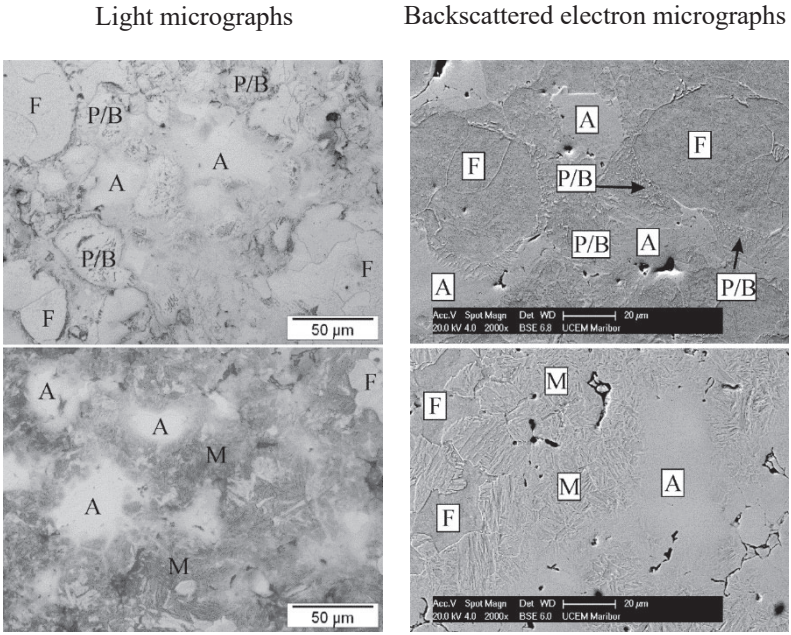

Figure 4.2: Initial microstructures of the as-sintered (above) and as-hardened (below) samples

The static properties of a randomly chosen sample from both sets of specimens (as-sintered and as-hardened) were determined at room temperature on the uni-axial test machine according to the ISO 6892-1 Standard [4.11]. The displacement rate for all quasi-static tests was set to 0.5 mm/min. The basic material properties obtained by quasi-static uni-axial tensile tests on five test specimens from each set are averaged in Figure 4.3 and in Table 4.1, where the Standard Deviation values are also given in brackets. It is evident that additional heat treatment increases the ultimate tensile strength R_m and reduces elongation at breakage A. A slight increase of Young's module E was also observed in the case of as-hardened specimens. When observing the yield point, two different criteria were used; one with 0.1 % plastic deformation $R_{p0.1}$ and the other with 0.2 % plastic deformation $R_{p0.2}$. The results show much higher $R_{p0.1}$ and the absence of $R_{p0.2}$ in the hardened specimens. Detailed information on static mechanical testing and properties can be found in [4.12].

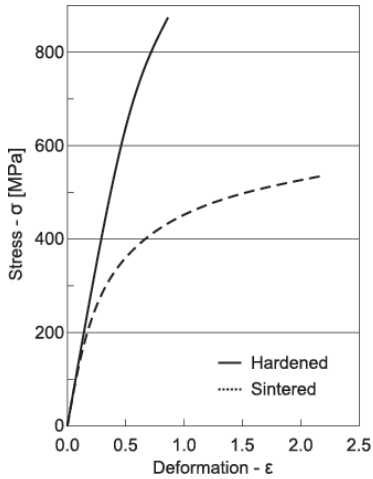

Figure 4.3: Stress-strain curve of the analysed PM-steel

Table 4.1: Static mechanical properties of the analysed PM-steel

Mechanical property		As-sintered specimens	As-hardened specimens
E	[MPa]	130000 (± 2)	142000 (± 3)
$R_{p0.1}$	[MPa]	302 (± 6)	754 (± 14)
$R_{p0.2}$	[MPa]	356 (± 9)	–
R_m	[MPa]	532 (± 27)	965 (± 37)
A	[%]	2.16 (± 0.07)	0.86 (± 0.06)

The Vickers hardness [4.13] was measured on three different specimens from each set in quasi-static specimens and at two positions: In frontal and lateral directions from the compaction movement. Regardless of direction, the hardness of the sintered specimens was from 160 to 180 HV1, and the hardness of the hardened set was between 310 and 340 HV1. The higher hardness in the hardened specimens is a consequence of the martensitic microstructure. The difference is also manifested in the stress/strain plot and in the absence of $R_{p0.2}$ in the hardened specimens. As seen in the micrographs in Figure 4.2, the prevalent microstructure in the hardened specimens was martensite with nickel-rich austenite. When compared to the diverse microstructure of sintered steel, it is predictable that the martensitic needles in hardened sintered steel will prevent dislocation propagation. In contrast, the numerous pores in sintered steel cause many local stress peaks, which are then absorbed into the ductile nickel-rich austenite.

4.2 High-cycle fatigue behaviour of Cu-Ni-Mo sintered steel

When determining the high-cycle fatigue behaviour of analysed PM-steel the same type of specimen as shown in Figure 4.1 has been used. The pulsating fatigue tests (stress ratio $R = 0$) were performed in a force-controlled regime on the same machine as already used for quasi-static testing. To avoid specimen heating due to damping effects [4.14], the pulsating frequency was kept low at 10 Hz, making testing relatively long for cases with more than 10^6 cycles. Measured data was then processed with a best-fit function to obtain material parameters of Basquin's equation [4.15, 4.16].

Several fatigue tests were done at different load levels. Data points were plotted in a $\log(\sigma_a) - \log(N)$ diagram and afterwards the method of least squares was used to find parameters A and b in the Basquin's equation (Eq. 4.1), which suggests a straight-line relationship in a double logarithmic graph:

$$\sigma_a = A \cdot (N)^b \tag{4.1}$$

where σ_a is the applied amplitude stress and N is the number of loading cycles. Parameter A represents the amplitude fatigue strength for 1 cycle and it is only a theoretical value. Parameter b indicates the slope of the S-N line on a logarithmic scale. However, Eq. (4.1) is often written in a slightly different form [4.16, 4.17]

$$\sigma_a = \sigma_f' \cdot (2N)^b \tag{4.2}$$

where parameter A is substituted with $2^b \cdot \sigma_f$'. Fatigue strength coefficient σ_f' represents the theoretical amplitude stress at $N = 0.5$ and it is roughly equal to the true tensile strength for most wrought-metal materials. It can be easily calculated from Eq. (4.1), if parameters A and b are known, by inserting the value of 0.5 for N. Parameter b is the same in both Eqs, (4.1) and (4.2). The results are shown in Table 4.2.

Table 4.2: Material parameters of Basquin's equation

Material parameter	As-sintered specimens	As-hardened specimens
A [MPa]	494	787
b	– 0.121	– 0.153
σ_f' [MPa]	537	875

In addition to Table 4.2, Figure 4.4 shows the difference in fatigue strength between both sets of specimens graphically. The fatigue parameters were obtained in the region between 10^2 and 10^6 cycles for hardened specimens and between 10^3 and 10^6 cycles for sintered specimens. It is evident that the hardened specimens showed higher fatigue strength between 10^3 and 10^4; however, the difference between 10^5 and 10^6 stress cycles was less profound.

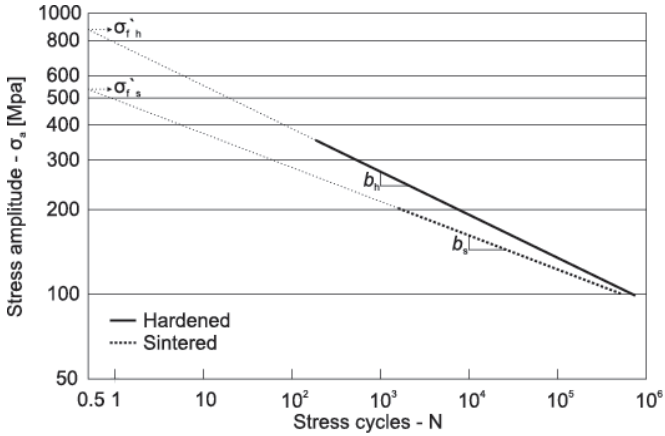

Figure 4.4: S-N diagram of the analysed PM-steel

When comparing the fatigue strengths at 10^4 cycles, the calculated value from the S–N line is 192 MPa for the hardened specimens and 162 MPa for the sintered specimens. From Figure 4.4 it is evident that the difference in the fatigue strength dissipates gradually. The fatigue strength at 10^5 cycles is almost the same for both sets of specimens (≈135 MPa for the hardened and ≈123 MPa for the sintered specimens). Figure 4.4 also suggests that the S–N lines would cross each other after 10^6 cycles, but this is inconclusive because there are no data points after 10^6 cycles. Therefore, based on the available data, the amplitude strength cannot be determined at 10^6 cycles and additional testing should be performed to find if the S–N lines cross each other after 10^6 cycles.

Although typical fatigue striations are not expected to be clearly visible in sintered steel, some SEM scans were taken for the fatigue specimens and are shown in Figure 4.5 for sintered and in Figure 4.6 for hardened specimens. Each of the Figures consists of two images; the one on the right is taken from the marked rectangle in the left image. In the right image of both Figures, striations are marked with a rectangle with arrows that are perpendicular to the striations. From the size of the striations, it can be assumed that, at the early stages of crack formation, when individual pores are starting to coalesce, diffusion bonds begin to collapse, causing larger defect areas, raising stress concentrations and causing an unstable breakage in the next few cycles [4.18].

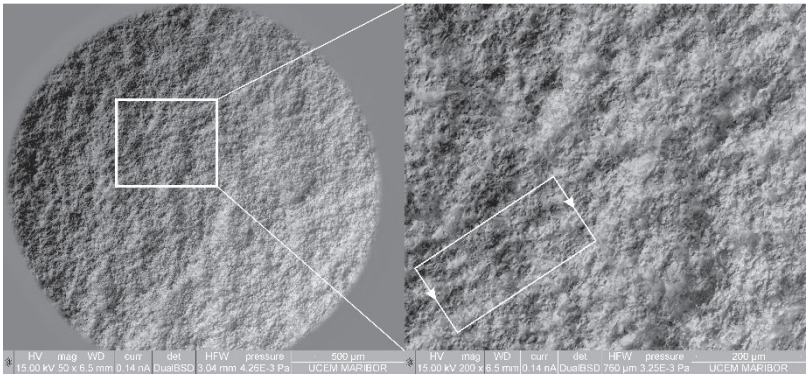

Figure 4.5: SEM micrograph of sintered PM-steel

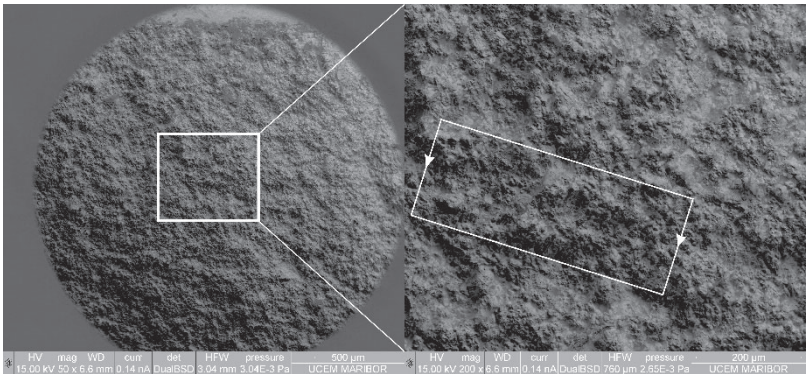

Figure 4.6: SEM micrograph of hardened PM-steel

4.3 Low-cycle fatigue behaviour of Cu-Ni-Mo sintered steel

When determining the low-cycle fatigue behaviour of the analysed PM-steel the same type of specimen was used as shown in Figure 4.1. Low-cycle fatigue tests were performed on the servo-hydraulic testing machine LFV-50-HH (Figure 4.7a) using a 50 kN load cell. The tests were conducted at room temperature under load control. Sinusoidal loading was applied in pulsating tension with stress ratio $R = 0.1$ at the loading frequency $f = 0.5$ Hz. Extension of the specimens was measured by contact extensometer, as shown in Figure 4.7b.

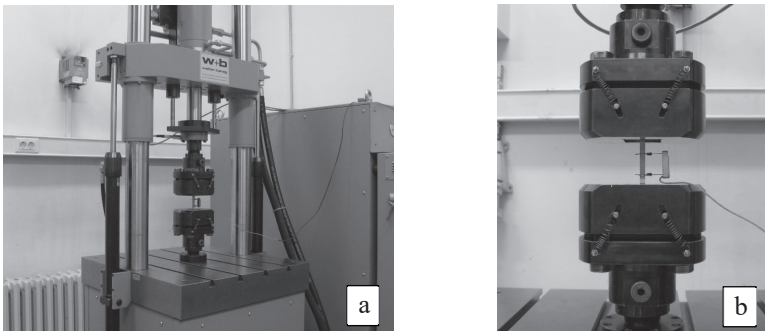

Figure 4.7: Test setup (a) and extensiometer (b)

As described in [4.19–4.21], the failure criteria for strain-life curves may be the life to a small detectable crack, life to a certain percentage decrease in tensile load, or life to fracture. In the presented study, all specimens were tested until fracture, and the appropriate number of stress cycles was designated with N_f. Up to five test specimens were tested for each stress level (see Table 4.3).

Table 4.3: Maximum stress σ_{max} during the experimental testing

As-sintered specimens		As-hardened specimens	
σ_{max} = 446 MPa	3 specimens	σ_{max} = 614 MPa	4 specimens
σ_{max} = 418 MPa	3 specimens	σ_{max} = 587 MPa	5 specimens
σ_{max} = 390 MPa	3 specimens	σ_{max} = 561 MPa	3 specimens
σ_{max} = 446 MPa	2 specimens		

During the testing no typical stable hysteresis loop was formed, as is usually the case with some other engineering materials. Therefore, the hysteresis loop at the 50 % point of the specimen fatigue life was considered for the subsequent determination of low–cycle fatigue parameters (see Figure 4.8).

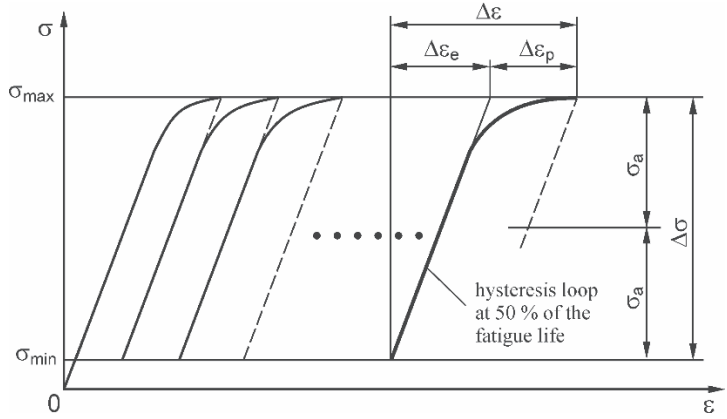

Figure 4.8: True stress versus true strain behaviour of the analysed PM-steel

The hysteresis curves shown in Figure 4.8 can be described using the following equation [4.16, 4.19]:

$$\Delta\varepsilon = \Delta\varepsilon_e + \Delta\varepsilon_p = \frac{\Delta\sigma}{E} + 2\left(\frac{\Delta\sigma}{2K'}\right)^{1/n'} \tag{4.3}$$

where $\Delta\varepsilon$ is the total strain range, $\Delta\varepsilon_e$ and $\Delta\varepsilon_p$ are the elastic and plastic strain ranges, respectively, $\Delta\sigma$ is the stress range, E is the modulus of elasticity, K' is the cyclic strength coefficient and n' is the cyclic strength hardening exponent. Only the plastic strain should be considered when determining the material parameters K' and n':

$$\frac{\Delta\sigma}{2} = \sigma_a = K'\left(\frac{\Delta\varepsilon_p}{2}\right)^{n'} \tag{4.4}$$

The strain-life fatigue curves are usually plotted on log-log scales using the amplitude values of treated magnitudes, and can be described mathematically as follows:

$$\varepsilon_a = \frac{\Delta\varepsilon}{2} = \frac{\Delta\varepsilon_e}{2} + \frac{\Delta\varepsilon_p}{2} = \frac{\sigma_f'}{E}(2N_f)^b + \varepsilon_f'(2N_f)^c \tag{4.5}$$

where σ_f', b, ε_f' and c are the low-cycle fatigue parameters for the tested material, and N_f is the number of stress cycles until failure. In the presented study, it should be noted that the material parameters σ_f', b, ε_f' and c were determined for the stress ratio $R \approx 0.1$.

Figure 4.9 shows the relationship between fatigue life and the applied stress amplitude for both as-sintered and as-hardened specimens. It can be observed that the additional hardening increased the fatigue strength of the material significantly. However, a typical scatter of experimental results can be observed for both as-sintered and as-hardened specimens, which is typical for porous materials.

Figure 4.10 shows the relationship between the plastic strain amplitude and the applied stress amplitude, plotted in a log-log scale for both as-sintered and as-hardened specimens. The experimental results can be approximated with a linear relationship, where the cyclic strength coefficient K' represents the stress intercept at $\Delta\varepsilon_p/2 = 1$, while the cyclic strength hardening exponent n' is a slope of the approximation line. It can be observed that the parameter n' is very similar for both cases. However, the recorded cyclic strength coefficient K' for as-hardened material is significantly higher as opposed to the as-sintered material (see also Table 4.4).

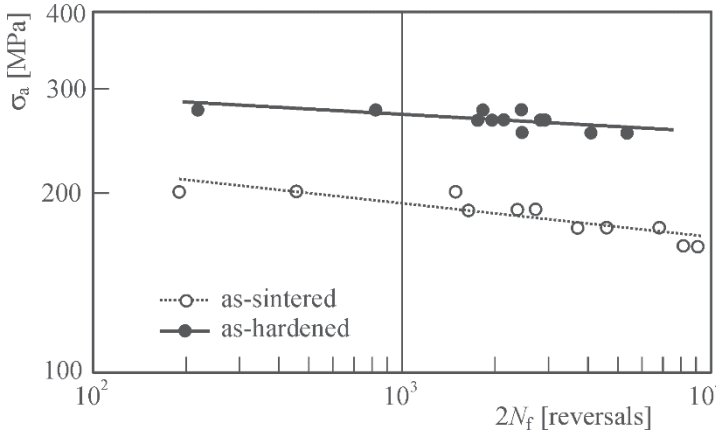

Figure 4.9: Relationship between fatigue life and applied stress amplitude

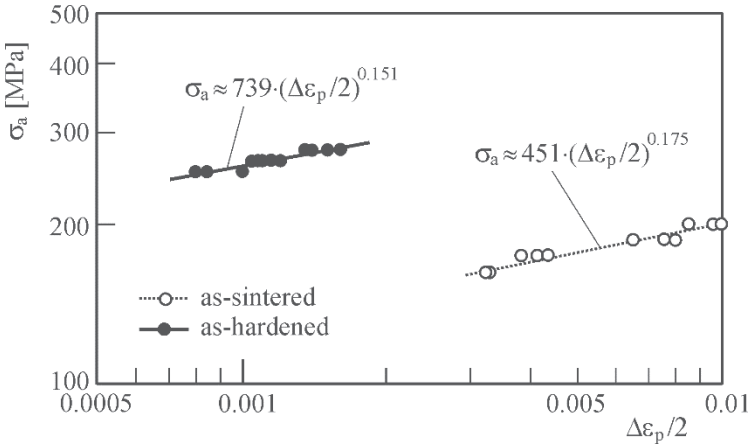

Figure 4.10: Relationship between the plastic strain amplitude and the applied stress amplitude

Figures 4.11 and 4.12 show the relationship between the fatigue life and the strain amplitudes plotted in log-log scales. According to eq. (4.5), the total strain amplitude $\Delta\varepsilon/2$ can be divided into elastic ($\Delta\varepsilon_e/2$) and plastic ($\Delta\varepsilon_p/2$) strain components from which the low-cycle fatigue parameters σ_f', b, ε_f' and c can be determined. Here, it should be pointed out that the appropriate modulus of elasticity E has to be considered when determining the fatigue

strength coefficient σ_f'. The complete results for the experimentally determined low-cycle fatigue parameters are summarised in Table 4.4.

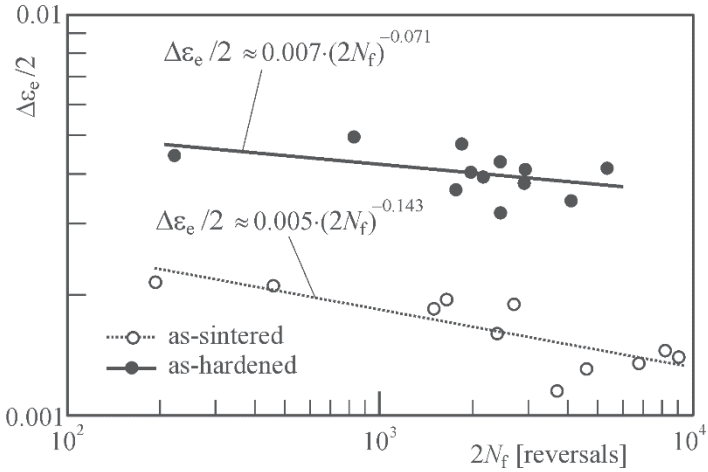

Figure 4.11: Relationship between fatigue life and the elastic strain amplitude

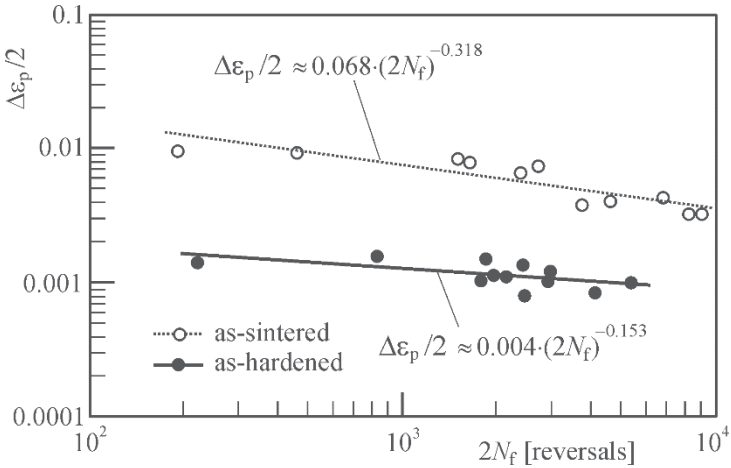

Figure 4.12: Relationship between the fatigue life and the plastic strain amplitude

Table 4.4: Low-cycle fatigue parameters of the tested material at stress ratio $R \approx 0.1$

Parameter		As-sintered	As-hardened
Cyclic strength coefficient	K' [MPa]	451	739
Cyclic strength hardening exponent	n' [–]	0.175	0.151
Fatigue strength coefficient	σ_f' [MPa]	530	721
Fatigue strength exponent	b [–]	–0.143	–0.071
Fatigue ductility coefficient	ε_f' [–]	0.068	0.004
Fatigue ductility exponent	c [–]	–0.318	–0.153

Figure 4.13 shows some fractured specimens. The cracks propagated mainly perpendicular to the longitudinal axis (stress axis). They were not straight, but followed a zigzag path. One of the as-hardened specimens failed outside the extensometer range, with no other cracks evident within the test section. Based on the engineering judgement [4.22], this data point was reviewed and tagged valid, since the half-life strain and life were consistent with the trend created by the other as-hardened specimens.

A typical microstructure of the fractured surface of an as-sintered specimen is shown in Figure 4.14. At the surface (and up to 200 μm below the surface), the pore fraction and sizes were much higher than elsewhere. This fact indicates that the cracks followed the weakest path during their propagation; that is, the regions with the highest fraction of porosity. The same conclusion can be obtained by inspection of the fractured surfaces (see Figure 4.15a). There, large smooth regions (s) can be observed, indicating that the powder had not been joined together during sintering. The fractured as-sintered specimens also showed a combination of brittle and ductile fracture. The brittle fracture (b) showed a typical cleavage appearance that occurred by the propagation of a crack through the Ferrite regions. This fact was also confirmed by the results of the EDS-analysis. The composition in the regions of ductile fracture varied considerably, but their composition corresponded mainly to the compositions of Austenite and Pearlite/Bainite regions. The fracture surfaces of the as-hardened specimens (Figure 4.15b) showed only ductile character (d), with dimples of several sizes. The ferritic regions were too small to induce a brittle fracture. The dimples formed mainly in the ductile Austenite regions.

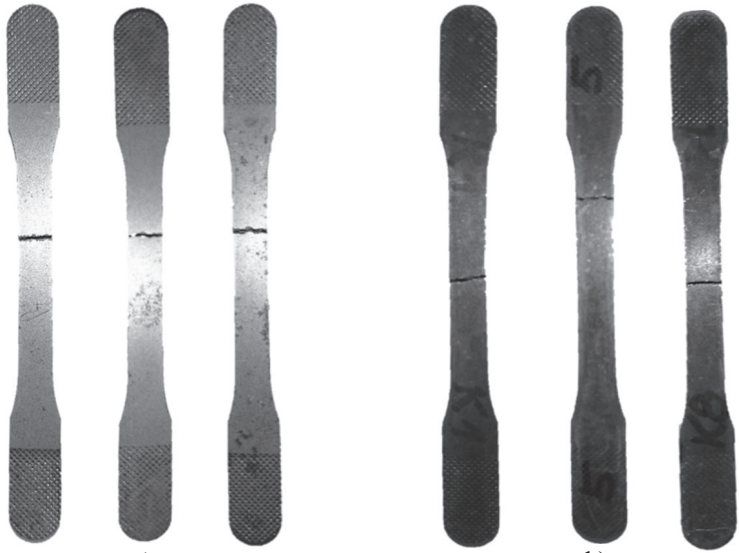

Figure 4.13: Fracture examples of as-sintered (a) and as-hardened (b) specimens

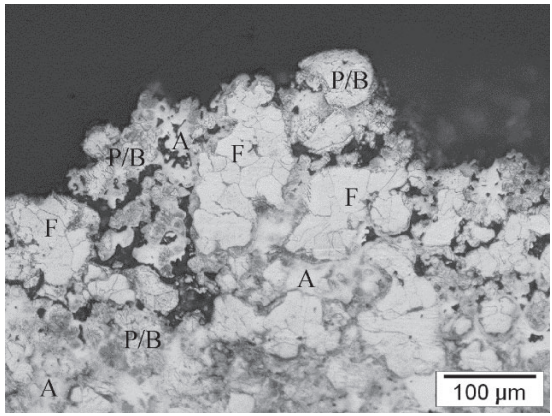

Figure 4.14: Light micrograph of a fractured as-sintered specimen [4.23]

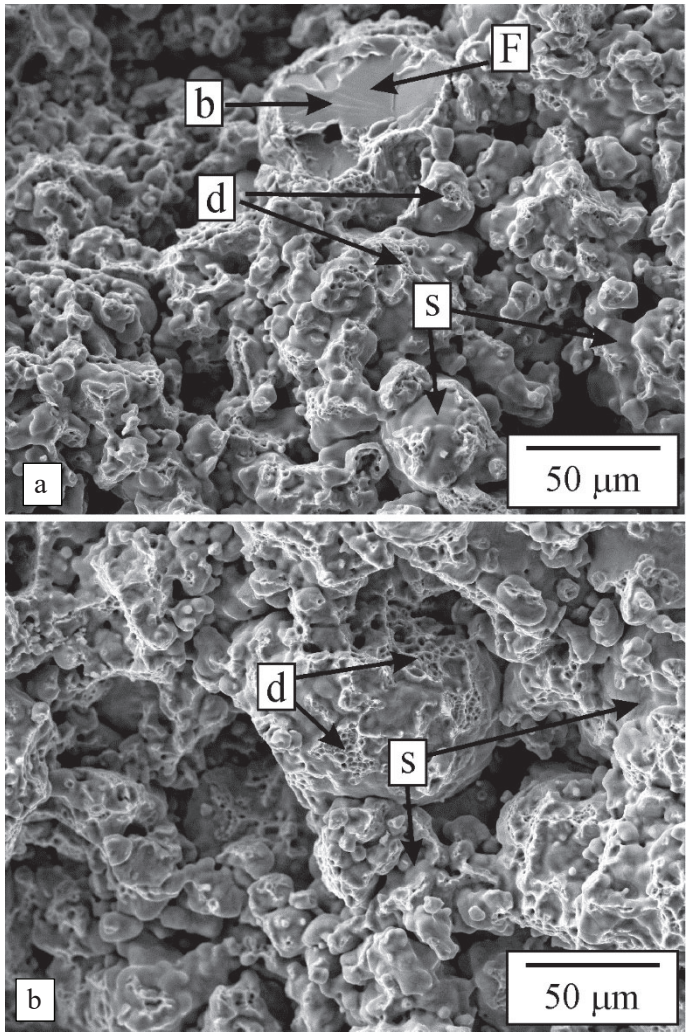

Figure 4.15: Secondary Electron Micrographs of a fractured as-sintered specimen (a) and as-hardened specimen (b) [4.23]
(b) brittle, (d) ductile, (s) smooth

4.4 Crack growth and fracture analysis of Cu-Ni-Mo sintered steel

The crack growth and fracture analysis of treated PM-steel were performed using standardised experimental testing. The crack growth rate from the threshold region through the stable crack growth region to the unstable breakage was investigated using the specimens shown in Figure 4.16a with a height of 10 mm, which were cut out from sintered rounds using Wire Electric Discharge Machining (WEDM). The used specimens are practically the same as standard specimens for the impact toughness evaluation according to ISO 14556 Standard [4.24], only instead of 55 mm in length, they were 100 mm long to ensure a better grip on a Rumul Cracktronic device. Measuring foil of type RMF A-5 was placed on each side of the specimen, to enable automatic crack length detection. The testing was performed in a regime with a computer-controlled intensity factor range of ΔK. It began with low ΔK values, which were increased gradually to obtain stable crack growth. Afterwards, the ΔK value was decreased until the crack growth rate was below 1 μm per 10^6 load cycles, which determined the crack growth threshold value ΔK_{th}. This also ensured that the crack front had passed the "white layer" or Heat-Affected Zone (HAZ), which may have been caused by the WEDM [4.25]. When the threshold was determined, the ΔK value was again increased gradually until unstable breakage occurred.

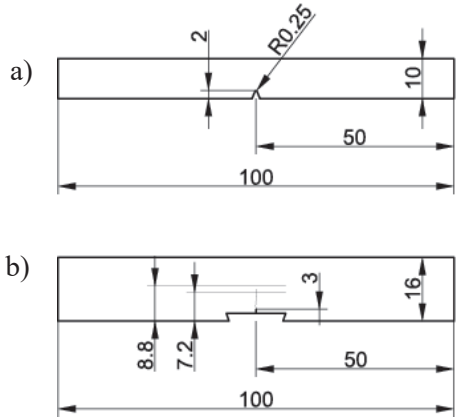

Figure 4.16: Test specimens for stable crack growth analysis (a) and determination of fracture toughness (b)

Due to rapid crack propagation in the region of unstable crack growth, the evaluation of critical stress intensity factor K_{Ic} was not possible. Therefore, to establish the full fracture behaviour of the chosen PM-steel, fracture toughness was evaluated on specimens according to the standard ASTM E1820 [4.26], shown in Figure 4.16b, with a thickness of 8 mm. Ten specimens were cut from sintered rounds using WEDM. Half of the specimens were then additionally heat treated and marked as Hc1 to Hc5, while the remaining five were left in the sintered state and marked as Sc1 to Sc5. An initial 3 mm long and 0.65 mm wide WEDM-produced notch served as a seam to produce a fatigue crack of 7.2 to 8.8 mm long on a Rumul Cracktronic device. The prepared specimens were then subjected to bending load at room temperature on round supports 64 mm apart with the load applied in the middle, on the opposite side of the initial crack. Bending force and Crack Mouth Opening Displacement (CMOD) were measured until breakage, as specified in ASTM E1820. Specimens were then subjected to 200 °C to oxidise the crack surface, which enabled better visualisation of the remaining ligament. With both procedures, the crack growth rate da/dN to stress intensity factor range ΔK relation can be plotted in a log (da/dN) – log ΔK diagram. In principle, such a plot consists of three regions: The crack growth threshold ΔK_{th} at the lowest ΔK values and fracture toughness K_{Ic} or K_c near the highest ΔK values; in between, a linear section of crack growth rate to stress intensity factor range relation is defined using the Paris law, written in Eq. (4.6), with material-specific parameters C and m.

$$\frac{\mathrm{d}a}{\mathrm{d}N} = C \cdot (\Delta K)^m \tag{4.6}$$

Figure 4.17 shows the experimental results of the crack growth rate for 6 sintered specimens (S1 to S6). The linear section was calculated for 9.9 MPa√m < ΔK < 20.2 MPa√m on data points from all specimens. The determination of the interval was based on the regression value, which was 91.23 %, and increased rapidly when the interval was extended in either direction. The large scattering of data points is most likely a consequence of different sizes, shapes, shares and distributions of the pores in the material [6]. The noted threshold value for crack growth for sintered-only specimens is ΔK_{th} = 5.197 MPa√m.

Figure 4.18 shows measurements of the crack growth rate for 6 hardened specimens (H1 to H6). The linear section was calculated for 8.0 MPa√m < ΔK < 19.9 MPa√m on data points from all specimens. The selection of the interval was also based on the regression value, which was 96.05 %. The

higher regression value in the hardened specimens shows less scattering than in the sintered specimens. The noted threshold value for crack growth in the hardened specimens is $\Delta K_{th} = 5.240$ MPa$\sqrt{m}$.

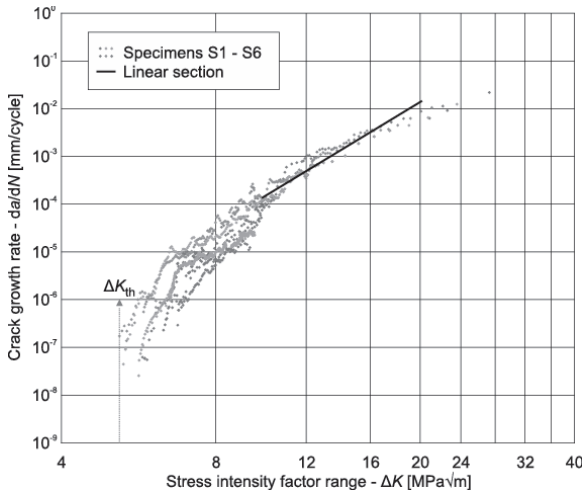

Figure 4.17: The diagram log(Δ*K*) – log(d*a*/d*N*) for sintered specimens

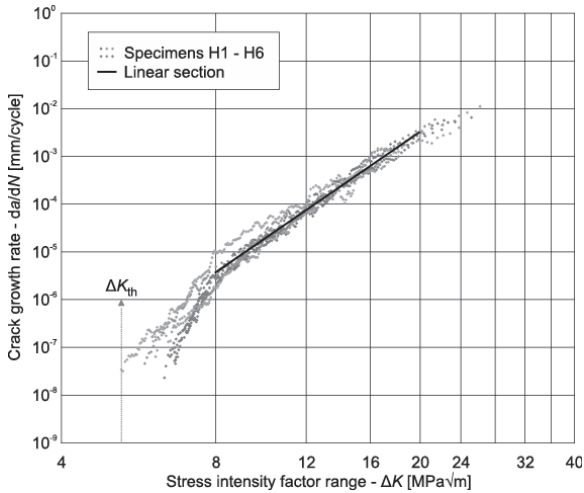

Figure 4.18: The diagram log(Δ*K*) – log(d*a*/d*N*) for hardened specimens

Figure 4.19 shows the test specimen with measuring foils before and after crack growth rate measurements. The final crack is clearly visible, and it appears that the crack path changes direction slightly. This change of direction is caused by the inhomogeneity of the material and could cause a potential drop proportional to crack length in the bonded foil. However, an angle of 10 deg would cause an error of only 2 % and is less problematic than the scatter.

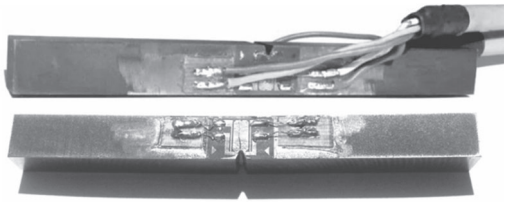

Figure 4.19: Test specimen before (above) and after (below) crack growth rate measurement

To establish the full fracture mechanics' behaviour of the given PM-steel, 5 sintered and 5 hardened specimens (Sc1 to Sc5 and Hc1 to Hc5) were used to determine the fracture toughness according to the ASTM E1820 Standard [4.26]. As the threshold values and the stable crack growth parameters were already known, the fatigue crack was produced on the same Rumul Cracktronic testing device, but without measuring foils. Consequently, the crack propagation was monitored visually and the load withdrawn manually when the crack reached the desired length according to ASTM E1820. In the cases of specimens Sc2, Sc5 and Hc2, the crack front propagated too quickly through the desired area, and was not stopped in time; therefore, those specimens were discarded from further analysis.

According to the ASTM E1820 Standard, certain criteria must be fulfilled to prove linearly elastic fracture mechanics and plane strain conditions. One of them is the uniform fatigue crack length through the thickness of the specimen. To check this criterion, crack surfaces were observed under a microscope and the fatigue crack length was measured through the thickness. Images of crack surfaces are shown in Figures 4.20 and 4.21 with 350 dpi resolution, along with the measured distances on sintered and hardened specimens, respectively. Due to uneven fatigue crack lengths, specimens Sc1, Hc1, and Hc3 were excluded from K_{Ic} calculations. Only 2 specimens of the hardened set passed the full criteria and yielded K_{Ic} values, that are averaged in Table 4.5 and marked as K_{Ic}^{ASTM}. The plastic region of

the remaining 2 sintered specimens was too large according to the criteria; therefore, no regular K_{Ic}^{ASTM} could be calculated for the sintered specimens.

Since a complete comparison between both sets would be impossible without the K_{Ic} values for the sintered set, an alternative energy method [4.28] was used to find the K_{Ic} values for the sintered specimens. Due to the different procedure in the ASTM E1820 Standard, the fracture toughness values could not be compared directly. Therefore, both sets were calculated according to this method, and are marked as K_{Ic}^{Witt} (see also the results in Table 4.5). Further analysis of fracture resistance was made with impact toughness determination according to the standardised Charpy V-notch test [4.24] at room temperature. Three sintered and three hardened standard specimens were tested, and the results are given in Table 4.5, marked as KV-values.

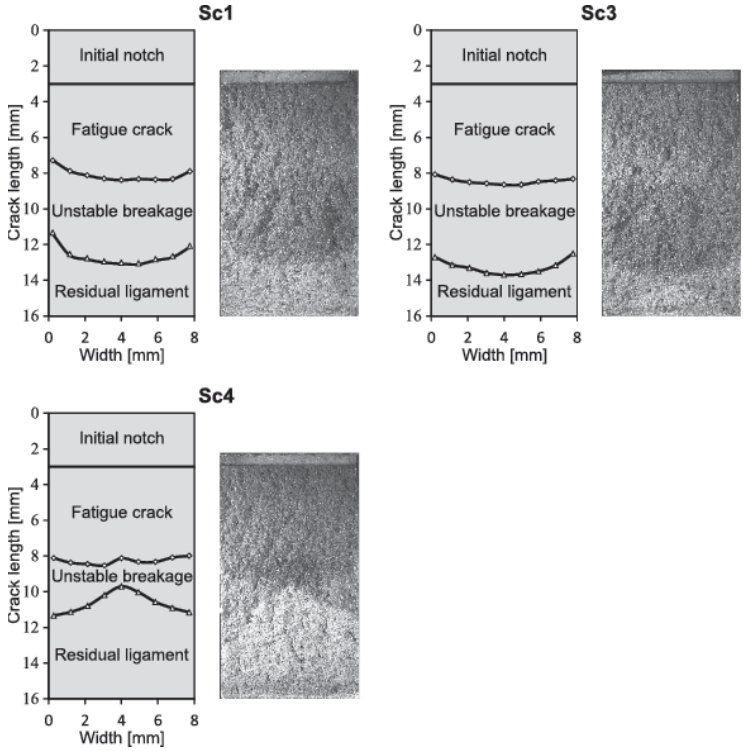

Figure 4.20: Crack surfaces of sintered specimens

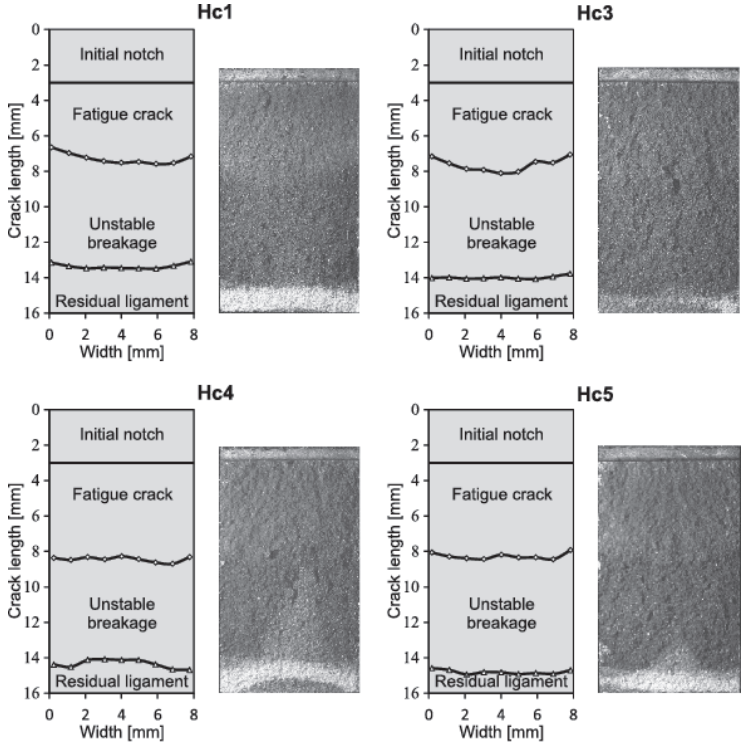

Figure 4.21: Crack surfaces of hardened specimens

Table 4.5: Complete comparison of crack growth and crack growth resistance parameters

Crack growth parameters	ΔK_{th} [MPa√m]	C [MPa√m]	m [ ]
Sintered	5.197	$4.896 \cdot 10^{-11}$	6.440
Hardened	5.240	$7.824 \cdot 10^{-11}$	7.396
Crack resistance parameters	K_{Ic}^{ASTM} [MPa√m]	K_{Ic}^{Witt} [MPa√m]	KV [J/cm²]
Sintered	/	35.9	7.37
Hardened	25.45	30.1	6.08

The complete comparison of both types of materials regarding their responses to crack presence is given in Figure 4.22, with the parameters written in Table 4.5. It is evident that both types of material have roughly the same threshold values at around 5.2 MPa√m, which are similar to those found by Gerosa et al. [4.29]. With an increase in the stress intensity factor range, the crack growth rate was higher in the sintered specimens. However, after the linear portion of the curve within the unstable breakage zone, the ductility of the sintered specimens seemed to lower the crack growth rate, which is seen from the higher K_{Ic}^{Witt} values in the sintered specimens. The greater ductility is also seen from the fracture toughness values *KV*, and, nevertheless, also from the static response to tensile load. The calculated K_{Ic}^{ASTM} value can be compared with the results of other researchers, and it is well within the typically expected values of between 20 and 35 MPa√m for sintered PM steel with a density of 7.0 g/cm³ and above [4.30].

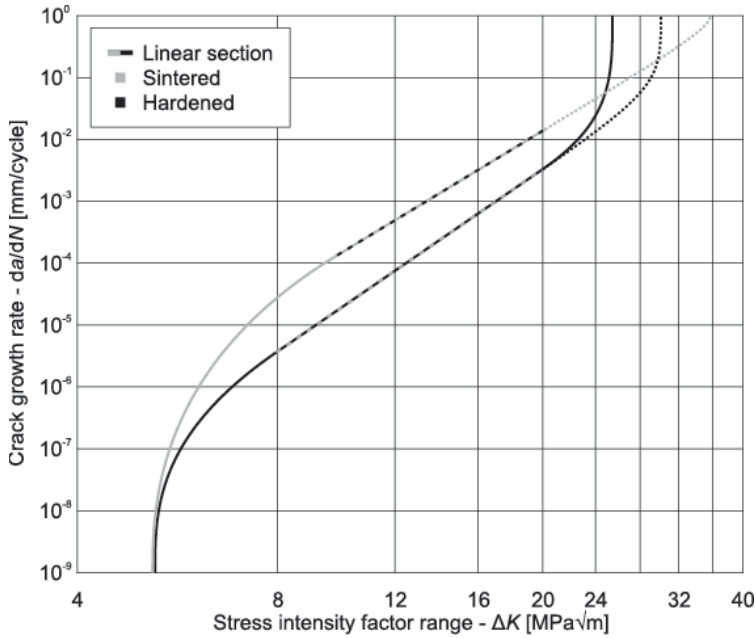

Figure 4.22: Comparison between the crack growth rate in the sintered and hardened specimens

4.5 Conclusions

This study provides a comprehensive overview of the mechanical, fatigue and fracture properties of diffusion alloyed Cu-Ni-Mo sintered steel. The proposed experimental investigation of the analysed PM-steel focused on the potential influence of the additional hardening of base material on the investigated mechanical, fatigue and fracture properties.

Monotonic tensile tests were done before the fatigue and fracture mechanics' testing. The experimental results showed that the ultimate tensile strength for the sintered and hardened specimens was found to be 532 MPa and 965 MPa, respectively. Additional heat treatment also decreased the elongation at breakage from 2.16 % to 0.86 %. Based on these findings it can be concluded that the hardening of the analysed PM-steel increases tensile strength and decreases ductility.

High-cycle fatigue testing

The high-cycle fatigue behaviour of the analysed PM-steel was investigated under pulsating loading with the load ratio $R = 0$. The acquired data were then used to calculate the parameters of Basquin's equation with the least-squares method, and the S–N lines for both sets of specimens were plotted in log-log diagrams. Based on the obtained experimental results, the following conclusions can be made:

- The additional heat treatment (hardening) increases the fatigue strength significantly, up 10^4 loading cycles; after this point, the effect of hardening is small and can be neglected.
- The S–N lines would cross each other after 10^6 cycles, but this is inconclusive, because there are no data points after 10^6 cycles in this study. Therefore, based on the available data, the fatigue strength cannot be determined at 10^6 cycles, and additional testing should be performed to find if the S–N lines cross each other after 10^6 cycles.
- Experimental testing in the area $N > 10^6$ should also be performed to determine the fatigue limit for both sets of specimens.
- From the metallographic investigation, it can be assumed that, at the early stages of crack formation, when individual pores are starting to coalesce, diffusion bonds begin to collapse, causing larger defect areas, raising stress concentrations and causing an unstable breakage in the next few cycles.

Low-cycle fatigue testing

The low-cycle experimental testing was performed on a servo-hydraulic testing machine under load control with stress ratio $R = 0.1$. The metallography of the initial microstructure and fracture surfaces was examined using a light microscope and two Scanning Electron Microscopes. Based on the experimental results and complete metallography of the initial microstructure and fracture surfaces, the following conclusions can be made:

- The fatigue tests have shown that additional hardening increases the fatigue strength of a tested material significantly. When the service life is given in advance, the appropriate amplitude dynamic strength is approximately 35 % to 40 % higher for as-hardened specimens as opposed to as-sintered specimens.
- The initial microstructure of treated PM-steel was found not uniform for both as-sintered and as-hardened specimens.
- The fracture surfaces consisted of smooth regions in both as-sintered and hardened specimens, which indicated the surfaces of pores. The as-sintered specimens displayed a combination of brittle and ductile fracture, while only dimples were observed for the as-hardened specimens, occurring mainly in the austenitic regions.
- The determined low-cycle fatigue parameters σ_f', b, ε_f' and c are helpful in estimating the number of loading cycles required for the fatigue crack initiation of different machine parts and structural elements made of treated sintered steel in both as-sintered or as-hardened conditions.

Crack growth and fracture analysis

Due to much lower elongation at breakage during the static tests, the hardened sintered steel seemed more brittle than before hardening. If both sets of material are compared regarding fracture and impact toughness, the hardened set seemed more brittle again. However, the comparison of material sets within the stable growth zone revealed a noticeably slower crack growth rate in the hardened set. While both sets had roughly the same randomly distributed defects through the volume, the combination of martensitic and austenitic microstructures prevented crack propagation better than the colourful microstructure of the sintered set did. Hard martensitic needles stop dislocations, while ductile nickel-rich austenite prevents micro-crack coalescence and propagation. Based on these findings, the following conclusions can be made:

- There is no significant difference in the crack growth threshold between sintered and hardened sintered steel.
- The crack growth rates in the stable crack growth region are lower in hardened sintered steel.
- The fracture toughness and impact toughness of sintered steel are higher than in hardened sintered steel.

Although many experimental tests have been done, there is still some work to do regarding the evaluation of the endurance limit and short crack propagation in sintered steel. Nevertheless, the material properties given in this study give a comprehensive overview of macroscopic material responses to different loads and to internal defects. This work covers material response to static loads, microstructure and hardness evaluation, response to dynamic loads, impact toughness and complete analysis of the response to the presence of long cracks.

References

[4.1] Campbell-Tremblay J., St-Laurent S., Effect of Ni and Cu addition on pre-alloyed Mo powders designed for high-performance applications, Proceeding of Euro PM Congress on powder metallurgy, Salzburg, Austria, 2014.

[4.2] Bergmark A, Alzati L., Fatigue crack path in Cu-Ni-Mo alloyed PM steel, *Fatigue Fract Engng Mater Struct*, 28, 2005, 229–235.

[4.3] Lichanska E., Kulecki P., Pancikiewicz K., The structure and mechanical properties of Ni-Mo PM steels with the addition of Mn and Cu, *Powder Metallurgy Progress*, 17, 2017, 37–46.

[4.4] Anklekar R.M., Bauer K., Agrawal D.K., Roy R., Improved mechanical properties and microstructural development of microwave sintered copper and nickel steel PM parts, *Powder Metallurgy*, 48, 2005, 39–46.

[4.5] Saager R., Stephens R. I., Prucher T., Influence of density and sintering temperature on monotonic, cyclic and low cycle fatigue behaviour of FL4405 high strength PM steel, *Powder Metallurgy*, 41, 1998, 103–108.

[4.6] Cias A., Stoytchev M., Nickel and Copper-free sintered structural steels containing Mn, Cr, Si, and Mo developed for high performance application, *Arch. Metall. Mater.*, 62, 2017, 11–17.

[4.7] DIN 30910-4, 2010. Sintered metal materials: Sintered material specifications – Part 4: Materials for structural parts, German standard, Berlin.

[4.8] Candela, N., Velasco, F., Martinez, M.A., Torralba, J.M., Influence of microstructure on mechanical properties of molybdenum alloyed P/M steel, *Journal of Materials Processing Technology*, 168, 2005, 505–510.
[4.9] Khraisat, W., Nyborg, L., Effect of carbon and phosphorus addition on sintered density and effect of carbon removal on mechanical properties of high density sintered steel, *Materials Science and Technology,* 20, 2004, 705–710.
[4.10] Nabeel, R., Frykholm, R., Hedstrom, P., Influence of alloying elements on Ni distribution in PM steels, *Powder Metallurgy*, 57, 2014, 111–118.
[4.11] ISO 6892-1:2019, Metallic materials–Tensile testing–Part 1: Method of test at room temperature, International Standard Organization, Geneve, Switzerland, 2019
[4.12] Šori M., Verlak T., Glodež S., Heat Treatment Effects on Static and Dynamic Mechanical Properties of Sintered SINT D30 Powder Metal, *Key Engineering Materials*, 592, 2014, 643–646.
[4.13] ISO 6507-1:2005, Metallic Materials: Vickers hardness test, International Standard Organization, Geneve, Switzerland, 2005.
[4.14] Dlapka M., Danninger H., Gierl C., Klammer E., Weiss B., Khatibi G., Fatigue Behaviour and Wear Resistance of Sinter-Hardening Steels, *International Journal of Powder Metallurgy*, 48, 2012, 49–60.
[4.15] Basquin O., The exponential law of endurance tests, *Proceedings of American Society for Testing Materials*, 10, 1910, 625–30.
[4.16] Stephens R.I., Fatemi A., Stephens R.R., Fuchs H.O., *Metal fatigue in engineering*, John Wiley & Sons Inc., New York, 2001.
[4.17] Sori M., Sustarsic B., Glodez S., Fatigue Properties of Sintered DIN SINT D-30 Powder Metal Before and After Heat Treatment, *Materiali in Tehnologije*, 48, 2014, 837–40.
[4.18] Sori M., Vuherer T., Glodez S., Fatigue and fracture parameters of diffusion alloyed Cu-Ni-Mo sintered steel, *Engineering Fracture Mechanics*, 153, 2016, 278–288.
[4.19] Dowling N.E., *Mechanical Behaviour of Materials*, Prentice Hall, New Jersey, 1999.
[4.20] Draper J., *Modern Metal Fatigue Analysis*, Emas Publishing, Warrington, 2007.
[4.21] Radaj D., *Ermüdungsfestigkeit*, Springer Verlag, Heidelberg, 2003. (in German).

[4.22] Williams C.R., Lee L., Rilly J.T. A practical method for statistical analysis of strain–life fatigue data, *International Journal of Fatigue*, 25, 2003, 427–436.
[4.23] Glodež S., Vučković K., Šori M., Šurjak M., Zupanič F., The influence of thermal treatment on the low-cycle fatigue behaviour of Cu-Ni-Mo sintered steel, *Mechanics of Materials*, 129, 2019, 57–62.
[4.24] ISO 14556:2015, Metallic materials - Charpy V-notch pendulum impact test - Instrumented test method, International Standard Organization, Geneve, Switzerland, 2015.
[4.25] Huang C., Hsu F., Yao S., Microstructure analysis of the martensitic stainless steel surface fine-cut by the wire electrode discharge machining (WEDM), *Materials Science and Engineering A,* 371, 2004, 119–126.
[4.26] ASTM E1820-15, Standard Test Method for Measurement of Fracture Toughness, ASTM International, West Conshohocken, PA, USA, 2015.
[4.27] Chawla N., Deng X.. Microstructure and mechanical behaviour of porous sintered steels, *Materials Science and Engineering: A*, 390, 2005, 98–112.
[4.28] Witt F., The Equivalent Energy Method - An Engineering Approach to Fracture, *Engineering Fracture Mechanics*, 14, 1981, 171–87.
[4.29] Gerosa R., Rivolta B., Tavasci A., Silva G., Bergmark A., Crack initiation and propagation in Chromium pre-alloyed PM-steel under cyclic loading, *Engineering Fracture Mechanics*, 75, 2008, 750–759.
[4.30] Kabatova M., Dudrova E., Wronski A. Microcrack nucleation, growth, coalescence and propagation in the fatigue failure of a powder metallurgy steel, *Fatigue & Fracture of Engineering Materials & Structures*, 32, 2009, 214–22.

CHAPTER 5

FATIGUE BEHAVIOUR OF AL-ALLOYS PRODUCED BY AM-TECHNOLOGIES

5.1 Introduction

Additive Manufacturing (AM) is a fabrication process which provides unique opportunities to manufacture customised parts with complex shapes from Computer Aided Design (CAD) or Functionally Graded Materials (FGM) [5.1–5.3]. Many Additive Manufacturing technologies are currently being used in different engineering applications, especially in the Automotive and Aerospace industries [5.4–5.6]. Direct Metal Laser Sintering (DMLS) and Selective Laser Melting (SLM) are Powder Bed Fusion (PBF) processes capable of fabricating near fully dense metal components with complex geometries by melting successive layers of metal powders selectively. They show a great potential to make metallic cellular lattice structures beyond the current limitations. Recent studies have employed DMLS to build lattice structures using different metal materials, including stainless steel [5.7], titanium alloys [5.8], aluminium alloys [5.9], etc. Although there are some other AM-technologies often used in engineering praxis (Electron Beam Melting-EBM, Laser Metal Deposition- LMD etc.), DMLS and SLM techniques are particularly widespread, especially for aluminium alloy processing [5.10, 5.11].

The EOSINT M-Systems [5.12] are one of the most popular systems to produce different components (prototypes, series production parts, spare parts, etc.) using DMLS or SLM technology. Here, the metal powder is fused into a solid part by melting it locally using a focused laser beam. The parts are built up additively layer by layer. Even highly complex geometries can be created directly from 3D CAD data, fully automatically, without any tooling. The AM-parts produced by this technique have a high accuracy, good surface quality and excellent mechanical properties.

The fatigue behaviour of AM-parts is not yet well understood, thus delaying the widespread adoption of this advanced manufacturing technology in a

variety of engineering applications. In general, the fatigue strength of AM-parts depends primarily on their microstructure. Here, it should be taken into account that the manufacturing process using AM-technology usually leads to an increased surface roughness, causing increased stress concentration and early failure of AM parts under fatigue loading in as fabricated condition [5.13, 5.14]. Mechanical surface treatments (e.g. polishing) improve the fatigue behaviour, but it is sometimes difficult to use (e.g. for AM lattice structures [5.15]). However, material defects such as porosity and insufficient layer bonding could result in increased scatter of the experimental data rendering an assessment of the fatigue properties rather difficult [5.16].

5.2 Fatigue behaviour of DMLS AlSi10Mg alloy

The aluminium alloy AlSi10Mg is used widely in the Aerospace and Automotive industries because of its high specific strength and high corrosion resistance [5.17, 5.18]. Recently, several investigations have been focused on the determination of the mechanical properties of AM AlSi10Mg alloy considering the process optimisation [5.19–5.21], surface roughness [5.22, 5.23], crystallographic texture [5.24, 5.25], hardness [5.26, 5.27] etc. However, until now, there are only a few publications related to the fatigue properties for AM AlSi10Mg. Ngnekoua et al. [5.28] investigated the impact of building direction and additional T6 heat treatment on the fatigue life of an AM AlSi10Mg. The authors concluded, that the building direction influenced the fatigue life significantly only in the case of the additional heat treatment. As reported by Awd et al. [5.29], the fatigue behaviour of AM AlSi10Mg parts may be influenced significantly by the material porosity, its microstructure and surface quality. The surface roughness does have a high influence on the fatigue strength, as the as-built surface of AM parts is usually highly rough. Therefore, the initiation of fatigue cracks has been observed dominantly from these micro-defects (Aboulkhair et al. [5.30], Tang et al. [5.31]). Furthermore, many of the studies have reported improved fatigue strength of the AM AlSi10Mg parts using an appropriate heat treatment, which leads to the homogenisation of the material's structure (Brandl et al. [5.32], Uzan et al. [5.33], Bagherifard et al. [5.34].

5.2.1 Material and specimen preparation

The AlSi10Mg specimens were fabricated by the DMLS-technique using the EOSINT-M-270 system [5.12]. The general process data were as follows: Minimum layer thickness 30 μm; surface roughness of as built and

cleaned specimens Ra 15–19 μm; density of the material 2.68 g/cm^3. The material composition is shown in Table 5.1.

Table 5.1: Material composition (maximum values in [%]) of DMLS AlSi10Mg alloy

Al	Si	Fe	Cu	Mn	Mg	Ni	Zn	Pb	Sn	Ti
Bal.	9.0 – 11.0	0.55	0.05	0.45	0.2 – 0.45	0.05	0.10	0.05	0.05	0.15

Flat specimens were designed directly in the shape required for the quasi-static tensile and fatigue tests. Figure 5.1*a* shows the geometry of the specimen, while the designation of building and scanning directions using DMLS technology are shown in Figure 5.1*b*. Specimens for metallography were prepared by manual grinding with SiC up to No. 1200, polishing with diamond pastes 9 μm, 3 μm and 1 μm, and etching in 0.5 % HF in water. They were examined by a light microscope (Nikon 300), and two Scanning Electron Microscopes (SEMs, Quanta 200 and Sirion 400 NC, FEI).

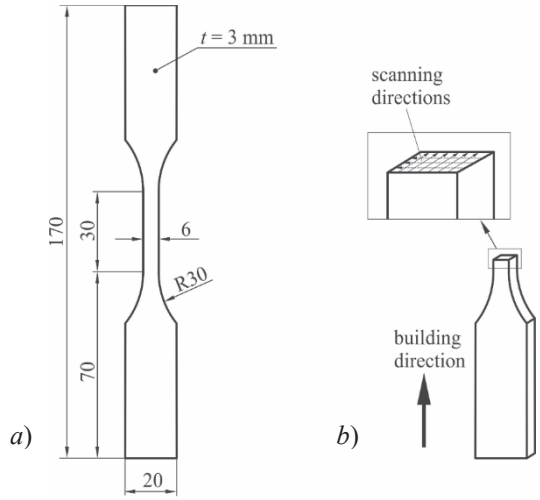

Figure 5.1: Geometry (*a*) and building direction (*b*) of a flat test specimen

5.2.2 Experimental testing

Because of the limited number of specimens, only two (specimen nos. #1 and #2) were used for static tensile tests, in order to measure the σ–ε response of the specimens and to determine the loading levels for the fatigue experiments. The tensile tests were carried out on the 100 kN MTS Landmark hydraulic machine at room temperature of 23 ºC. The tests were displacement controlled, with a loading rate of 0.5 mm/min according to the ISO 6892-1 Standard [5.36]. The force was measured with a 100 kN MTS load cell, and the strains were measured with an MTS 834.11F-24 extensometer. The average elastic modulus E, yield stress $R_{p0.2}$, ultimate tensile strength R_m and strain at rupture ε_{max} were calculated on the basis of the measured σ–ε responses. In the framework of cyclic experimental testing, eight specimens were used for the high-cycle fatigue tests. The loading was pulsating ($R = 0$), in order to avoid buckling of the specimens due to their thin cross-section. The tests were performed on the same 100 kN MTS Landmark hydraulic machine at room temperature of 23 ºC. In each fatigue test, the dynamic loading was force controlled with a constant stress amplitude σ_a (σ_a was varying between 57.0 to 79.8 MPa for eight tested fatigue specimens designated from #3 to #10).

5.2.3 Results and discussion

5.2.3.1 Microstructure investigation

Figure 5.2 shows the polished surface of specimen #1 after DMLS. The black circles represent porosity. The pores were much more frequent and also much larger near the specimen surface around the whole circumference, up to 500 μm inwards. The diameters of the largest pores were 47 ± 16 μm, and their distances to the surface were 192 ± 142 μm. These near-surface pores were formed at the beginning/end of a scan vector in the x-direction. The laser movement in the y-direction did not remove them during the formation of the subsequent layer. Some larger pores were also inside the specimens. However, their typical sizes were much smaller (10 to 20 μm), and they were visible at higher magnifications.

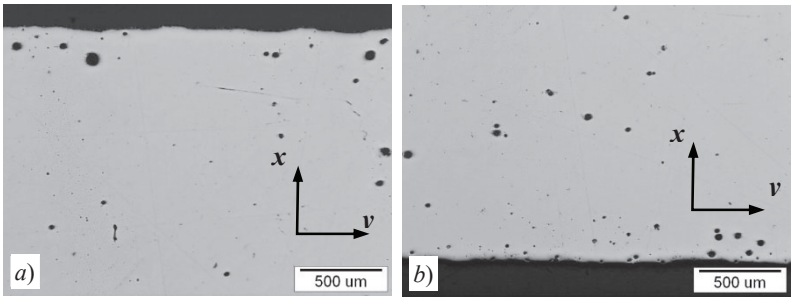

Figure 5.2: A light micrograph of the polished specimen #1 in the *x*-*y* plane showing the distribution of pores (the deposition direction *z* is perpendicular to the micrograph)
a) Top area, *b*) Bottom area

Figure 5.3 shows a light micrograph of the etched specimen #1 after DMLS. The arrows indicate subsequent layers formed by the laser beam when it scanned in the *x*-direction (perpendicular to the micrograph). The lateral movement in the next *x*-layer was opposite to the previous one. It is evident that the microstructure consists of bands, which were produced by varying the scan direction in each subsequent layer. The *y*-layers were nearly continuous in this cross-section, since the laser beam moved uniformly from the left to the right, and vice versa. The *x*-direction was perpendicular to the metallographic surface. Each laser pass caused partial remelting of the bottom *y*-layer, and a neighbouring lateral *x*-trace. Thus, the microstructure reveals the sequence of deposition clearly. The passing laser beam caused full remelting of the initial powder, and partial remelting of the bottom layer and the neighbouring trace in the same layer. Some of the previously solidified material remelted fully, and some areas were heated to the two-phase α-Al + liquid region. These two-phase regions appear brighter, and separate areas produced by each scan of the beam. In a micrograph with a higher magnification (Figure 5.3, right), the fully remelted areas consisted of dendritic cells growing in a direction opposite to the prevalent heat extraction, while the dendrites in the partly remelted zone appeared larger, since they were able to coarsen, when they were in contact with the melt. In the fully remelted areas, the β-Si particles were between the dendritic cells as individual particles (Figure 5.4*a*). The interdendritic spaces in the mushy zone were larger (1 μm), and in this region very fine coral-like eutectic β-Si was present as a part of the (α-Al + β-Si) eutectic, which is considerably smaller than in castings (Figure 5.4*b*). Some β -Si particles were present

within the dendrites. Previous studies showed that approximately 9 % Si was dissolved in the α-Al [5.37], which exceeds the maximum equilibrium solubility of Si in Al significantly.

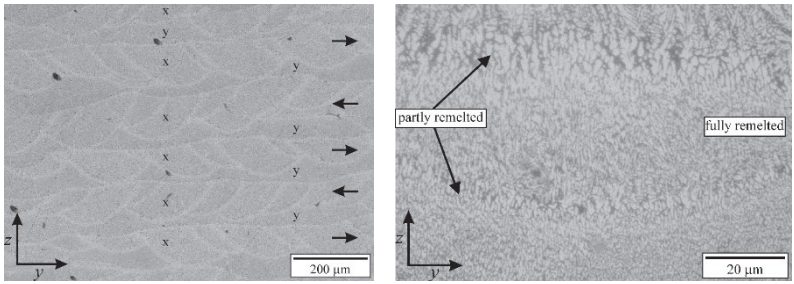

Figure 5.3: A light micrograph of the etched specimen #1 at different magnifications (the building direction was *z*)

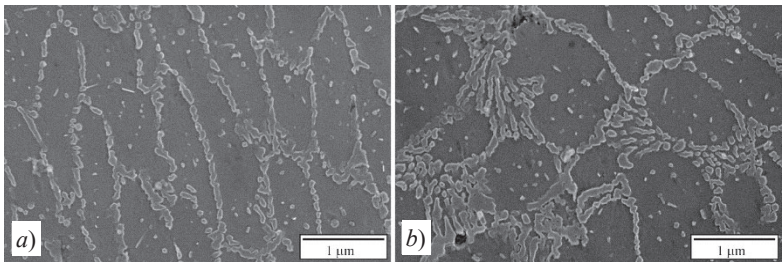

Figure 5.4: The secondary electron micrographs of the microstructure *a*) Fully remelted region, *b*) Partly remelted region

5.2.3.2 Quasi-static tests

The measured quasi-static σ–ε responses for the specimens #1 and #2 are presented in Figure 5.5. Through the whole domain the discrepancy between the two curves is less than 2 MPa. The average measured values for the typical mechanical parameters are presented in Table 5.2.

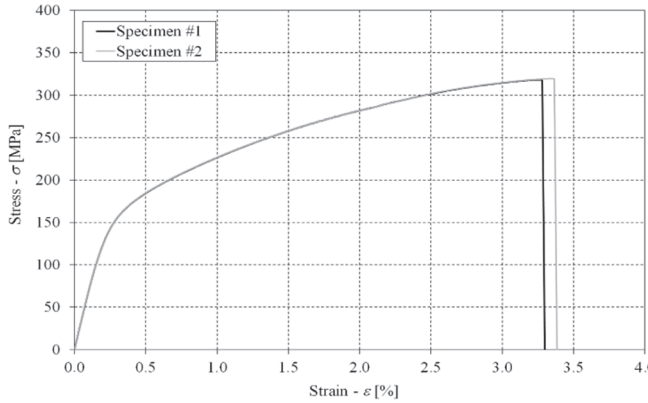

Figure 5.5: σ–ε responses from the tensile tests

Table 5.2: Average measured mechanical parameters of the DLMS AlSi10Mg alloy [5.35]

Young's modulus E [MPa]	Yield stress $R_{p0.2}$ [MPa]	Ultimate tensile strength R_m [MPa]	Strain at rupture A_5 [%]	True fracture strain ε_f [–]
70900	180	318	3.35	0.031

The already presented results obtained by the quasi-static tests served as a basis for the determination of the loading level of the further fatigue tests. Here, the highest maximum stress level of 159.6 MPa, which represents the end of the linear elastic characteristic in the σ–ε response and the smallest maximum stress of 114 MPa (approximately three times smaller than the ultimate tensile strength) was chosen for that purpose.

The fractured surfaces of both specimens were similar. Figures 5.6 and 5.7 show the fractured surface of the tensile specimen #1. The fracture probably started near the surface, at the sites where large pores were present. Despite that the contractions of the specimen were small, the fracture surface showed characteristics of a ductile fracture, with many dimples. Some dimples were 10−20 μm in diameter, others around 4−7 μm, and most of them 0.5−2 μm. Some of the largest dimples perhaps belong to the pores that were initially present in the microstructure. Smaller dimples formed during the plastic deformation. The dislocation glide can cause decohesion at the matrix-particle interface or fracture of particles, resulting in the

formation of micro-voids. The micro-voids grow and coalesce during further plastic deformation until they are torn apart.

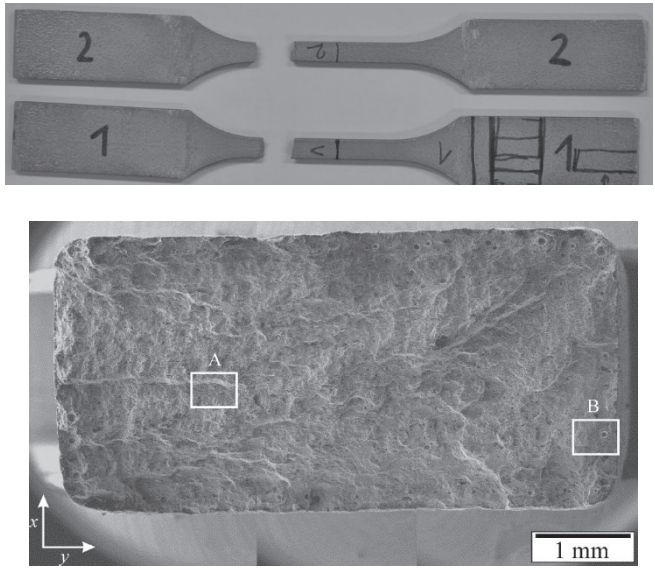

Figure 5.6: A secondary electron micrograph of the fracture surface of the specimen #1.

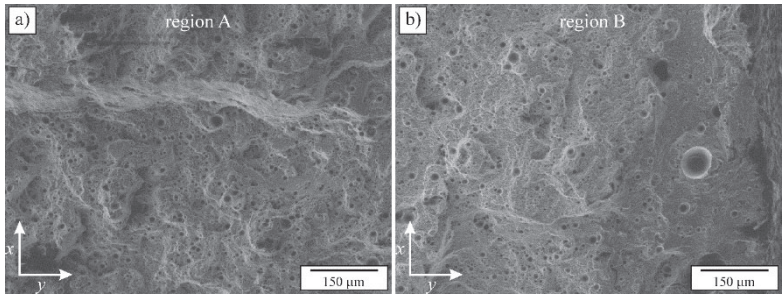

Figure 5.7: Secondary electron micrographs of the fracture surface of the specimen #1
a) at site A, *b*) at site B (see also Figure 5.6.)

5.2.3.3 Fatigue tests

Figure 5.8 shows the *S–N* curves obtained from the experimental results for eight fatigue-life experiments (specimens #3 to #10). As shown, the fatigue-life curves are presented. The fatigue-life curves for 5 %, 50 % and 95 % probabilities of fatigue failure were modelled using a conditional Weibull's probability density function [5.38]. The complete statistical evaluation of the given example is described fully in [5.35].

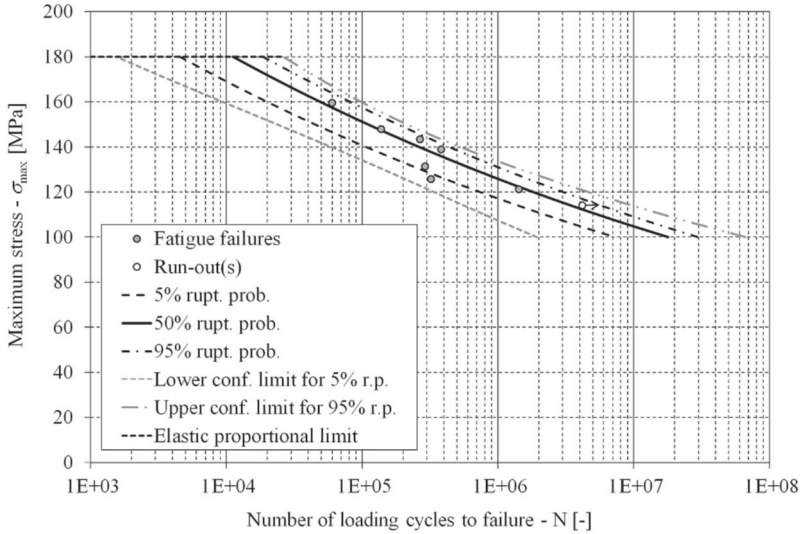

Figure 5.8: The *S-N* curve of the analysed DLMS AlSi10Mg alloy [5.35]

Figure 5.9 shows a typical fatigue fracture surface (the white arrows indicate the crack propagation direction during the stable crack growth). It can be seen that the fracture surface consists of four regions: The region of Fatigue Striations (FS) close to the surface, the region of Stable crack growth (S), the region of unstable crack propagation (I) and the region of Forced Fracture (FF).

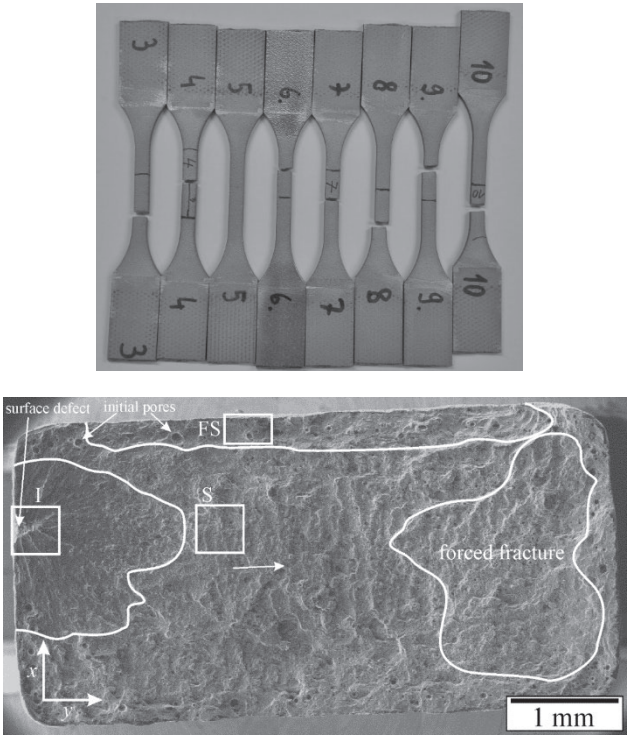

Figure 5.9: A secondary electron micrograph of the fatigue fracture surface of specimen #9.

Figure 5.10*a* shows a region between the original DLMS-surface and fracture surface. The original surface was rather rough, with many surface defects (Figure 5.10*b*). Cracks formed at several sites, and some of them grew from the surface inwards. At the beginning Fatigue Striations can be seen. They were typical features during crack growth at rather low stress intensity factor. This type of crack growth was limited to a near-surface region. As stress intensity factor increased, the stress concentration around large surfaced defects caused unstable crack propagation in all directions from those defects. In this stage of crack growth, the surface contained several flat surfaces – facets.

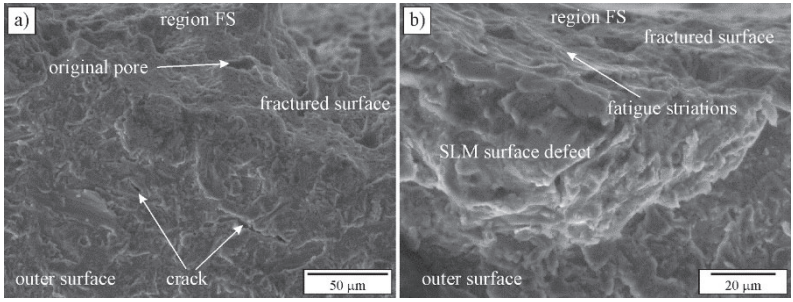

Figure 5.10: Secondary electron micrographs of the fatigue fracture of specimen #9 in the FS-region (see also Figure 5.9)
a) Cracks on the outer surface and original pores, *b*) Fatigue Striations on the fracture surface

The pores shown in Figure 5.11 were formed during the DLMS process, and not during the crack propagation. The fracture surface was not completely flat, due to a fine microstructure consisting of α-Al and β-Si. During the stable crack propagation, plastic deformation occurred at the crack tip, producing pores of different sizes (Figure 5.12). Such growth is a typical for a high stress intensity factor, when the stress is close to the alloy's yield point.

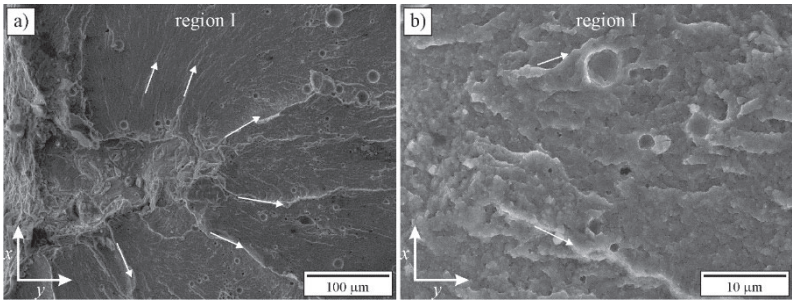

Figure 5.11: Secondary electron micrographs of the fatigue fracture of specimen #9 in region I (see also Figure 5.9)
a) Area of the crack initiation, *b*) Area of the unstable crack propagation

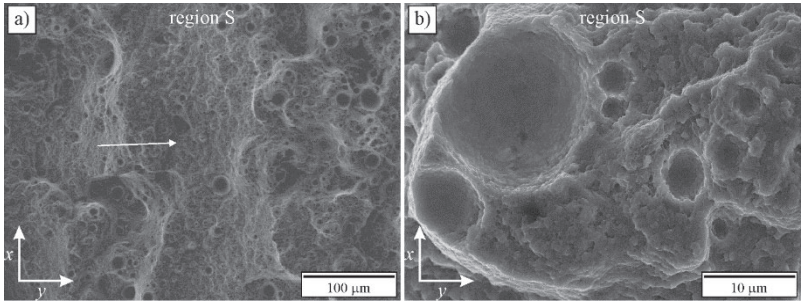

Figure 5.12: Secondary electron micrographs of the fatigue fracture of specimen #9 in region S (see also Figure 5.9)
a) Lower magnification, *b*) Higher magnification

5.2.4 Conclusions

The material characterisation of SLM AlSi10Mg alloy under quasi-static and fatigue loading is presented in this study. Flat specimens were designed directly in the shape required for the quasi-static and fatigue tests under pulsating loading in tension ($R = 0$). Based on the theoretical study, experimental testing, statistical analyses and fractography of quasi-static and fatigue specimens, the following conclusions can be made:

- The microstructure of the analysed DLMS AlSi10Mg alloy consists of bands, which were produced by varying the scan direction in each subsequent layer. The material porosity is more frequent and larger in the near surface layers, where pores were formed at the beginning/end of a scanning during the AM process.
- The material parameters obtained by quasi-static tests are comparable to the results presented from other researches. The fractography of the quasi-static specimens has shown that the fracture probably started near the surface, where large pores were present. The fracture surface showed the characteristics of a tough fracture (many dimples appeared due to the local plastic deformation during the quasi-static crack propagation).
- The results of the fatigue tests have shown that the confidence interval of the obtained fatigue-life curves is relatively high, which is a consequence of the relatively small number of tested specimens. The fractography of fatigue specimens have shown that the fatigue

cracks initiated around the surface defects, produced by DLMS and then propagated in an unstable manner.

5.3 Computational fatigue analysis of auxetic cellular structures made of DMLS AlSi10Mg Alloy

Typical lightweight structures, where AM AlSi10Mg alloy may also be used, are advanced cellular metamaterials and structures, which are difficult to fabricate by traditional processes [5.39, 5.40]. The advantages of using AM technologies are focused mainly on the predefined cell topology and morphology to manufacture designed-to-purpose structures [5.41]. With the proper choice of optimal geometrical properties and predesigned skeleton of cellular structures, it is possible to develop new advanced multifunctional materials and structures with superior mechanical and thermal properties. For example, auxetic cellular structures [5.42], which exhibit unique mechanical properties due to a negative Poisson's ratio (e.g. re-entrant, chiral and rotating-square structures, two-dimensional structures with a rectangular strut cross-section), will in future be fabricated from AM Al based alloys for green lightweight design. Thus, it is, especially for structural applications (e.g. engineering, medicine), important to determine the fatigue behavior of cellular structures precisely [5.43, 5.44] and the materials they are made of. In recent years, the research work regarding AM-cellular structures has been focusing on the mechanical response of the gradient lattice structures manufactured via the DMLS or SLM-process in terms of energy absorption under the compressive loading conditions [5.45–5.47]. Some authors have also investigated the fatigue behaviour of different SLM-lattice structures considering the effect of the cellular topology and geometrical imperfections on the fatigue life of the analysed structures [5.48–5.50]. The next group of metamaterials suitable to be produced using the AM-technology are the auxetic cellular structures, which are the subject of this study.

The presented study is focused on the fatigue behaviour of five different auxetic cellular structures obtained by the topology optimisation, and made of the DMLS AlSi10Mg alloy already described in Section 5.2. The fatigue life of different auxetic cellular geometries with different fillet radiuses is determined by the strain-life approach using the Universal Slope method. The needed material parameters were determined according to the experimental results previously obtained by the unidirectional tests (see Section 5.2). Numerical nonlinear finite element simulations were performed to determine the deformation behaviour and the stress and strain fields in

the critical cross-sections of the analysed cellular structures. Then, the numerical results were used as the input parameters in the subsequent fatigue analyses.

5.3.1 Auxetic cellular structures

The auxetic cellular structures exhibit a negative Poisson's ratio and, thus, experience large volume changes under loading [5.51–5.53]. The auxetic structures tend to expand in the lateral direction when subjected to the uni-axial tensile loading, and vice versa in the case of the compressive loading (Figure 5.13). During the external loading of a given auxetic geometry, their cell shape changes rapidly through the complete auxetic structure, thus the loading spreads efficiently through the whole structure. With recent advances in the AM technologies, it is possible to fabricate the auxetic cellular structures with optimised and exactly predefined geometries (i.e. strut thickness, geometry, cell shape and size). Design and optimisation of auxetic structures can be done by using advanced Computer Aided Engineering (CAE) methodologies to achieve and control the desired mechanical properties for specific applications [5.54]. Such precise fabrication control of the shape, size and distribution of cells with the use of layered Additive Technologies makes the auxetic structures superior to the other conventionally manufactured cellular materials.

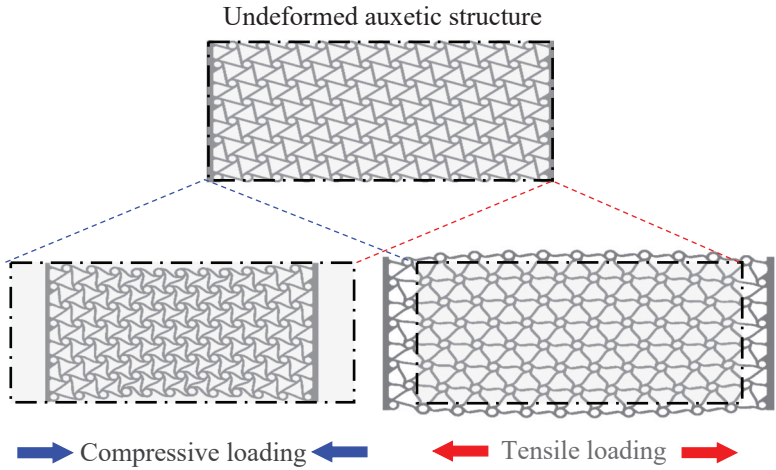

Figure 5.13: The principle of the deformation behaviour of a chiral auxetic cellular structure

Many auxetic cellular structures have been developed to-date. Their shape, topology and dimensions were usually custom-made for the task they were designed for. Therefore, it is difficult to compare their fatigue properties between them. In the previous study by Borovinšek et al. [5.54], a procedure for the determination of optimal auxetic topology was developed using a numerical approach. The performance of the auxetic structure was regarded as a performance of the compliant mechanism and, as such, two objective functions related to the stiffness and flexibility were applied to determine the optimal topologies. A set of the best topologies (the Pareto front) was obtained using two objective functions and a multi-objective optimisation procedure. All solutions on the Pareto front are optimal and equally good. Thus, applying this procedure results in a set of topologies which have an auxetic behaviour. Since they are optimised with the same procedure and with the same objectives, it is also possible to compare their fatigue behaviour directly. The drawback of this procedure is that the resulting optimal topologies of the quarter cell models are sharp-edged, since their topology consists of square-shaped parameter regions (Figure 5.14*a*). The sharp edges of the structure result in stress concentrations under load, and do not allow a direct application of the obtained topologies. For this reason, the following smoothing procedure was applied, to reduce the number of possible stress concentration regions. The medial axis of the obtained topology was determined first (Figure 5.14*b*). The existing vertical and horizontal parts retained their thickness, while a new thickness was prescribed to the topology parts obtained from the medial axis. The thickness of these parts was set to such a value that the topology area remained the same. In the last procedure step, all remaining sharp corners were rounded using an equal fillet radius R (Figure 5.14*c*).

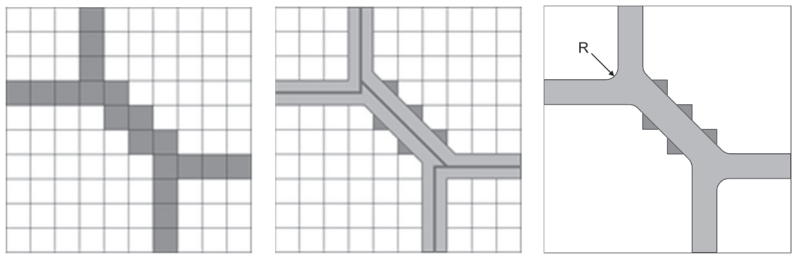

Figure 5.14: Base topology (*a*), medial axis topology (*b*) and rounded medial axis topology (*c*)

From the Pareto front, five base topologies were selected for this study. The topologies of the Pareto front were first sorted by their Poisson's ratio starting with the lowest one (Topology 1), the median one (Topology 3) till the highest one (Topology 5). An additional two topologies were selected between the lowest and the median Poisson's ratio (Topology 2) and between the median and the highest Poisson's ratio (Topology 4). The Poisson's ratio and the mass of all five base topologies are reported in Table 3. After selection, the smoothing procedure was applied, which resulted in five distinct quarter unit cell topologies (Figure 5.15).

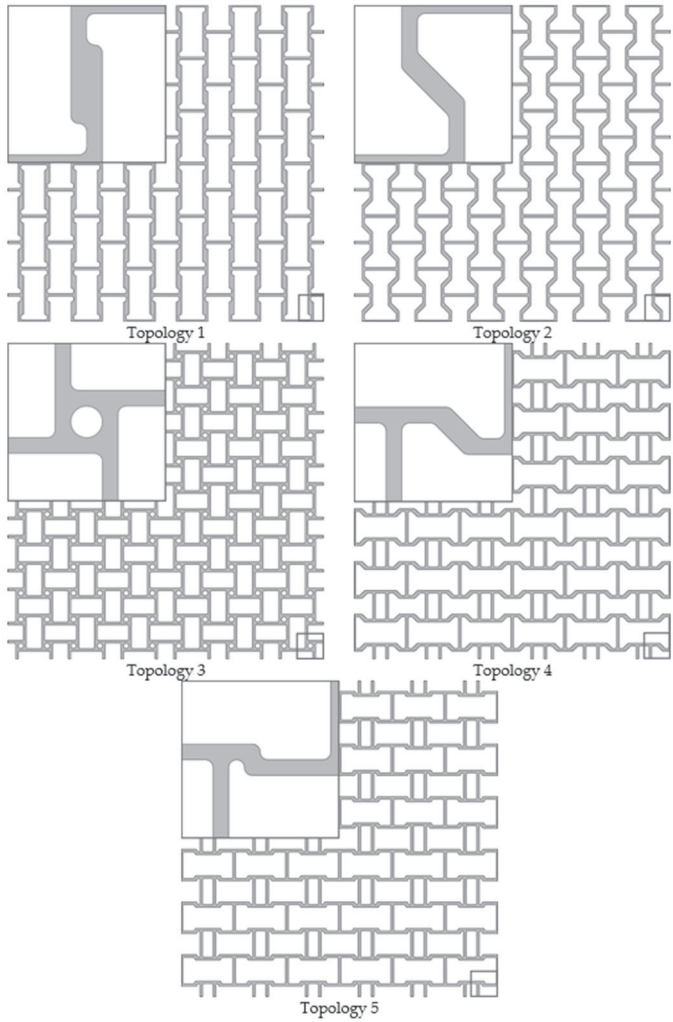

Figure 5.15: Selected quarter unit cell topologies and resulting auxetic structures [5.55]

5.3.2 Computational analyses

The material used in this study was the DMLS AlSi10Mg alloy already described in Section 5.2 (see material parameters see in Table 5.2).

The numerical models of five auxetic structures were built in Ansys Mechanical [5.56], using a 2D plane stress formulation. The size of 10 mm x 10 mm was chosen for the one-unit cell, which results in a structure size of 60 mm x 60 mm and nominal strut thickness of 0.5 mm. The finite element mesh consisted of plane stress parabolic quad finite elements with 8 nodes, and, in some cases, plane stress triangular finite elements with 6 nodes. With the parametrical analysis, it was deduced that the results converged using a mesh where the global element size was approx. 0.2 mm, with consideration of curvatures, where the element size was even smaller. This resulted in numerical models with an average of 30,000 finite elements and 100,000 nodes. Each topology was constrained in the y-direction at the bottom and loaded with displacement at the top. All five structures were loaded with the same displacement of 0.4 mm in the +y-direction, thus creating a tension in the vertical direction. The models were constrained in the x-direction in the middle of the structure to prevent horizontal movement (see Figure 5.16). The models were loaded with the displacement, which caused plastic deformation in all five models. Therefore, material nonlinearity was considered in the simulations. For plasticity, a multilinear isotropic hardening model was used, with the utilisation of the true stress-strain material data previously obtained from tensile tests (see Section 5.2).

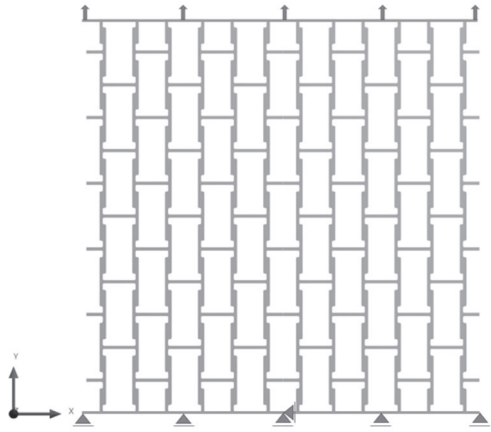

Figure 5.16: Boundary conditions

Numerical results in the form of total displacements are presented in Figure 5.17. Resulting displacement was scaled by the factor 11 for all structures. It can be noted that they have different Poisson's ratios.

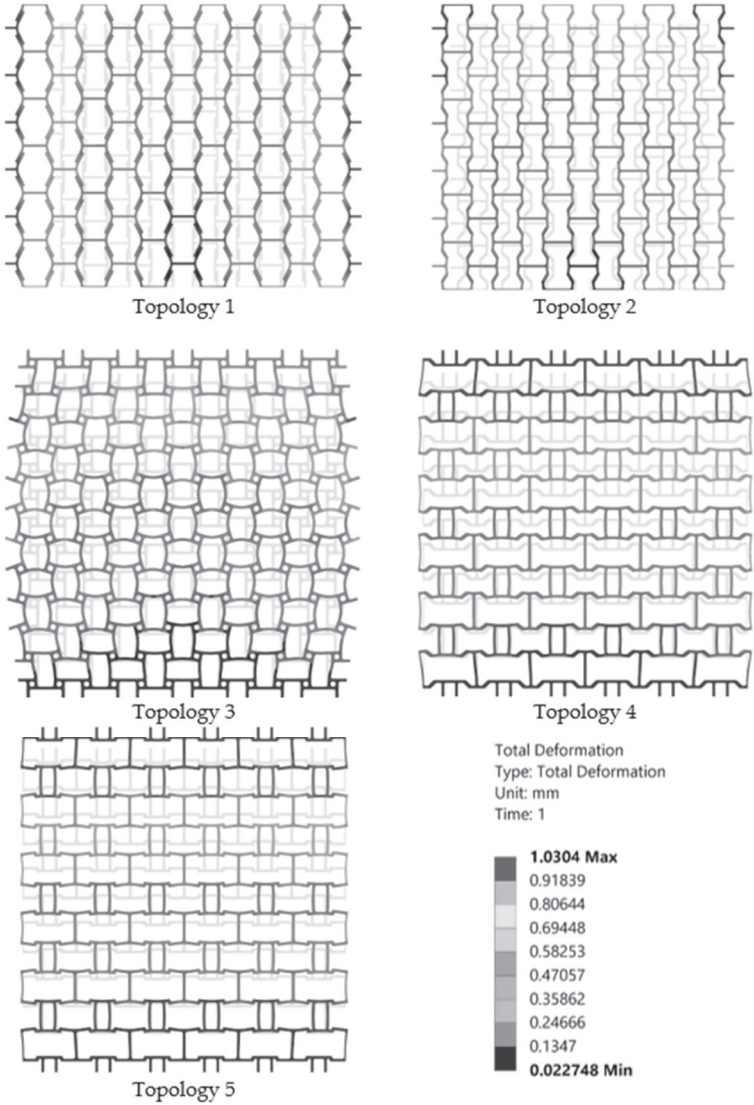

Figure 5.17: Deformed and undeformed analysed structures

Poisson's ratios were calculated as the ratio between the longitudinal and lateral displacement. The calculated Poisson's ratios and other results are given in Table 5.3. The Poisson's ratios of the analysed structures are to some extent different than the unit cell's Poisson's ratio. All calculated Poisson's ratios are negative, which proves that all analysed structures are also auxetic. It can be seen that Topology 1 has the lowest Poisson's ratio, while Topology 5 has the highest Poisson's ratio. The Poisson's ratio of the other three topologies is ascending between Topology 1 and Topology 5. Table 5.3 also reports the mass of each model, showing that all structures have a similar weight. Only Topology 3 is a bit more massive.

Table 5.3: Properties and results of the analysed topologies [5.35]

Topology	Mass [g]	Displacement *x*-direction [mm]	Equivalent el. strain [–]	Equivalent pl. strain [–]	Poisson's ratio [–]	Unit cell ratio [–]
1	0.10	0.964	0.00408	0.0154	–2.41	–4.01
2	0.09	0.381	0.00307	0.0180	–0.95	–2.71
3	0.12	0.280	0.00362	0.0094	–0.67	–0.92
4	0.10	0.080	0.00312	0.0022	–0.20	–0.35
5	0.09	0.040	0.00323	0.0011	–0.01	–0.19

Figure 5.18 shows the location of the maximum plastic strain. The area of the maximum plastic strain is also magnified to visualise the exact location of the developed plastic zones. The location of the maximum plastic strain in all cases is at the fillet radius of the auxetic structure.

Since the size of the radius is important, a series of parametric analyses were conducted with different radius sizes. Radiuses were scaled in a range of 0.1 mm and 0.9 mm with a step of 0.1 mm. Figure 4.15 shows the basic topology designs from which the numerical models were built. Most of the structures allow a wide range of radiuses, while Topology 1 and Topology 5 are limited because two fillets intersect and prevent further radius scaling. Therefore, some radiuses were scaled, while the potentially intersecting radiuses were presented only up to the maximum possible values, e.g. Topologies 1 and 5. Each time the radius was scaled, the numerical model was regenerated with the same mesh parameters and the same boundary conditions as presented in Figure 5.16. In that way, it was possible to determine how radius sensitive the analysed structures were and what the optimal radius for each structure was in terms of fatigue.

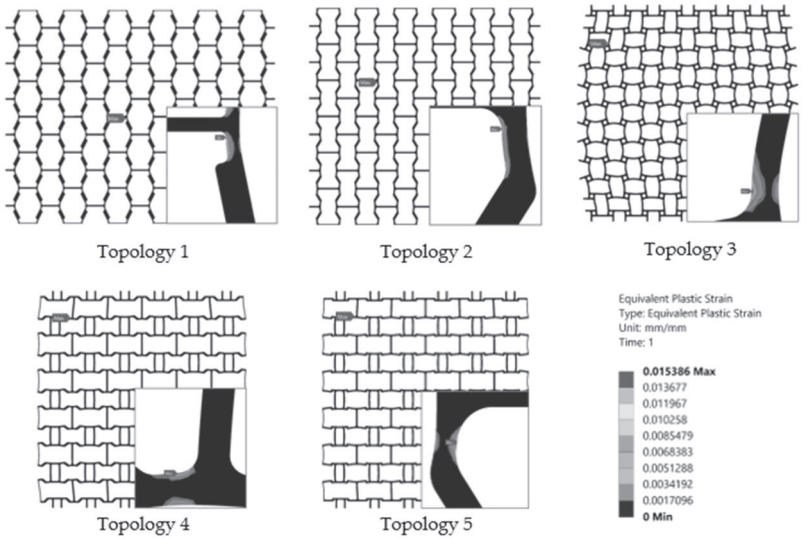

Figure 5.18: Location of the maximum equivalent plastic strain

Figure 5.19 shows the equivalent plastic strain for different fillet radiuses. From the results in Figure 5.19, it is clear that, at small fillet radius, the plastic strain occurs near the edge, which is placed, where the crack initialisation is expected. With a larger fillet radius, the area of the plastic zone is wider, and the value of the equivalent plastic strain is lower in all structures. In most of the observed structures, this occurs at the radius of approx. 0.4 mm, with exceptions in Topology 1 (at the radius of approx. 0.2 mm) and Topology 4 (at the radius of approx. 0.3 mm). The value of the equivalent plastic strain increased with further increase of the fillet radius. Furthermore, some new critical areas occurred. Accordingly, large fillet radiuses create new critical places for the crack initiation, where sometimes the equivalent plastic strain has the same or larger value than observed in the case of very small fillet radiuses.

The obtained numerical results were then used for fatigue life determination. From each numerical result, the maximum equivalent elastic strain was added to the maximum equivalent plastic strain. This allows the calculation of the fatigue life cycle for each topology including the fillet radius variations. Additional numerical analysis was performed for each structure, to determine the yield load condition when the structure behaves purely elastically and therefore has an infinite fatigue life.

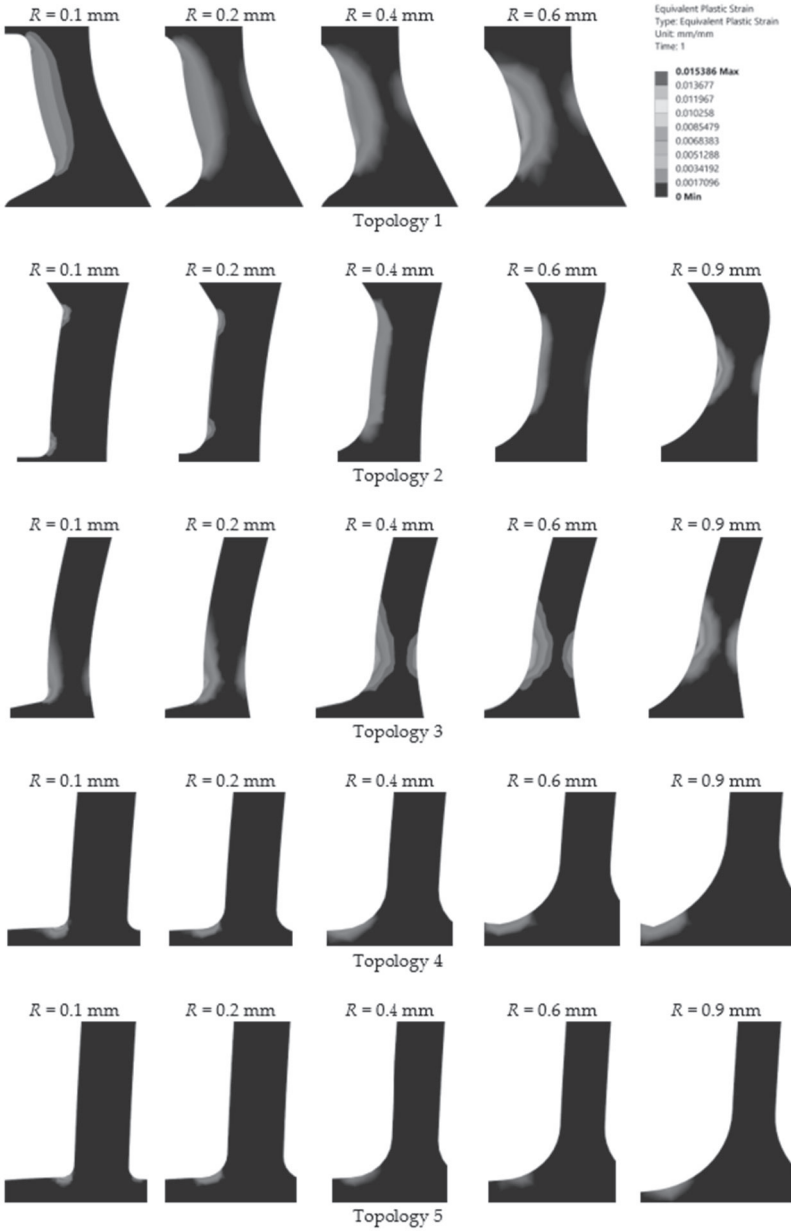

Figure 5.19: Equivalent plastic strain for different fillet radiuses [5.55]

5.3.3 Fatigue life determination

In the presented study, the strain-life approach is used to determine the fatigue life of the analysed auxetic structures. In general, this approach is based on the knowledge of the stresses and strains that occur at locations, where the fatigue crack nucleation is likely to start, e.g. holes, fillets, grooves. In this approach, the fatigue behaviour of the material is described by the strain-life curve expressed by the Coffin-Manson relation between fatigue life N_i and the total amplitude strain ε_a (see Section 2.2). However, the material low-cycle fatigue parameters should be determined previously using the appropriate low-cycle fatigue test. If it is not the case, an alternative method can be used, based on the material parameters obtained from a quasi-static test. In this study, the method of Universal Slopes as proposed by Muralidharan and Manson [5.57] was used to obtain the number of loading cycles N_i required for the fatigue crack initiation in the critical cross-section of the analysed auxetic structures:

$$\varepsilon_{aE} = 0.623\left(\frac{R_m}{E}\right)^{0.832}(2N_i)^{-0.09} + 0.0196\cdot{\varepsilon_f}^{0.155}\left(\frac{R_m}{E}\right)^{-0.53}(2N_i)^{-0.56} \quad (5.1)$$

where ε_{aE} is the equivalent strain amplitude, E is the Young's modulus, R_m is the ultimate tensile strength and ε_f is the true fracture strain. Once the equivalent strain amplitude, ε_{aE}, is known, the number of stress cycles N_i can be obtained iteratively from Eq. (5.1) and with consideration of the material parameters E, R_m and ε_f given in Table 5.2.

In the presented study, the sum of the equivalent elastic and plastic strain was considered as the equivalent strain amplitude, ε_{aE}, which enabled the calculation of the fatigue life from Eq. (5.1). Figure 5.20 shows the calculated fatigue life based on the numerical results with models using different fillet radiuses. For Topology 1, the expected fatigue life cycles are rather low, with a maximum value at the fillet radius of 0.2 mm. Topology 4 resulted in the best fatigue life expectance with a fillet radius of 0.3 mm. All other structures have the highest number of cycles with a radius of 0.4 mm, while the life expectancy of Topology 3 is very low. The best fatigue life is expected for Topology 5, which also has the highest Poisson's ratio making it the least auxetic structure presented in this study. On the other hand, Topology 2 has the second-highest fatigue life expectancy, while having the second-lowest Poisson's ratio. Therefore, Topology 2 could be used in cases, where a highly auxetic and durable structure is needed. It is clearly evident that the fillet radius has a significant impact on the fatigue life of the analysed auxetic cellular structures.

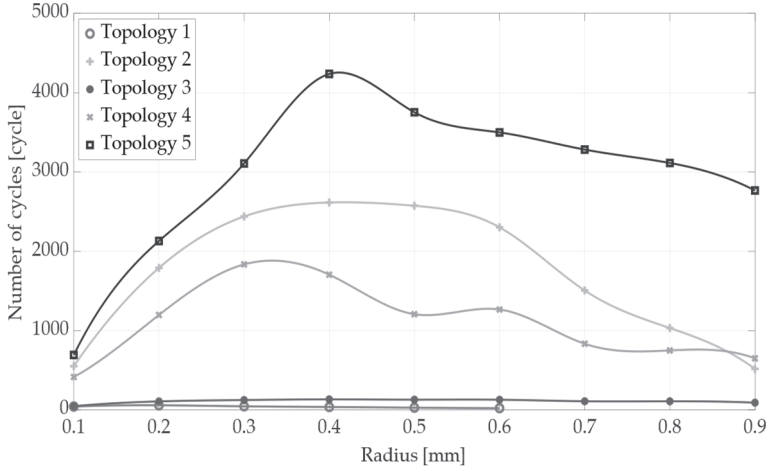

Figure 5.20: The fatigue life of different topologies and fillet radiuses

5.3.4 Conclusions

The fatigue behaviour of auxetic cellular structures obtained by multi-objective topology optimisation and made of DLMS AlSi10Mg alloy, is presented in this study. Five structures with different Poisson's ratios were considered for the parametric computational analysis, where the fillet radius of cellular struts was chosen as a parameter. All five topologies were subjected to the same tensile loading conditions. The amount of the tensile load was high enough to cause plasticity in every topology, but small enough that each topology would sustain several loading cycles until failure. The fatigue life of the analysed structures was determined by the strain-life approach using the Universal Slope method, where the needed material parameters were determined according to the experimental results obtained by the quasi-static unidirectional tensile tests. Based on the fractography of the quasi-static specimens, comprehensive numerical modelling of auxetic cellular structures, numerical simulations and fatigue analyses, the following conclusions can be made:

- The microstructure of the analysed DMLS AlSi10Mg alloy consists of bands, which were produced by varying the scan direction in each subsequent layer. The material porosity is more frequent and larger

in the near-surface layers, where pores were formed at the beginning/end of scanning during the DMLS process.

- The material parameters obtained by the quasi-static tests (Youngs modulus, yield stress, ultimate tensile strength, strain at rupture) are comparable to the results presented by the other researches.
- The obtained computational results have shown that less auxetic structures (higher Poisson's ratio) tend to have a better fatigue life expectancy (the longest fatigue life was obtained for the structure topology with the minimum auxetic characteristic).
- The fillet radius of cellular struts has a significant impact on the fatigue life. Computational analyses have shown that the fatigue life decreases for smaller fillet radiuses (less than 0.3 mm) as a consequence of high-stress concentrations, and also for larger fillet radiuses (more than 0.6 mm) due to the movement of the plastic zone away from the edge of the cell connections.
- The obtained computational results provide a basis for further investigation, including experimental testing of the fabricated auxetic cellular structures made of DLMS AlSi10Mg alloy under the cyclic loading conditions.

References

[5.1] Daniewicz S.R., Shamsaei N., An introduction to the fatigue and fracture behavior of additive manufactured parts, *International Journal of Fatigue*, 94, 2017, 167–167.

[5.2] Zhang Q., Liang Z., Cao M., Liu Z., Zhang A., Lu B., Microstructure and mechanical properties of Ti6Al4V alloy prepared by selective laser melting combined with precision forging, *Transactions of Nonferrous Metals Society of China*, 27, 2017, 1036–1042.

[5.3] Kieback B., Neubrand A., Riedel H., Processing techniques for functionally graded materials, *Materials Science and Engineering: A*, 362, 2003, 81–106.

[5.4] Simar A., Godet S., Watkons T.R., Highlights of the special issue on metal AM, *Materials Characterization*, 143, 2018, 1–4.

[5.5] Herzog D., Seyda V., Wycisk E., Emmelmann C. Additive manufacturing of metals, *Acta Materialia*, 117, 2016, 371–392.

[5.6] Gorny B., Niendorf T., Lackmann J., Thoene M., Troester T., Maier H.J., In situ characterization of the deformation and failure behaviour of non-stochastic porous structures processed by SLM, *Materials Science and Engineering: A*, 528, 2011, 7962–7967.

[5.7] Yan C., Hao L., Hussein A., Raymont D., Evaluations of cellular lattice structures manufactured using SLM, *International Journal of Machine Tools and Manufacture*, 62, 2012, 32–38.
[5.8] Murr L.E., Gaytan S.M., Medina F., Martinez E., Martinez J.L., Hernandez D.H., Machado B.I., Ramirez D.A., Wicker R.B., Characterization of Ti–6Al–4V open cellular foams fabricated by additive manufacturing using electron beam melting, *Materials Science and Engineering: A*, 527, 2010, 1861–1868.
[5.9] Yan C., Hao L., Hussein A., Young P., Huang J., Zhu W., Microstructure and mechanical properties of aluminium alloy cellular lattice structures manufactured by DMLS, *Materials Science and Engineering: A*, 628, 2015, 238–246.
[5.10] Ismaeel A., Wang C.S. Effect of Nb additions on microstructure and properties of γ-TiAl based alloys fabricated by SLM, Transactions of Nonferrous Metals Society of China, 29, 2019, 1007–1016.
[5.11] Bagherifard S., Beretta N., Monti S., Riccio M., Bandini M., Guagliano M., On the fatigue strength enhancement of additive manufactured AlSi10Mg parts by mechanical and thermal post-processing, *Materials and Design*, 145, 2018, 28–41.
[5.12] *EOS* (Electro Optical Systems), https://www.eos.info/en/about-us
[5.13] Wycisk E., Solbach A., Siddique S., Herzog D., Walther F., Emmelmann C., Effects of defects in laser additive manufactured Ti-6Al-4V on fatigue properties. *Phys. Proc.*, 56, 2014, 371–378.
[5.14] Beevers E., Brandão A.D., Gumpinger J., Gschweitl M., Seyfert C., Hofbauer P., Rohr T., Ghidini T., Fatigue properties and material characteristics of AM AlSi10Mg, *International Journal of Fatigue*, 117, 2018, 148–162.
[5.15] Maconachie T., Leary M., Lozanovski B., Zhang X., Qian M., Faruque O., Brandt M., Selective Laser Melting lattice structures: Properties, performance, applications and challenges, *Materials and Design*, 183, 2019, 108137.
[5.16] Siddique S., Muhammad I., Wycisk E., Emmelmann C., Walther F., Influence of process-induced microstructure and imperfections on mechanical properties of AlSi12 processed by selective laser melting, *J. Mater. Proc. Tech*., 221, 2015, 205–213.
[5.17] Zhang C., Zhu H., Liao H., Cheng Y., Hu Z., Zeng X., Effect of heat treatments on fatigue property of selective laser melting AlSi10Mg, *Int. J. Fatigue*, 94, 2017, 192–201.
[5.18] Tang M., Pistorius P.C., Oxides, porosity and fatigue performance of AlSi10Mg parts produced by selective laser melting, *Int. J. Fatigue*, 116, 2018, 513–522.

[5.19] Weingarten C., Buchbinder D., Pirch N., Meiners W., Wissenbach K., Poprawe R., Formation and reduction of hydrogen porosity during selective laser melting of AlSi10Mg, *Journal of Materials Processing Technology*, 221, 2015, 112–20.
[5.20] Read N., Wang W., Essa K., Attallah M.M., Selective laser melting of AlSi10Mg alloy: Process optimisation and mechanical properties development, *Materials & Design*, 65, 2015, 417–24.
[5.21] Olakanmi E.O., Cochrane R.F., Dalgarno K.W., A review on selective laser sintering/melting (SLS/SLM) of aluminium alloy powders: processing, microstructure, and properties. *Prog Mater Sci*, 74, 2015, 401–407.
[5.22] Boschetto A., Bottini L., Veniali F., Roughness modeling of AlSi10Mg parts fabricated by selective laser melting. *J Mater Process Technol*, 241, 2017, 154–63.
[5.23] Calignano F., Manfredi D., Ambrosio E.P., Iuliano L., Fino P., Influence of process parameters on surface roughness of Al-parts produced by DMLS, *Int J Adv Manuf Technol*, 67, 2013, 2743–2751.
[5.24] Thijs L., Kempen K., Kruth J.P., Van Humbeeck J., Fine-structured aluminium products with controllable texture by SLM of pre-alloyed AlSi10Mg powder, *Acta Mater*, 61, 2013, 1809–1819.
[5.25] Rosenthal I., Stern A., Frage N., Microstructure and mechanical properties of AlSi10Mg parts produced by the laser beam AM technology. *Metallogr Microstruct Anal*, 3, 2014, 448–453.
[5.26] Tuck C., Aboulkhair N.T., Maskery I., Ashcroft I., Everitt N.M., On the formation of AlSi10Mg single tracks and layers in selective laser melting: microstructure and nano-mechanical properties. *J Mater Process Tech*, 230, 2016, 88–98.
[5.27] Manfredi D., Calignano F., Krishnan M., Canali R., Ambrosio E.P., Atzeni E., From powders to dense metal parts: Characterization of a commercial AlSiMg alloy processed through DMLS, *Materials*, 6, 2013, 856–869.
[5.28] Ngnekoua J.N.D., Nadot Y., Henaff G., Nicolai J., Kan W.H., Cairney J.M., Ridosz L., Fatigue properties of AlSi10Mg produced by AM. *Int. J. Fatigue*, 119, 2019, 160–172
[5.29] Awd M., Siddique S., Johannsen J., Emmelmann C., Walther F., Very HCF properties and microstructural damage mechanisms of SLM AlSi10Mg alloy. *Int. J. Fatigue*, 124, 2019, 55–69.
[5.30] Aboulkhair T., Maskery I., Tuck C., Shcroft I.A., Everitt N., Improving the fatigue behaviour of a Selective Laser Mel aluminium alloy: Influence of heat treatment and surface quality, *Materials & Design*, 104, 2016, 174–82.

[5.31] Tang M., Pistorius C., Oxides, porosity and fatigue performance of AlSi10Mg parts produced by Selective Laser Melting, *Int J Fatigue*, 94, 2017, 192–201.
[5.32] Brandl E., Heckenberger U., Holzinger V., Buchbinder D., Additive manufactured AlSi10Mg samples using selective laser melting (SLM): microstructure, high cycle fatigue, and fracture behaviour. Materials & Design, 34, 2012, 159–69.
[5.33] Uzan N., Ramati S., Shneck R., Nachum F., Yeheskel O., On the effect of shot-peening on fatigue resistance of AlSi10Mg specimens fabricated by additive manufacturing using selective laser melting (AM-SLM), *Additive Manufacturing*, 21, 2018, 458–64.
[5.34] Bagherifard S., Beretta N., Monti S., Riccio M., Bandini M., Guagliano M., On the fatigue strength enhancement of additively manufactured AlSi10Mg parts by mechanical and thermal post-processing, *Materials & Design*, 145, 2018, 28–41.
[5.35] Glodež S., Klemenc J., Zupanič F., Vesenjak M., High-cycle fatigue and fracture behaviours of Selective Laser Melting AlSi10Mg alloy, *Transactions of Nonferrous Metals Society of China*, 30, 2020, 2577–2589.
[5.36] ISO 6892-1, *Metallic materials, Tensile testing - Part 1: Method of test at room temperature*, ISO standard, 2019.
[5.37] Li W., Li S., Zhang A., Zhiu Y., Wei Q., Yan C., Shi Y., Effect of heat treatment on AlSi10Mg alloy fabricated by selective laser melting: Microstructure evolution, mechanical properties and fracture mechanism. *Materials Science and Engineering A*, 663, 2016, 116–125.
[5.38] Klemenc J., Influence of fatigue–life data modelling on the estimated reliability of a structure subjected to a constant-amplitude loading, *Reliability Engineering and System Safety*, 142, 2015, 238–247.
[5.39] Wei P., Wei Z., Chen Z., Du J., He Y., Li J., Zhou Y., The AlSi10Mg samples produced by selective laser melting: single track, densification, microstructure and mechanical behaviour, *Appl. Surf. Sci.*, 408, 2017: 38–50.
[5.40] Takata N., Kodaira H., Suzuki A., Kobashi M., Size dependence of microstructure of AlSi10Mg alloy fabricated by selective laser melting, *Materials Characterization*, 143, 2018, 18–26.
[5.41] Lehmhus D., Vesenjak M., Schampheleire S.D., Fiedler T., From Stochastic Foam to Designed Structure: Balancing Cost and Performance of Cellular Metals, *Materials*, 10, 2017, 1–32.

[5.42] Novak N., Vesenjak M., Ren Z., Auxetic Cellular Materials – a Review, *Strojniški vestnik - Journal of Mechanical Engineering*, 62, 2016, 485–493.
[5.43] Tomažinčič D., Nečemer B., Vesenjak M., Klemenc J., Low-cycle fatigue life of thin-plate auxetic cellular structures made from aluminium alloy 7075-T651, *FFEMS*, 42, 2019, 1022–1036.
[5.44] Nečemer B., Vesenjak M., Glodež S., Fatigue of Cellular Materials – a Review, *Strojniški vestnik - Journal of Mechanical Engineering*, 65, 2019, 525–536.
[5.45] Sienkiewicz J., Płatek P., Jiang F., Sun X., Rusinek A., Investigations on the Mechanical Response of Gradient Lattice Structures Manufactured via Selective Laser Melting, *Metals*, 10, 2020, 213.
[5.46] Maconachie T., Leary M., Lozanovski B., Zhang X., Qian M., Faruque O., Brandt M., Selective Laser Melting lattice structures: Properties, performance, applications and challenges, *Materials & Design*, 183 2019, 108137.
[5.47] Xiao L., Song W., Wang C., Liu H., Tang H., Wang J., Mechanical behaviour of open-cell rhombic dodecahedron Ti-6Al-4V lattice structure, *Mater. Sci. Eng. A*, 640, 2015, 375–384.
[5.48] Boniotti L., Beretta S., Patriarca L., Rigoni L., Foletti S., Experimental and numerical investigation on compressive fatigue strength of lattice structures of AlSi7Mg manufactured by Selective Laser Melting, *International Journal of Fatigue*, 128, 2019, 105181.
[5.49] Dallago M., Winiarski B., Zanini F., Carmignato S., Benedetti M., On the effect of geometrical imperfections and defects on the fatigue strength of cellular lattice structures additively manufactured via SLM, *International Journal of Fatigue*, 124, 2019, 348–360.
[5.50] Zargarian A., Esfahanian M., Dadkhodapouor J., Ziaei-Rad S., Zamani D., On the fatigue behaviour of AM lattice structures, *Theoretical and Applied Fracture Mechanics*, 100, 2019, 225–232.
[5.51] Lim T.C., *Auxetic materials and structures*; Springer, 2015.
[5.52] Lakes R.S., Foam structures with a negative Poisson's ratio, *Science*, 235, 1987, 1038–1040.
[5.53] Salit V., Weller T., On the feasibility of introducing auxetic behaviour into thin-walled structures, *Acta Materialia*, 57, 2009, 125–135.
[5.54] Borovinšek M., Novak N., Vesenjak M., Ren Z., Ulbin M., Designing 2D Auxetic Structures Using Multi-Objective Topology Optimization, *Mater. Sci. Eng. A*, 795, 2020, 139914.

[5.55] Ulbin M., Borovinšek M., Vesenjak M. Glodež S., Computational fatigue analysis of auxetic cellular structures made of SLM AlSi10Mg alloy, *Metals*, 10, 2020, 1–18.
[5.56] Ansys® Academic Research Mechanical, Release 2020 R1.
[5.57] Muralidharan U., Manson S.S., Modified Universal Slopes Equation for Estimation of Fatigue Characteristics, *Trans. ASME- J. Eng. Mater. Tech*., 110, 1988, 55–58.

CHAPTER 6

BENDING FATIGUE OF SINTERED GEARS

6.1 Introduction

As discussed in Chapter 1, Powder Metallurgy (P/M) is useful in making parts that have irregular curves (i.e. sintered gears). Sintered gears have initially been used only for light duty applications such as toys and power tools. Today, powder metal gears are a cost efficient alternative for machined gears in larger series in the Automotive industry (synchroniser gears, oil pump gears, engine gears, etc.). The next step should be power transmission gears [6.1].

A critical review regarding P/M-sintered gears' application for transmissions and machinery has been presented by Dizdar [6.2]. The idea of sintered gears dates back to 1985, when researchers in the Soviet Union investigated the tooth strength of sintered planetary pinions for automobile differentials [6.3]. However, due to low Young`s modulus and low surface hardness, which led to significant wear, the usage of sintered gears was limited to low load applications. Investigations of RCF (Rolling Contact Fatigue) on sintered steel led to the selective surface densification of gear flanks, which improved the surface hardness and, therefore, reduced wear [6.4–6.8]. However, surface densification of gear flanks is done after sintering, and thus causes an additional procedure, which raises the cost of the final product, and, consequently, the reducing economic advantage over conventional gear production with milling. Recent development in powder metallurgy production technology increased the strength of final PM-products to an again interesting level for sintered gears applications without additional procedures [6.9, 6.10].

This study is focused on the fatigue failures of sintered gears. Although two kinds of fatigue failures (surface pitting and tooth breakage) should be taken into account when dimensioning gear drives, only the tooth breakage is addressed here. The classical standardised procedure ISO 6336 [6.11] is usually used to determine the bending load capacity of a treated gear pair.

However, ISO 6336 does not apply to gears finished by sintering. Some guidelines on how to calculate the bending load capacity of sintered external spur gears are described in the information sheet AGMA 930-A05 [6.12]. However, the needed fatigue strength properties are not included in [6.12] and should be taken from the available literature or determined by own experiments. There is also a complicated geometrical analysis to determine the geometry factor for bending strength, which is usually very impractical when calculating sintered gear pairs.

In the presented study, the stress-life approach (see Section 2.1) is used to determine the fatigue life of sintered gears in regard to the bending stress in a gear tooth root. Because the stress field in the critical cross-section in a gear tooth root is determined numerically using the FEM-method, the proposed computational model can be applied to a wide range of gear pairs, and is not limited by some geometrical parameters as is the case for the ISO and AGMA Standards. The computational results are then compared with the experimental data, obtained on the back-to-back gear-testing rig.

6.2 Material and geometry of analysed sintered gears

The powder mixture used for the sintered gears analysed in this study was Höganäs Distaloy AB (SINT – D30 according to the German Standard DIN 30910-4) already described in Section 4.1. It contains 1.47 % Cu, 1.69 % Ni, 0.50 % Mo, 0.29 % C and 0.58 % of lube with an Fe balance. The apparent density of this powder is 3.15 g/cm^3 and Hall flow rate is 29 s/50 g [6.13, 6.14]. This powder was compacted into gear specimens and sintered at 1120 °C for 30 minutes in a controlled 10/90 hydrogen and nitrogen atmosphere. After sintering, sintered gears were machined to reduce tooth width and to produce a key slot in the hole (see Figure 6.1). The sintered PM gears were then austenitised at 915 °C, oil quenched and tempered for one hour at 175 °C. The final density of the specimen gears was 7.03 g/cm^3. The mechanical properties of the analysed gears were considered the same as were determined in the previous mechanical testing on the flat specimens.

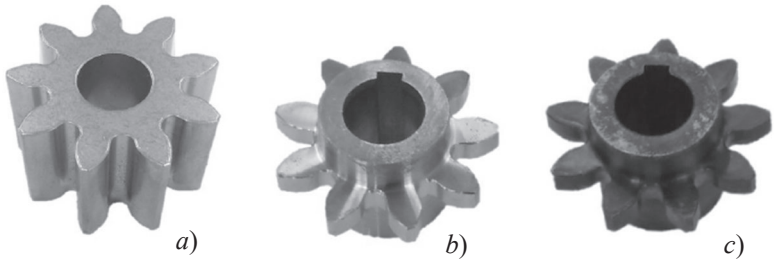

Figure 6.1: Analysed sintered gears
a) After compaction and sintering, *b*) After machining, *b*) After heat treatment

The tested sintered pinion with 9 teeth and 5 mm tooth width (see Figure 6.1) was paired with a wrought carburised tempered steel gear with 31 teeth and 20 mm tooth width at a centre distance of 80 mm. The normal module was 4 mm, the pressure angle at normal section was 25° and the helix angle was zero. The nominal rotational speed of the tested pinion was 800 rpm.

6.3 Computational analyses

In this study, the stress-life approach was used to determine the fatigue life N (i.e. number of loading cycles) of the analysed sintered gears in regard to the bending stress amplitude σ_a in a gear tooth root using the following equation:

$$\sigma_a = \sigma_f'(2 \cdot N)^b \tag{6.1}$$

where σ_f' is the fatigue strength coefficient and b is the fatigue strength exponent. The material parameters σ_f' and b can be determined experimentally, usually by means of rotating bending tests under fully reversed uniaxial loading (stress ratio $R = -1$). If this is not the case, the influence of mean stress and multi-axial state of stress should be considered when determining the appropriate stress amplitude σ_a in eq. (6.1). Here, the material parameters σ_f' = 875 MPa and b = – 0.153 were determined previously on the uniaxial pulsating test machine under stress ratio $R = 0$. The flat sintered specimens used in these experiments were made of the same powder mixture and produced with the same P/M technology (see Section 4.2) as already used for the analysed sintered gears. Because the stress ratio $R = 0$ corresponds to the operation of real gear pairs, the mean stress effect can be omitted in this case. On the other hand, the effect of

multiaxial stress in a gear tooth root should be considered (the Mises hypothesis was used for that purpose). Once the equivalent stress amplitude σ_{aE} is determined on the basis of alternating principal stresses in a gear tooth root σ_{a1}, σ_{a2} and σ_{a3}, it should be considered when determining the fatigue life according to eq. (6.1). Due to the pulsating loading regime (load ratio $R = 0$) in the tooth root, the equivalent stress amplitude σ_{aE} is equal to the half of the maximum equivalent stress $\sigma_{\max E}$ which can be obtained directly from the FEM-analysis.

When determining the fatigue life of machine parts using eq. (6.1), the influence of notch effect and surface finish should also be considered, because the material parameters σ_f' and b are usually determined using unnotched specimens with a polished surface. If this is not the case, the appropriate notch factor K_f and surface factor K_s should be taken into account [6.15]. In the presented work, the flat test specimens described above (see also Section 4.2) were produced in the same way as real sintered gears (compaction, sintering, additional thermal treatment, without additional polishing). For that reason, the surface factor K_s=1 can be assumed in such case. The notch factor K_f is included indirectly in the alternating principal stresses σ_{a1}, σ_{a2} and σ_{a3} which were determined numerically in this study using the FEM-method.

Figure 6.2*a* shows a 3D numerical model of the analysed gear pair. As shown, only one-third of the discussed gear was modelled (Instance 1), and one tooth of a pairing gear (Instance 2) was added to the assembly in such a way, that the contact between the two of them was at the outermost single contact point. The surfaces of shaft holes with diameter d_i = 15 mm and cut result surfaces were coupled to the reference points in such a way that all relative displacements and rotation between them were restricted. All degrees of freedom of both reference points were set to zero at the initial step. In the load step, rotation around the gear axis was applied to the reference point coupled to instance 1 (RP-1). Because of the contact between the teeth, the reaction moment was calculated in the reference point, which is considered as torque load to the gear that causes a stress field in the tooth root. This approach was taken because of much greater simulation stability if compared to the torque boundary condition.

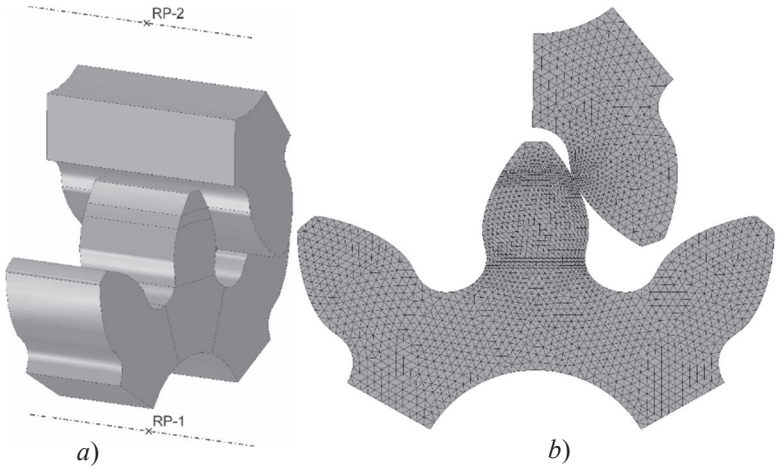

Figure 6.2: 3D model (*a*) and FE-mesh (*b*) of analysed gear pair

The material of both sections was modelled as linearly elastic with Young`s modulus $E = 1.42 \cdot 10^5$ MPa, which was taken from the data obtained by experimental testing of this material, discussed in Section 4.1. Contact between the two sections was modelled as tangentially frictionless, and as "Hard" contact in the normal direction. The whole assembly was meshed with linear tetrahedral elements of type C3D4H. There were approximately 427,000 elements in instance 1 and around 64,000 elements in instance 2 (Figure 6.2*b*). Numeric simulation was done in 20 increments. The first increments were used to establish the contact between two instances, and the rest to get the principal stress components in the tooth root of instance 1 for different reaction moments. Although stress gradients were covered to consider the stress intensity factor dependent on the notch geometry, the material notch sensitivity factor was neglected in this approach.

In the case of the high cycle fatigue regime usually applied during meshing of a gear pair, stress levels were much lower than the yield stress of the material, and, thus, the linear material model was sufficiently suitable for such calculation. This assumption made it possible to find a direct linear correlation between the torque T and the equivalent stress amplitude σ_{aE}. Furthermore, the scatter of dynamic tests should be considered when estimating the number of loading cycles until failure. Usually at least 10 fatigue tests are conducted at the same stress level to determine the scatter and to evaluate the fatigue life with a certain probability [6.17]. In such

approach, material parameters σ_f' and b can vary in dependence to the stress level. Due to the low number of data-points in our previous material testing [6.13], fatigue strength exponent b was assumed to be constant at all stress levels. However, to estimate the area in an S-N diagram with 95% probability of failure, the fatigue strength coefficient $\sigma_{f`i}$ was calculated for each torque T_i with corresponding data point (N_i, σ_{aEi}). A detailed description of such procedure may be found in Reference [6.14].

6.4 Experimental testing

Experimental evaluation of the fatigue life of the analysed sintered gears was done on the custom made back-to-back gear testing rig shown in Figure 6.3, with a mechanical torque loop between the test gear pair in housing (1) and the support gear pair in housing (2). Back-to-back configuration enables large testing moments in comparison to the power of a driving motor (3), which only provides rotational movement, and covers the losses caused by friction between the gears, in bearings and between gaskets and shafts. The basic parameters of the testing rig are written in Table 6.1.

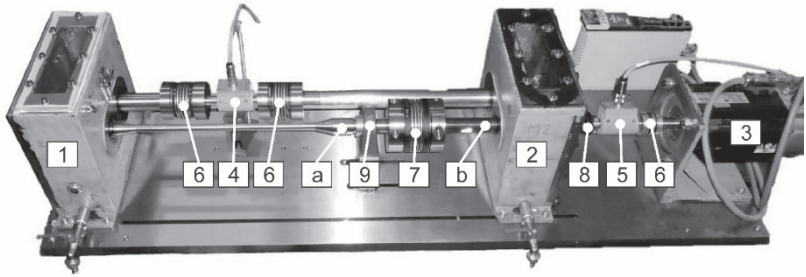

Figure 6.3: Custom made gear-testing rig [6.18]

Table 6.1: Basic parameters of the testing rig

Parameter	Test pinion	Support gear
Centre distance a	80 mm	
Normal module m	4 mm	
Pressure angle at normal section α_n	25°	
Helix angle β	0°	
Width b	5 mm	20 mm
Number of teeth z	9	31
Material	Sintered steel	42Cr5Mo4
Nominal rotational speed n	800 min^{-1}	232 min^{-1}
Lubrication	Immersed in gearbox oil: ISO VG 220	

Setting the loading torque begins with constraining the shaft rotation near the coupling (7) at position (b). Torque is then applied at position (a), next to support bearing (9). With loading torque applied, coupling (7) is engaged and the mechanical loop is established. The loading torque of the closed loop is monitored with a 200 Nm torque transducer (4), coupled between the shafts with two bellow couplings (6). A smaller 20 Nm torque transducer (5) was used to monitor the exact input torque at the motor (3), which was connected with a bellow coupling (6) to the motor (3) and with a safety bellow coupling (8) to the testing rig. A Data Acquisition System (DAQ) connects the two torque transducers (4 and 5) to the computer, where the measured data are recorded at 50 Hz. Data acquisition starts automatically, when the load at smaller 20 Nm torque transducer (5) is more than 2 Nm and also stops automatically when the torque is lower than 0.5 Nm. If gear breakage occurs, the test gears in housing (1) jam and the safety coupling (8) disengages.

In the experimental testing, such torque T was applied, that the expected number of loading cycles until failure was between 10^4 and 10^6 which corresponds to the high cycle fatigue regime. However, the exact setting of desired torque during the complete test was not possible due to the way of torque application, which does not permit configuration of loading torque during operation of the testing rig. In cases without tooth flank wear, this would not have posed a problem, but with wear of tooth flanks, the loading torque drops. The majority of the tests were done at 800 min^{-1}, while two tests were also done for higher rotational speed at 1200 min^{-1} for the quick speed dependence evaluation discussed in following Section, and are marked clearly in the Table 6.2.

6.5 Results and discussion

The results of sintered gear testing are shown in Table 6.2, where rotational speed, average torque, and the number of cycles are given for each tested sintered gear, marked from K01 up to K20. Average torque was calculated from all data points from the beginning of a particular test until tooth breakage. In the last column, some remarks are given where necessary.

Table 6.2: The results of the experimental testing

Specimen	Rotational speed n [min^{-1}]	Average torque T [Nm]	Number of cycles N	Remarks
K01	800	34.3	19 957	
K02	800	28.0	66 543	Inappropriate
K03	800	28.9	48 978	heat treatment
K04	800	27.0	49 518	
K05	800	22.4	1 034 480	runout
K06	800	34.3	114 040	
K07	800	39.5	45 508	
K08	800	31.5	229 552	
K09	800	28.4	320 640	
K10	800	26.2	455 832	
K11	1200	25.0	1 006 056	runout
K12	800	29.1	235 488	
K13	1200	29.6	971 112	runout
K14	800	38.3	43 284	
K15	800	31.6	119 816	
K16	800	31.3	148 568	shaft failure
K17	800	25.8	250 944	
K18	800	25.2	230 464	
K19	800	22.2	1 007 040	runout
K20	800	22.6	10 003 200	runout

The first four test gears achieved significantly lower operation time as expected, and were therefore subjected to the metallographic investigation, where inappropriate heat treatment was discovered, which was caused by an electrical issue in one of the heaters in the furnace for additional heat treatment. Subsequent test gears were then heat-treated and tested properly, as seen in Table 6.2.

All the results except K20 are plotted in Figure 6.4. Regular tests are marked with black dots and are well within the 95% probability of estimation, which is the grey area in the diagram. The first four tests with inappropriate heat treatment are marked with black circles and are on the edge of the estimation area. A black cross indicates an irregular test, where shaft failure occurred, but the gear remained intact. All four marks near 10^6 indicate runouts, but the two triangles are the tests run at 1200 min^{-1} and one of them is well outside the estimation area. This suggests a speed dependence of fatigue tests. The calculated estimation is based on fatigue tests that were done at 10 Hz, which would result in a rotational speed of 600 min^{-1}. The majority of tests, however, were done at 800 min^{-1}, which is 33% more than the fatigue tests. On the other hand, the tests at 1200 min^{-1} have a thee double

gear meshing frequency of the fatigue tests, which reduced the time of contact and, therefore, increased the number of stress cycles until failure.

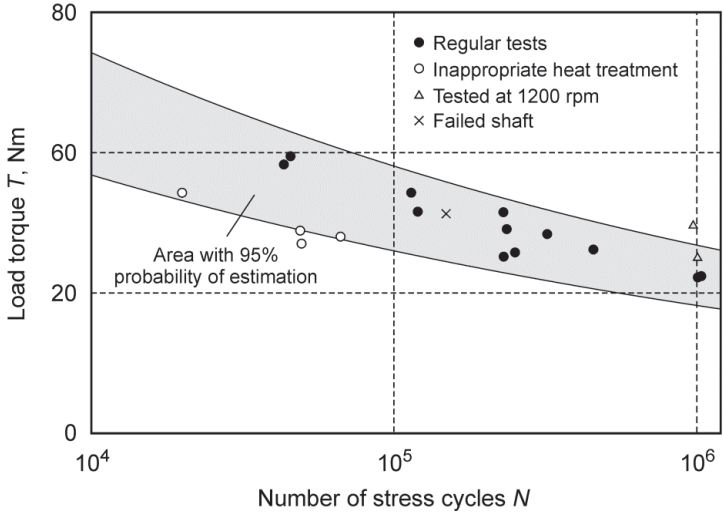

Figure 6.4: Computational and experimental results of tested sintered gears [6.18]

Examination of the failed test gears showed that all of them had similar damage. Typical damage of a tested gear is shown in Figure 6.5, where a photograph of test gear K08 is shown. Apart from the obvious tooth breakage, severe pitting of the working tooth flank can be seen. Although sintered gears were additionally hardened, the porosity of the material kept hardness relatively low if compared to wrought steel gears. (the hardness of tested gears was measured to be from 310 HV to 340 HV). Significant wear is also visible at the tooth tip, which is a result of high sliding velocities and possibly also a consequence of a low Young's modulus, which could cause meshing interference. Another area of extreme wear is seen at the tooth root on a neighbouring tooth. As it is only seen at the neighbouring tooth, this wear can be contributed to unusual meshing conditions right after tooth breakage and before jamming of the gears.

Figure 6.5: Typical fatigue fracture of a gear tooth (test gear K08)

6.6 Conclusions

The main goal of the presented study was to compare the computational and experimental approaches for determination of the fatigue life of sintered gears made of the powder mixture Höganäs Distaloy AB. The additional heat treatment (quenching, tempering) was also performed on the sintered gears. The computational model used in this study wss based on the stress-life approach, where the needed material data were taken from our previous research work. The experimental testing was done on a custom made back to back gear testing rig. Based on the obtained computational and experimental results the following conclusions can be made:

- The existing standardised procedure for determination of the load capacity of sintered gears (i.e. the AGMA Standard), requires calculation of many influential factors that are mainly dependent on the geometry of a gear. Here, the appropriate computational analysis may be used to replace this procedure and determine the stress field in a gear tooth root numerically. Usually, dies for sinter-press technology are made by wire-EDM and at least a 2D contour exists, which can be used for swift preparation of an FEM model.
- Although some fatigue data for sintered steels can be found in the literature, experimental testing of an exact material is preferred, because mechanical properties can be affected significantly by many variables: Density, sintering temperature and time, type and quantity of lubricant, ratio of alloying elements and additional heat treatment.

- To validate the proposed computational approach, the expected service life was calculated with 95% probability of failure. It was shown that, in the case of proper heat treatment, tooth breakage occurred well within the calculated estimation. Therefore, it can be assumed, that this approach is an appropriate calculation method for estimation of the fatigue life of sintered gears regarding the tooth root strength.
- However, during evaluation, some damage was also observed other than gear tooth breakage. Presumably, due to the relatively low hardness of tooth flanks, severe pitting occurred on the working flanks of the sintered gears. In that respect, the future work should be focused on the wear estimation of sintered PM gears.

References

[6.1] Flodin A., Brecher C., Gorgels C., Rothlingshofer T., Henser J., Designing powder metal gears, *Gear Solutions*, August 2011, 26–35.

[6.2] Dizdar S., High-performance sintered-steel gears for transmissions and machinery: A critical review, *Gear Technology*, August 2012, 60–65.

[6.3] Dorofeev Y.G., Baidala É.S., Static strength of the teeth of powder metallurgy planetary pinions for the Zhiguli automobile differential, *Soviet Powder Metallurgy and Metal Ceramics*, 24. 644–647.

[6.4] Lawcock R., Rolling-contact fatigue of surface-densified gears. *International Journal of Powder Metallurgy*, 42, 2006, 17–29.

[6.5] Koide T., Ishizuka I., Takemasu T., Miyachika K., Oda S., Load bearing capacity of surface-rolled sintered metal gears, *Int. J. of Automation Technology*, 2, 2008, 334–340.

[6.6] Bengtsson S., Fordén L., Dizdar S., Johansson P., Surface densified P/M transmission gear, *Advances in High Performance Powder Metallurgy Applications'*, Ypsilanti, Michigan, 2001.

[6.7] Sudhakar K.V., Fatigue behaviour of a high density powder metallurgy steel, *International Journal of Fatigue*, 22, 2000, 729–734.

[6.8] Sonsino C.M., Mueller F., Mueller R., The improvement of fatigue behaviour of sintered steels by surface rolling, *International Journal of Fatigue*, 14, 1992, 3–13.

[6.9] Dlapka M., Danninger H., Gierl C., Klammer E., Weiss B., Khatibi G., Fatigue Behaviour and Wear Resistance of Sinter-Hardening Steels, *International Journal of Powder Metallurgy*, 48, 2012, 49–60.

[6.10] Straffelini G., Benedetti M., Fontanari V., Damage evolution in sinter-hardening powder-metallurgy steels during tensile and fatigue loading, *Materials & Design*, 61, 2014, 101–108.
[6.11] ISO 6336, *Calculation of Load Capacity of Spur and Helical Gears*, Geneva, International Organization for Standardization, 2019.
[6.12] AGMA 930-A05. *Calculated Bending Load Capacity of Powder Metallurgy (P/M) External Spur Gears*, Information sheet, 2017.
[6.13] Glodež S., Šori M. Verlak T., A Computational Model for Bending Fatigue Analyses of Sintered Gears, *Journal of Mechanical Engineering*, 60, 2014, 649–655.
[6.14] Glodež S., Šori M., Vučković K., Risović S., Determination of Service Life of Sintered Powder Metallurgy Gears in Regard to Tooth Bending Fatigue, *Croat. J. for. Eng.*, 39, 2018, 129–137.
[6.15] Dowling, N.E., *Mechanical behaviour of materials,* Pearson Prentice Hall, New York, 2007.
[6.17] Glodež S., Šori M., Kramberger J., Prediction of micro-crack initiation in high strength steels using Weibull distribution, *Engineering Fracture Mechanics*, 108, 2013, 263–274.
[6.18] Šori M., Computational model for bending strength determination of sintered gears, *Ph.D. Thesis*, University of Maribor, Faculty of mechanical engineering, Maribor, 2015.